THESIS FOR THE DEGREE OF DOCTOR OF PHILOSOPHY

Tinkering with Light at the Nanoscale using Plasmonic Metasurfaces and Antennas: From Fano to Function

Mikael Svedendahl

Department of Applied Physics
CHALMERS UNIVERSITY OF TECHNOLOGY
Göteborg, Sweden 2014

Tinkering with Light at the Nanoscale using Plasmonic Metasurfaces and Antennas:
From Fano to Function
Mikael Svedendahl
ISBN 978-81-7597-019-6

Doktorsavhandlingar vid Chalmers tekniska högskola
Ny serie 3700
ISSN 0346-718X

Department of Applied Physics
Chalmers University of Technology
SE–412 96 Göteborg
Sweden
Telephone +46 (0)31 772 1000

Cover picture
Tinkering with light on the nanoscale using plasmonic nanoparticles. The left most graph shows the temperature increase due to illumination of gold nanodisk arrays at different incidence angles. The middle cartoon, illustrates the different spectra that can be detected in reflection for similar nanoparticle arrays. The right most figure shows the difference between two parameters of the reflected spectrum: The phase of the reflected light varies almost one order of magnitude faster than the reflected intensity.

Tryckservice i Ängelholm AB
Ängelholm, Sweden 2014

Tinkering with Light at the Nanoscale using Plasmonic Metasurfaces and Antennas: From Fano to Function

Mikael Svedendahl
Department of Applied Physics
Chalmers University of Technology

Abstract

Surface plasmons are charge density oscillations that can couple strongly to light and be excited in, for instance, thin metal films and metal nanoparticles. The plasmonic excitation squeezes the light down to nanometric length scales, far smaller than the wavelength of the light. This localization of light can be utilized in several surface-enhanced spectroscopies, for photothermal therapy, in optical trapping methodologies and in refractometric sensing schemes. This thesis focuses on various excitation schemes and spectroscopic measurements of surface plasmons and their sensitivity to the dielectric surrounding the metal.

Plasmonic excitations in metal films and nanoparticles have several common features, although only the former has successfully been commercialized as a refractometric biosensing platform. In a direct comparison of the two, both platforms performed equally well, from a sensitivity point-of-view. However, there are two significant advantages of nanoparticle plasmonic sensing schemes: The much relaxed excitation conditions and the miniscule size of the nanoparticle sensors. In a combination of these features, hundreds of individual nanoparticles were simultaneously interrogated in order to approach the few to single molecule detection limit. The data were obtained using a hyperspectral imaging methodology in combination with an enzymatic precipitation reaction that enhanced the plasmonic response from individual adsorbed molecules. The results demonstrated a sensitivity in the single molecule range, but a number of inhomogeneous broadening effects prevented counting the exact number of molecules per particle.

In a different line of research, plasmonic nanoparticles placed in a large two dimensional array with small interparticle spacing and supported with a glass substrate were interrogated. The nanoplasmonic layer then act as a metamaterial that can support strongly asymmetric resonances, dispersive modes and even complete light absorption. These effects are due to a so-called Fano interference between the plasmon excitation and the reflection from the dielectric boundary. Complete absorption enhances the optical near-fields, which can be utilized in, for instance, surface enhanced spectroscopy techniques. However, minimizing the reflection has another interesting feature: A rapid phase jump of the reflected light. The phase is shown to vary about one order of magnitude faster than the reflected intensity and, therefore, also provides around one order of magnitude higher sensitivity to molecular adsorption.

Altogether, the results presented in this thesis provides a basis for several interesting sensing schemes, as well as insight into some fundamentally intriguing phenomena regarding absorption, nanoscale coherence and light localization.

Keywords: surface plasmons, biosensing, metamaterials, Fano resonances

APPENDED PAPERS

The following papers are included in this thesis:

I. **Refractometric Sensing Using Propagating versus Localized Surface Plasmons: A Direct Comparison**

Mikael Svedendahl, Si Chen, Alexandre Dmitriev, and Mikael Käll.

Nano Letters 9, 4428 (2009)

II. **Ultrahigh Sensitivity Made Simple: Nanoplasmonic label-free biosensing with an extremely low limit-of-detection for bacterial and cancer diagnostics**

Si Chen, Mikael Svedendahl, Mikael Käll, Linda Gunnarsson and Alexandre Dmitriev.

Nanotechnology 20, 434015 (2009)

III. **Plasmon-Enhanced Colorimetric ELISA with Single Molecule Sensitivity**

Si Chen, Mikael Svedendahl, Richard P. Van Duyne, and Mikael Käll.

Nano Letters 11, 1826 (2011)

IV. **Fano Interference between Localized Plasmons and Interface Reflections**

Mikael Svedendahl and Mikael Käll.

ACS Nano 6, 7533 (2012)

V. **Plasmon-Enhanced Enzyme-Linked Immunosorbent Assay on Large Arrays of Individual Particles Made by Electron Beam Lithography**

Si Chen, Mikael Svedendahl , Tomasz J. Antosiewicz , and Mikael Käll.

ACS Nano 7, 8824 (2013)

VI. **Complete Light Annihilation in an Ultrathin Layer of Gold Nanoparticles**

Mikael Svedendahl , Peter Johansson and Mikael Käll.

Nano Letters 13, 3053 (2013)

VII. **Phase-based Optical Biosensing in a Nanoplasmonic Metamaterial Layer**

Mikael Svedendahl , Ruggero Verre and Mikael Käll.

In Manuscript

My contribution to the appended papers:

I. I designed and conducted the experiments, analyzed the data and wrote a draft of the paper.
II. I built the optical setup used in the biosensing experiments and participated in some of the optical measurements.
III. I performed numerical simulations and participated in the data analysis and drafting parts of the paper.
IV. I designed and performed the optical experiments, developed the analytical models and drafted the paper.
V. I performed numerical calculations, participated in the data analysis and resulting discussions.
VI. I designed and performed the optical experiments, developed the analytical and numerical models and drafted the paper.
VII. I designed and performed the optical experiments and drafted the manuscript.

The following works are related, but not included in this thesis:

Papers

VIII. **A Thermal Plasmonic Sensor Platform: Resistive Heating of Nanohole Arrays**

Mudassar Virk, Kunli Xiong, Mikael Svedendahl, Mikael Käll and Andreas B. Dahlin

Nano Letters, in press

Book Chapters

IX. **An Introduction to Plasmonic Refractive Index Sensing**

Mikael Svedendahl, Si Chen, and Mikael Käll.

In Alexandre Dmitriev (Ed.) *Nanoplasmonic Sensors* 2012. New York: Springer

X. **Nanostructured Surface Plasmon Resonance Sensors**

Mikael Svedendahl, Si Chen, and Mikael Käll.

In Andrea Cusano (Ed.) *Optochemical nanosensors* 2013. Taylor and Francis

XI. **Nanostructured Antennas for Refractive Index Sensing**

Timur Shegai, Mikael Svedendahl, Si Chen, Andreas Dahlin and Mikael Käll.

In Mario Agio (Ed.) *Optical Antennas* 2013. Cambridge University Press

Patent Applications

XII. **Method of exciting a layer of metallic nanostructures on solid support to achieve total absorption and its use in surface enhanced spectroscopy, refractometric sensing and optical trapping**

Mikael Svedendahl and Mikael Käll. Patent no.: US 61/576,361

Contents

Chapter 1

Light at the Nanoscale

Seeing is believing. Sight is perhaps the most important of our human senses, allowing us to study and interpret the world we live in, ranging from the enormous span of the universe to the microscopic life within single cells. Therefore, both the telescope and the microscope were revolutionary inventions, with which human kind could finally envision the vastness of the universe and study fatal bacteria by eye. Leaving Gallileo and the Milky Way to the side, this work *focuses* on light in the micro- and nanoscopic universe, which we otherwise cannot resolve.

The first microscopes where probably developed in the Netherlands during the late 16^{th} or in the beginning of the 17^{th} century. In the latter part of the 17^{th} century, Robert Hooke published his astounding work *Micrographia*, in which he, for example, published drawings of his observations through the eyepiece of his microscope[1]. As seen in Figure 1.1 the microscopes back then did not show much resemblance with today's automated systems, but they contained more or less the main optical components. With this powerful tool Hooke could investigate the microscopic universe and found the *cell*, named after what he thought looked like monks quarters.

The development of the microscope continued over the next century, however, it was soon clear that also the microscopes were limited in resolving power. The concept of the so-called *diffraction limit* was published in the 1870's by Ernst Abbe and Hermann Helmholtz, stating the smallest resolvable distance, d, between two point sources depended on the wavelength, λ, and light acceptance cone of the optics, that is, the numerical aperture, NA, of the system [2, 3]:

$$d \approx \frac{\lambda}{2NA}. \tag{1.1}$$

Diffraction of light blurs the image of a point source leading to a so-called Airy pattern in the far field [4]. The criterion for resolving two point sources close to each other was defined by Lord Rayleigh as when the maximum of one source coincided with the first minimum from the second source [5]. Even though a perfect lens would be feasible to fabricate, the diffraction would limit the resolvable features. For visible light, ranging from about 400 to 750 nm, the smallest resolvable details are about 200 nm. It is of course possible to use light of shorter wavelengths, such as ultra-violet or even X-ray light, but this may be harmful for the specimen under study, for instance living cells.

Today, however, there are several ways in order to retrieve information from *beyond* the diffraction limit. Naturally, these length scales describes biology and

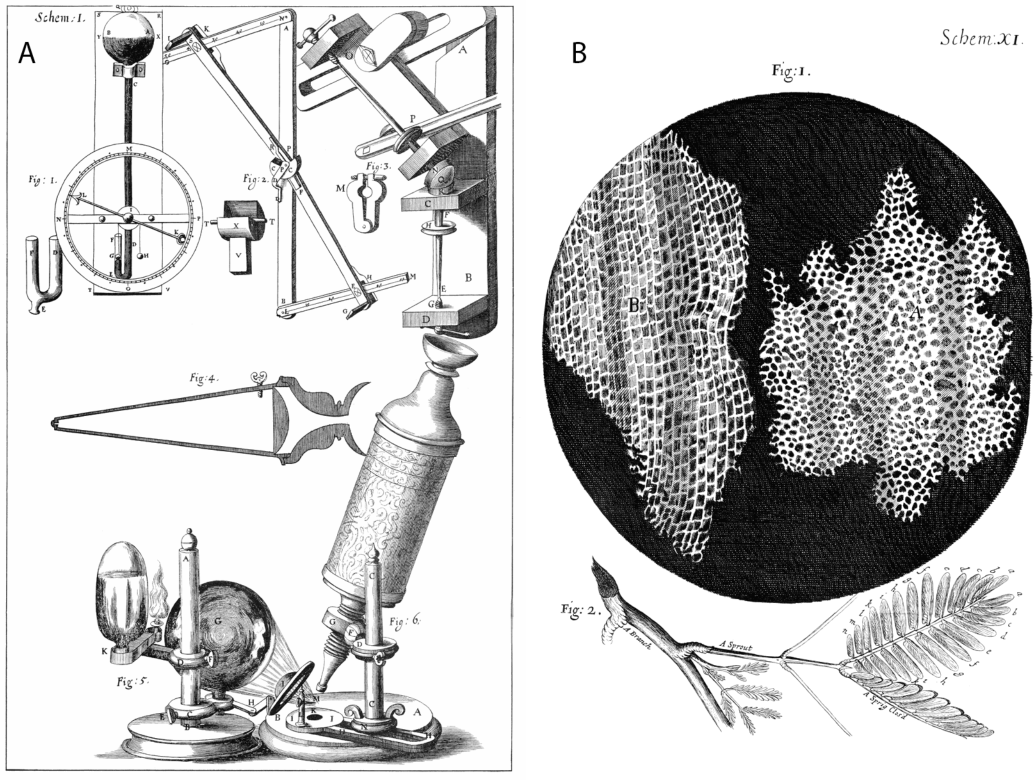

Figure 1.1: Robert Hooke's microscope (A) and cell observation (B).

chemistry in more detail, but are also extremely important in many more fields of research and technology. During the two last decades, there has been a boost in optical imaging techniques, based on far-field methodologies and/or mathematical post-processing techniques [6–15]. However, there has also been a tremendous development on techniques that rely on the properties of nanoscopic matter; Techniques that enables single molecule spectroscopy, molecular manipulation and detection, enhanced catalytic activity and so on [16–21]. This field of research is generally termed *nanotechnology* or *nanoscience*, due to the length scales of the structures which either are studied or utilized for investigating other processes on these length scales. According to the National Nanotechnology Initiative [22], there are several key properties of nanoscale matter that make it so interesting: The geometric overlap with many biological processes, the possibility to study *quantum effects*, to increase surface-to-volume ratios, for instance to enhance catalytic activity and, last but not least, the study of size-dependent properties of matter.

One of the main concepts of nanotechnology is perhaps *tunability*. For example, noble metals have completely different properties on the bulk scale and in the nano regime. Dividing bulk gold into two pieces does not change them very much: You have only created two bulk pieces with identical properties. However, taking a gold or silver nanoparticle and slicing it into two, yields two pieces that 1. is much different from the original piece and 2. most likely have different properties, compared one to another.

Nanotechnology does not, however, mean that researchers should only deal with very small length scales. It is also possible to utilize nano effects on the macroscopic scale to enhance, tune or create all-new properties of matter, that does not exist in Nature, as we know it. Again, catalysis is good example, but also exotic optical properties, such as negative refraction, optical cloaking, complete absorption of light etcetera, can be achieved on the macroscale, possibly to create perfect lenses for subdiffraction imaging or more efficient solar cells.

However, the great advances made within the nanotechnologic field is to a large portion due to several enabling technologies. The perhaps most prominent and obvious is nanofabrication techniques, through which increasingly complex and exact structures can be made, continuously pushing the resolution limits and cost of fabrication. Perhaps not as obvious is the impact of lasers, CCD imaging technology, the Scanning Electron Microscope (SEM), optical fibers and so on. All these technologies enabled nanoscopic sensors based on nanoscale structures such as nanocantilevers, carbon nanotubes, magnetic nanoparticles, quantum dots, whispering galleries, silicon nanowires and plasmonic nanostructures [23–33]. All the nanoscale sensors are, in principle, interesting because of the overlap between the size of the sensor and the analyte to be detected. Further, their small size also make dense packing of individual sensors possible.

Nanophotonics and nanoplasmonics are subfields of nanotechnologic research. Both fields concerns with light at the nanoscale, with the latter utilizing surface plasmons for field confinement. Nanophotonics may contain interesting aspects such as photonic crystals, subwavelength dielectric resonators, quantum dots and many more [23, 34–37]. The main topic of this thesis is surface plasmons. Chapter 2 will give a more detailed introduction to their properties, but there are some major characteristics to point out already now. Metal nanoparticles, which support surface plasmons in the visible range, act as optical antennas, focusing the light down to length scales smaller than their own geometric dimensions. On the other hand, their apparent optical cross section, that is, the geometrical area that the particles seems to interact with incoming light, is about one order of magnitude *larger* than their own geometrical area! This discrepancy make metal nanoparticles extremely interesting for transforming information about nanoscale interactions into detectable signals in the far field.

Chapter 3, comprises the *macroscale* optical properties that arises due to patterning surfaces with plasmonic nanoparticles. Although individual nanoparticles can be excited from almost any angle, the excitation efficiency is vastly altered in this case, depending on the incident polarization and energy of the light, as well as the surface density of nanoparticles. In fact, such arrays can be tuned into a so-called *perfect absorption* condition where all light is absorbed within the nanoparticles.

As described above, the surface plasmons can be used to probe processes on the nano-scale, such as molecular adsorption and desorption kinetics. Chapter 4 outlines the main concepts within this field of research, for instance, how the field confinement affects results and how the macroscale optical properties, described in Chapter 3, can be used in enhanced sensing techniques.

Finally, a summary and a short outlook into future works and open questions is found in Chapter 5. It also briefly summarizes the appended papers, published during this work.

Chapter 2

Plasmonics

Plasmonics is the collective name for applications and research involving plasmons, charge density oscillations typically excitable with visible light in noble metals under special circumstances. The history of plasmonics dates back to the beginning of the last century when Mie described the resonances of small particles, Drude explained the dielectric function of metals and Wood experimentally documented the first indication of surface plasmon resonances (SPRs), although not fully understood as a plasmonic response until several decades later, through the pioneering work of Ugo Fano [38–41]. Plasmons in metals are due to the collective oscillations of conduction electrons, which are free and delocalized. In the 1950's and 1960's a configuration for exciting plasmons in thin films was developed [42–44], leading to the application with perhaps the largest impact of the plasmonic community as of today: The refractometric label free thin film biosensor, first described by Nylander and Liedberg in the early 1980's [45, 46].

The strong interaction of plasmons with visible light is responsible for the beautiful stained windows in medieval churches. The colors of stained glass stem from small nanosized noble metal particles supporting so-called localized SPRs (LSPRs). LSPRs absorbs different colors depending on the geometrical shape, size, material and surrounding environment of the nanoparticles. The distinctive color comes from the great coupling efficiency between the nanostructures and the incident light, manifesting in optical cross sections much larger than the nanoparticles' geometrical extent.

Recent advances in nanofabrication techniques enables detailed design of both individual and arrays of nanostructures. The design of individual nanostructures has, for instance, lead to deep sub-wavelength directivity of light and plasmon assisted lasing in so-called SPASERs [47–49]. The nanoscale design of nanostructure arrays enables even more spectacular optical properties, such as metamaterials and meta-surfaces exhibiting negative refraction, anomalous reflection and refraction and plasmon-induced transparency [50–55].

Nanoparticles can be thought of as antennas, transmitting signals between our macroscopic world in the optical far field and the nano-sized reality of the plasmonic mode volumes, residing in the optical near-field. The near fields are enhanced, which enables several surface enhanced spectroscopies, enhanced photovoltaics and photothermal therapies [56–62]. Plasmonic refractometric sensing schemes appears due to the large sensitivity of the plasmon to the refractive index of its immediate surroundings. Due to the large confinement of light in the optical near field, the plasmon is only sensitive to changes up to 10-100 nm from the metal surface, which

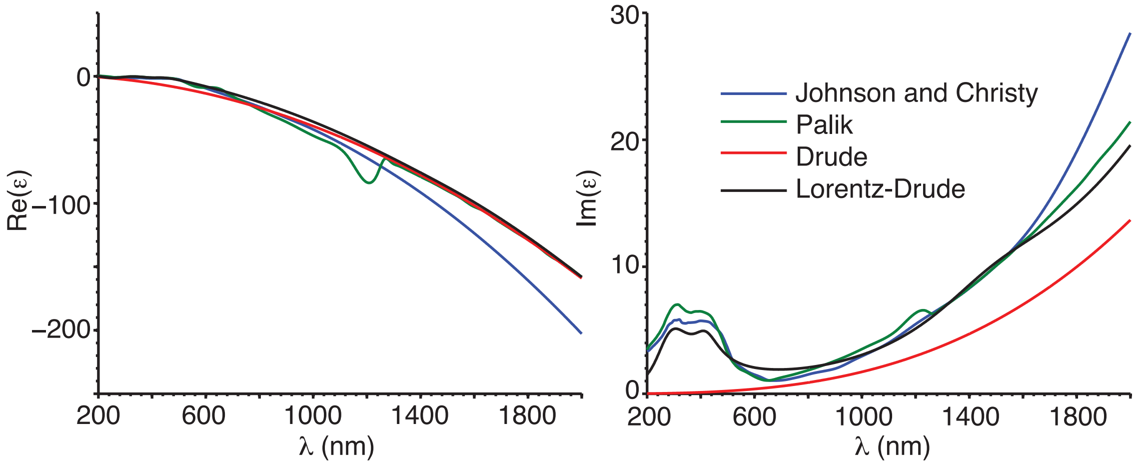

Figure 2.1: The permittivity of gold from experimental data and the Drude approximation [38, 63, 64]. (A) The real part of the permittivity is quite accurately described by the Drude model, however, it underestimates the imaginary part. (B) The model is improved by adding Lorentzians to describe, for instance, interband transitions in the material, as described by the Lorentz-Drude model [64, 65].

overlaps well with the sizes of many interesting molecules, such as proteins, sugars, nucleic acids, lipids etc. The refractometric plasmon biosensors do not focus on the colorful appearance of plasmons, but rather the change of appearance due to changes in the dielectric properties in its vicinity.

2.1 The Drude Approximation

Metals are often referred to as perfect reflectors and are, for instance, used as waveguides in microwave technology. However, at shorter wavelengths, the reflectivity decreases. Metals do not allow external electrical fields to penetrate them in the microwave region, but this is not true for visible and/or near infrared light. Further, alkali metals are fully transparent in UV-light, while noble metals, like gold and silver, are not. In this region these metals experience inter band transitions leading to high absorption.

All the optical properties are described by the complex dielectric function, ε, of the material. For metals the dielectric function is complex, with a negative real part. Much of the basics of plasmonics can be explained by the dielectric function of metals. The permittivity of solids varies with the incoming frequency of light, ω. The dielectric function and the refractive index of solids are complex, since the electrons face resistance and experiences interband and intraband transitions. One simple method to model ε is the Drude model, named after Paul Drude, whom was a German scientist specialized in optics and proposed this model 1900 [38]. The model considers the valence electrons of the metal as a free electron gas, influenced by an external electric field. The electrons are elastically bound to an atom, here assumed to be much smaller than the wavelength of the applied field. The equation of motion can then be written as:

$$m\frac{\partial^2 x}{\partial t^2} + m\gamma\frac{\partial x}{\partial t} = -eE_0 e^{-i\omega t}, \tag{2.1}$$

The applied electric field will induce a polarization $P = Np$, where $p = -ex_0$, e is the electron charge, m is the electron mass and N is the number of electrons per unit volume. With the ansatz $x(\omega, t) = x_0(\omega)e^{-i\omega t}$, one finds:

$$P = -\frac{Ne^2 E_0}{m(\omega^2 + i\gamma\omega)} = \varepsilon_0(\varepsilon_m - 1)E_0, \tag{2.2}$$

from which ε can be retrieved:

$$\varepsilon_m(\omega) = 1 - \frac{Ne^2}{\varepsilon_0 m(\omega^2 + i\gamma\omega)} = 1 - \frac{\omega_p^2}{\omega^2 + i\gamma\omega}, \tag{2.3}$$

where $\omega_p = \sqrt{\frac{Ne^2}{\varepsilon_0 m}}$. There are several simplifications and assumptions made in the model. The main limitation is that it only considers the contributions from the free conduction electrons. Therefore, it is common to also add the interband transitions as Lorentzian functions to retrieve a more complete representation of ε_m, see Figure 2.1. The Drude model is, however, still useful as it gives an indication of how the dielectric function varies with the frequency of the light and, as plasmons are indeed oscillations of the free electrons in metals, it captures the interesting features relevant to this field of research.

2.2 Surface Plasmon Polaritons

The dielectric properties of noble metals, described in the previous section, results in several interesting optical features. For instance, the negative real part of the permittivity leads to surface bound waves at a metal/dielectric interface. The surface waves are generally termed surface plasmon polaritons (SPPs) due to the strong coupling between photons and the plasmons in the metal. The properties of the SPPs can be derived directly from electrodynamic boundary conditions for transverse-magnetic (TM) waves, which result in the famous dispersion relation:

$$k(\omega) = \frac{\omega}{c}\sqrt{\frac{\varepsilon_m(\omega)\varepsilon_d}{\varepsilon_m(\omega) + \varepsilon_d}}, \tag{2.4}$$

where ε_d denote the permittivity of the dielectric medium and c is the light velocity in vacuum. Any bound waves are not allowed for transverse electric (TE) waves, unless assuming magnetic media.

In order to excite any surface waves, both energy and momentum needs to be conserved. The dispersion describe that SPPs have a larger wavevector component, or momentum, than ordinary photons in the dielectric medium, as illustrated in Figure 2.2A. Although this discrepancy is what actually lead to the confinement of the light, it also mean that any excitation of the SPP is impossible with direct illumination from the dielectric side. In practice, surface roughness may lead to some excitation and de-excitation possibilities, but in the ideal case other methods have to be used. Generally, there are two main means of excitation: Using high index materials on the back side of a thin metal film or using a grating in the vicinity of the

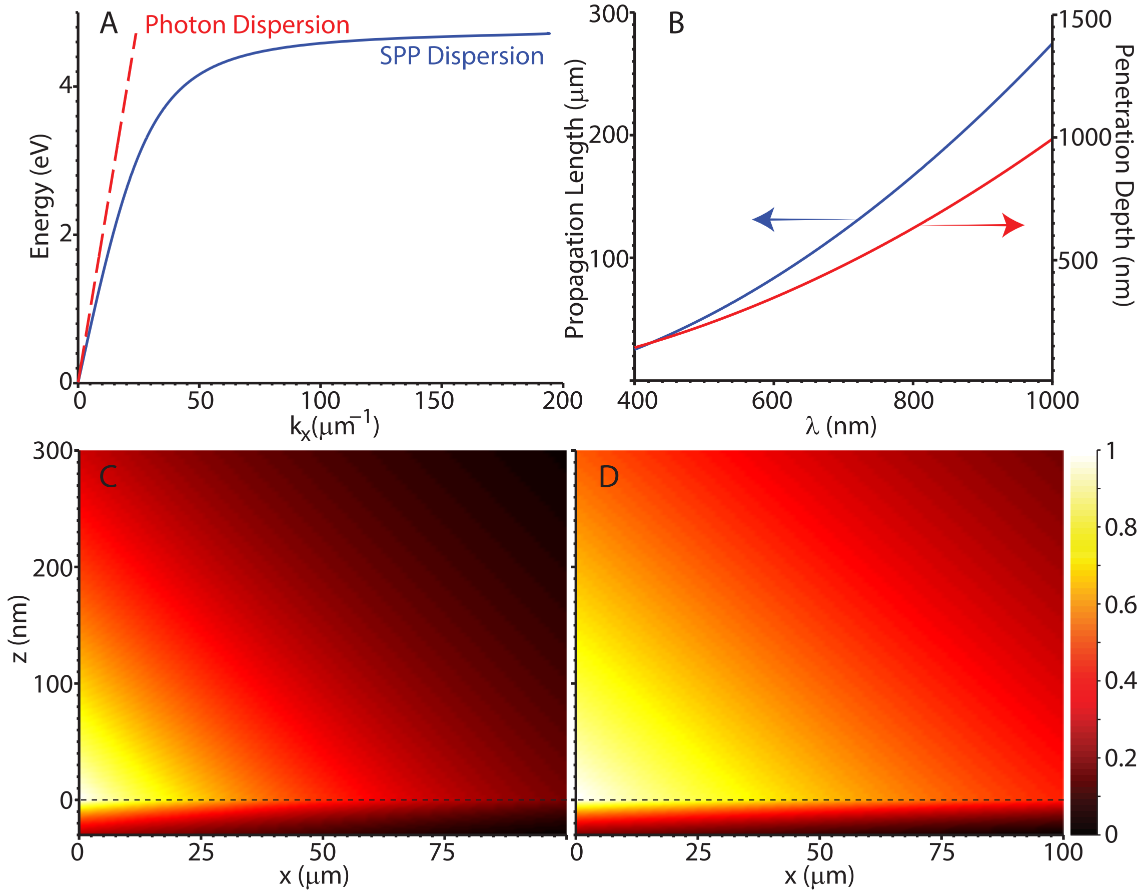

Figure 2.2: SPP properties. (A) An SPP is a surface wave with a larger k-vector than a photon in the same medium. (B) The confinement to the surface yields two distinctive lengths, the propagation length along the surface, in x, and the penetration depth, in the ambient, along z. These lengths defines the spatial extension of the SPP, which varies with wavelength. (C-D) The field amplitude, $|E(x, z)|$, versus x and z at $\lambda = 550$ nm (C) and 750 nm (D). All data is calculated using the Drude model for gold.

boundary. The former alternative uses photons that tunnel through a relatively thin metal film, in order to excite the SPP at the metal/low index dielectric side. Since a high refractive index material support photons that can carry more momentum, such a system can lead to high excitation efficencies. In the grating coupling case, the momentum of the photons is increased by the grating scattering properties, thus leading to matching of the energy and momentum criteria for excitation.

Figure 2.2B show the confinement of the SPP for two different wavelengths and ambient media, that is, with ambient permittivity $\varepsilon_d = 1$. A much larger portion of the fields penetrate into the dielectric media, compared to the fields penetrating within the metal (not shown), with longer wavelengths penetrating deeper than shorter wavelengths. The SPP is also confined in-plane, along the surface. Generally, this confinement is termed *propagation length*, which is defined from the imaginary part of equation (2.4). The penetrating depth and the propagation length thus define the “mode volume” that an SPP comprises. For example, when using the system as a refractive index sensor, the refractive index within the whole mode volume will contribute to the signal.

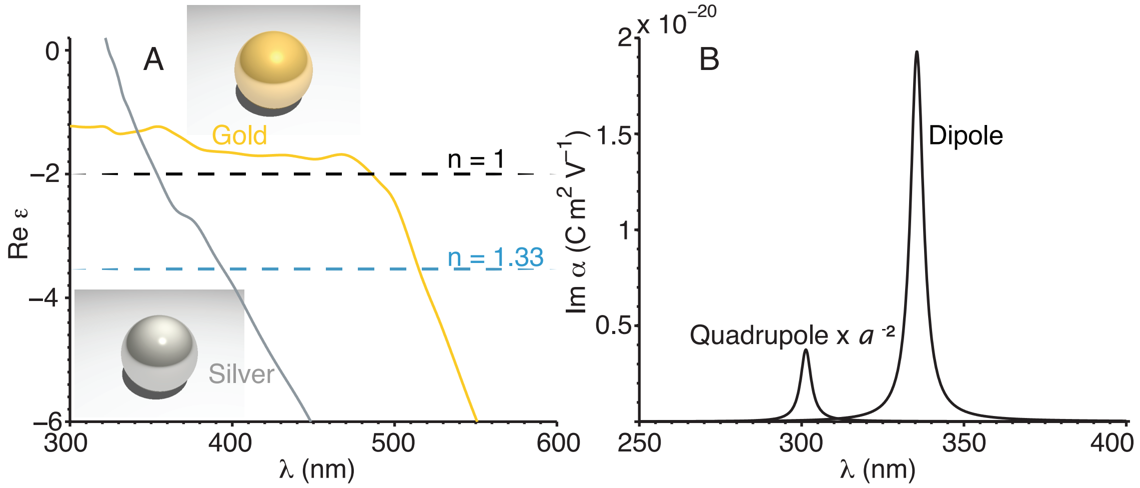

Figure 2.3: Dipolar and quadrupolar resonances in small metal spheres. (A) The dashed horizontal lines show the dipolar resonance conditions for small spheres in air and water medium, see Eq. (2.5), while the full lines represent the real dielectric functions of gold and silver. (B) Dipole and quadrupole polarizabilities in a small gold sphere, $a = 22$ nm. ε_m is approximated by the Drude model.

2.3 Nanoplasmonics

In the same manner that the dispersion relation of an SPP can be solved at a planar interface, it is possible to calculate the polarizability of a conductive sphere in a dielectric environment [66, 67]. External electric fields lead to the separation of surface charges on the sphere, again due to the free conduction electrons. The surface charges creates a polarization field inside the particle that seeks to restore field neutrality. This field will be dependent on the dielectric function of the particle, from which a frequency dependent polarizability can be derived. Generally, these calculations are valid in the so-called quasistatic regime, where the nanoparticle is assumed to be significantly smaller than the wavelength, but the dielectric function still has a frequency dependency. The calculations lead to a so-called Clausius Mossotti polarizability:

$$\alpha(\omega) = 4\pi\varepsilon_d a^3 \frac{\varepsilon_m(\omega) - \varepsilon_d}{\varepsilon_m(\omega) + 2\varepsilon_d} = 4\pi\varepsilon_d a^3 \left(\frac{\omega_0}{\omega_0^2 - \omega^2 - i\omega\gamma} - \frac{\omega^2 + i\omega\gamma}{\omega_0^2 - \omega^2 - i\omega\gamma} \frac{1 - \varepsilon_d}{1 + 2\varepsilon_d} \right). \tag{2.5}$$

Here, a is the radius of the sphere and the dielectric function of the metal has been approximated by the free electron Drude model [38]. There are corrections to the model, taking into account retardation effects, but the main characteristics is found in equation (2.5), including enhanced near fields surrounding the nanoparticle and a clear resonance condition when the denominator vanishes, dependent on the surrounding permittivity. For small γ the resonance frequency is given by $\omega_0 = \omega_p/\sqrt{1 + 2\varepsilon_d}$, and the LSPR will red-shift if $n_d = \sqrt{\varepsilon_d}$ increases, according to $\Re[\varepsilon_m + 2\varepsilon_d] = 0$. Figure 2.3A shows the resonance condition for small spheres in air and water environment, together with the real parts of the dielectric functions of gold and silver. The real part of noble metal dielectric functions decrease for longer wavelengths, resulting in a red-shift of the resonance condition as the refractive

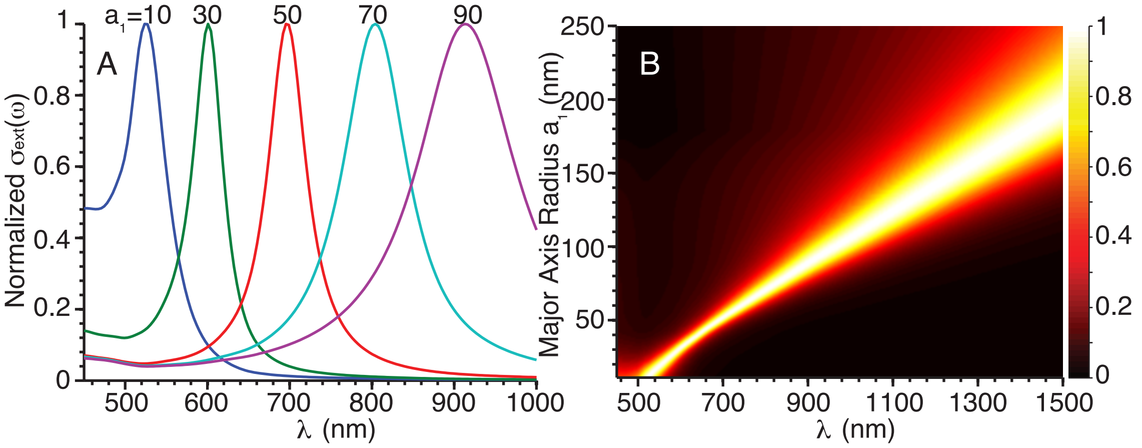

Figure 2.4: Normalized extinction cross sections of gold ellipsoids. (A) By varying the major axis, $a_1 = a_2$, while maintaining a constant minor axis, $a_3 = 10$ nm, the in-plane resonance red-shifts. (B) Color plot of normalized $\sigma_{ext}(\omega)$ when varying the same parameters, demonstrating the broadening of the resonances at longer wavelengths. Data calculated using equation (2.8) and (2.9) in water, $n = 1.33$, together with the modified long wavelength approximation and using experimental data for the dielectric function of gold [63, 69, 70].

index of the surrounding medium increases.

Equation (2.5) describe the dipolar resonance of the metal sphere. However, there are many more resonances potentially excitable. These multipoles can be found from [66, 68]:

$$\alpha_l(\omega) = \frac{l(\varepsilon_m(\omega) - \varepsilon_d)}{l\varepsilon_m(\omega) + (l+1)\varepsilon_d} a^{2l+1}, \tag{2.6}$$

which, for instance lead to the quadrupolar resonance [68]:

$$\alpha_2(\omega) = \frac{4}{3}\pi\varepsilon_d a^5 \frac{\varepsilon_{metal}(\omega) - \varepsilon_d}{2\varepsilon_{metal}(\omega) + 3\varepsilon_d}. \tag{2.7}$$

In Figure 2.3B, the imaginary part of equations (2.5) and (2.7) is plotted, using a Drude model for ε_m. For small spheres, the quadrupole is about a factor a^2 weaker than the dipolar resonance. The quadrupole is located at shorter wavelengths, often obscured by interband transitions in metals such as gold. Additional multipoles are even weaker, which make the dipolar approximation of many plasmonic nanoparticle resonances relevant.

Also the shape of the nanoparticle plays an important role for the resonance position. For example, if the sphere is elongated along one direction, the surface charges on the opposite sides of the spheroid will move further and further apart, decreasing the restoring force and thus shifting the resonance to lower energies, or longer wavelengths. A useful approximation for the polarizability of ellipsoids can be written as:

$$\begin{array}{lcl} \alpha(\omega) & = & \frac{4\pi a_1 a_2 a_3}{3} \frac{\varepsilon_m(\omega)-\varepsilon_d}{\varepsilon_d + L_i(\varepsilon_m(\omega)-\varepsilon_d)} \\ L_i & = & \frac{a_1 a_2 a_3}{2} \int\limits_0^\infty \frac{\delta q}{(a_i^2+q) f(q)} \\ f(q) & = & \sqrt{(q+a_1^2)(q+a_2^2)(q+a_3^2)} \\ \sum L_i & = & 1 \end{array}, \tag{2.8}$$

where a_1, a_2 and a_3 denote the different axis of the ellipsoid, which determine the depolarization factor, L_i $(i = 1, 2, 3)$. Commonly, nanodisks are approximated as oblate spheroids for analytical simplicity. For oblate spheroids $a_1 = a_2$ and $a_1 > a_3$, while prolate spheroids have $a_1 < a_3$.

Generally, the optical cross sections of nanoparticles or nanoparticle ensembles are measured. The three most important cross sections are the extinction, scattering and absorption cross sections, which are all dependent on the polarizability. The cross sections are given by:

$$\sigma_{ext}(\omega) = \frac{\omega}{c} \operatorname{Im}(\alpha(\omega)), \tag{2.9}$$

$$\sigma_{sca}(\omega) = \left(\frac{\omega}{c}\right)^4 |\alpha(\omega)|^2, \tag{2.10}$$

$$\sigma_{abs}(\omega) = \sigma_{ext}(\omega) - \sigma_{sca}(\omega), \tag{2.11}$$

Figure 2.4 shows how the resonance shift in extinction cross section spectra for varying gold ellipsoidal geometries. Here, the calculations include retardation effects, by using the modified long wavelength approximation (MLWA) [69, 70]. Larger aspect ratios, a_1/a_3, result in a red shift of the resonance position and additional broadening of the resonances. From a plasmonic point of view, the spectral region 600-750 nm yields more narrow resonances, which may be beneficial for several applications. Typically, surface enhanced phenomena is related to the so-called quality-factor, or Q-factor, of the resonance [71]. This parameter is calculated as the resonance energy over the width of the resonance. Good resonators have large Q-factors as the light is confined within them for a longer time.

From equation (2.8) it is clear that an anisotropic nanoparticle have different resonances depending on the excitation condition. To illustrate discrepancy, Figure 2.5 show transmission spectra for two anistropic gold nanoparticle ensembles: Elongated nanoparticles and taller nanocones. By illuminating the elongated nanoparticles at normal incidence, while aligning the incident polarization along the short and long axis of the nanoparticle, respectively, different resonances are probed. The dips in the transmission spectra is related to the two in-plane resonances. Similarly, tall nanostructures have prominent resonances out-of-plane, which lead to different spectra depending on the incident angle of the light, as illustrated in Figure 2.5 B.

Furthermore, nanoparticles can interact, both on the short range, though the optical near fields, and on the long range, through far-field interactions. Such properties can be understood through the Coupled Dipole Approximation (CDA) [72, 73]. Placing two dipoles in close vicinity of another alters their optical responses. In Figure 2.6A two dipoles, with resonances appriximated by gold ellipsoids, are placed with varying distance from one another, from 50 to 5 nm. Shorter distances decreases the restoring force and the resonance red shifts, if the dipoles are aligned

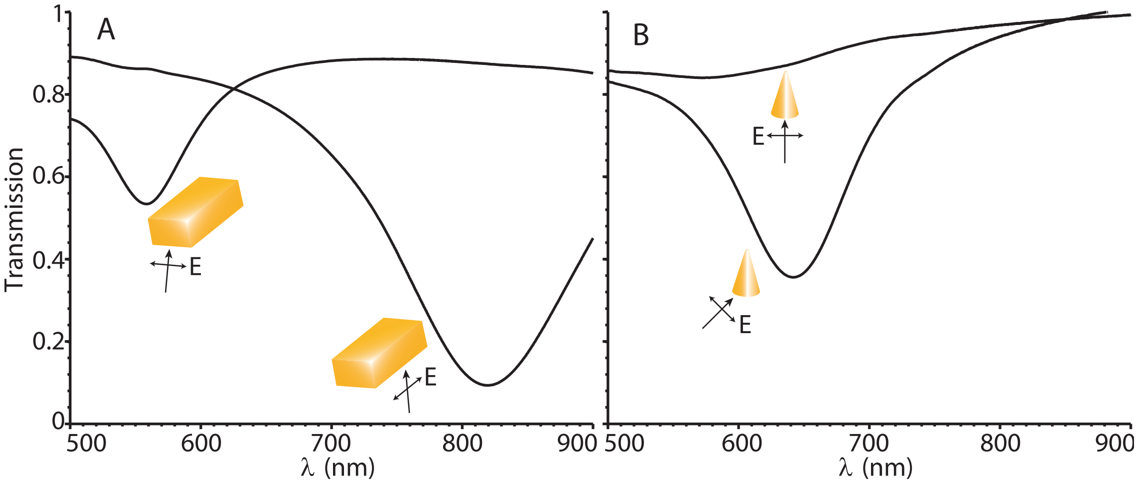

Figure 2.5: Different resonances in anisotropic nanoparticles. By altering the excitation conditions, different resonances are excited. (A) Elongated nanoparticles excited at normal incidence with the polarization of the incident light parallel to the short and long axis, respectively. (B) Tall nanoparticles, nanocones, excited at normal and 45° incidence.

with the incident polarization. Smaller changes are seen if the polarization is perpendicular to the dimer axis, but the resonances show a slight blue shift, due to an increased restoring force. If more nanoparticles are considered, far field interactions can become prominent [74–76], as exemplified in Figure 2.6B. Placing dipoles in a periodic array lead to diffractive coupling effects, which may lead to sharp features in the optical spectrum. For a less ordered array, these effects are much smaller, but the far-field interactions are still there, leading to small differences between the single nanoparticle spectrum and the ensemble properties [77].

The shape and composition of nanoparticles are, in other words, extremely important for their optical properties. Further, how the these properties are probed can yield completely different results as different resonances can be excited, with different properties both spectroscopically and in terms of localization. The simple illustrations in Figure 2.4 and 2.5 show the extreme tunability and vast possibilities that can be achieved with nanoplasmonics. However, these properties merely scratches the surface of the interesting optical properties that have been reported on plasmonic nanostructures, as noted in the introduction of this Chapter. However, also relatively simple structures can show very interesting optical properties, when placed in an array. More about these macroscopic optical properties can be found in Chapter 3.

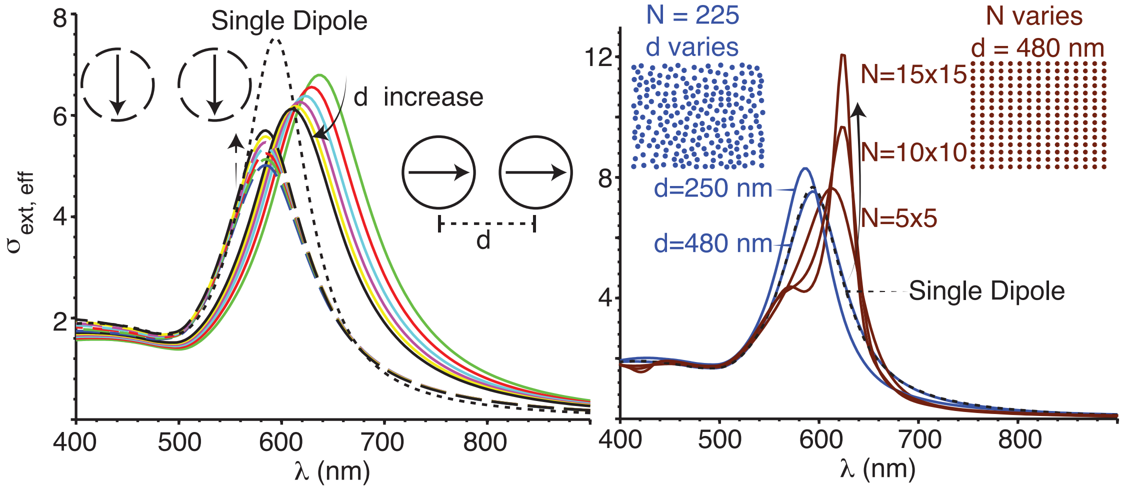

Figure 2.6: Dipolar interactions in (A) dimers and (B) arrays. (A) When nanoparticles are placed in close vicinity of one another, the resonances shift, due to strong interactions in the optical near-field. Here, the distance between the dipoles is changed from $d = 5$ nm to $d = 50$ nm. (B) Strong interactions can also couple nanoparticles on longer distances from each other, through the optical far fields, giving rise to so-called diffractive coupling effects or collective resonances, as illustrated in the calculations based on the periodic array (red). Decreasing the periodicity in the array, also decrease the effect of the far-field coupling. A random array (blue), with a minimum nearest-neighbor distance, d, show very similar optical properties to the single dipole. The calculations are based on an spheroidal gold nanoparticle, with minor and major axis of 22 and 50 nm, respectively. The gold permittivity is modeled by experimental data [63].

Chapter 3

Optical Properties of Nanoparticle Arrays

Contrary to the common behavior of individual nanoparticles, the optical properties of two-dimensional arrays of nanoparticles are highly sensitive to the excitation conditions. Isotropic nanoparticle arrays can either be described by an effective refractive index of a three dimensional medium or as a two-dimensional interference phenomenon[68, 78–84].

Effective medium theories have been around for a long time. The idea is to assign an effective refractive index or permittivity to a material with a more complicated composition, such as metallic inclusions on an interface. For example, the Maxwell Garnett or the Yamaguchi effective medium theories combine the permittivity of the inclusions, and their respective volume concentrations, to arrive at effective macroscale parameters that yield the correct far-field [78–81]. A metamaterial, or equivalently a metasurface, is composed of so-called meta-atoms, for instance small metal nanostructures, that yield designable macroscopic optical properties. Typically, the optical properties of the metamaterial cannot be found in Nature, but is synthesized for a given application. The meta-atoms should be sub-wavelength and generally assumed to be spatially separated and non-interacting. Naturally, the fields within the metamaterial layer are not described correctly by such an approach, as the fields are smeared out, or averaged, within the entire medium. Metallic nanoparticles within the medium would still concentrate the light close to the metallic surface, but these effects are not taken into account. Metamaterials can, for instance, be designed to facilitate negative refraction and superlensing effects, enhanced optical chirality or anomalous reflections[12, 52, 85]. However, the effective medium theories are indeed helpful in interpreting complex media, and have been used successfully to describe far field reflection and transmission spectra from plasmonic nanoparticle arrays fabricated on a dielectric support [82–84]. In the following section, the 2D-description is introduced, which has been the basis of the work in this thesis.

3.1 Reflecting on Reflections

The samples under investigation here are mainly prepared by Hole-Mask Colloidal Lithography (HCL) [86]. Characteristic for these types of samples is the bright colors that is evident from simple visual inspection, as seen in Figure 4.1. These colors generally stem from the sample specific absorption of optical wavelength bands in close relation to the plasmon resonance wavelength. A sample with a plasmon resonance far in the red part of the spectrum therefore look blue or blue-greenish under normal illumination conditions.

Generally, HCL samples are used to fabricate arrays of nanoparticles or nanoholes in thin films, however more exotic designs can be produced as well, such as homo- and hetero dimers, nanosandwiches, nanocones, etc[86–88]. The fabrication technique utilizes charged polystyrene beads that due to mutual Coulombic repulsion form arrays with a characteristic short range order, but without any significant long range order, as seen in Figure 3.2 A. It follows that the structures are only weakly interacting as there is no geometrical resonance present in the spectra. The nearest neighbor, center-to-center, distance is generally 2-3 bead diameters which leads to spectra similar to the expected single particle spectrum. Lastly, the randomness and the possibility of relatively large filling factors lead to meta-material-like properties of the sample. For example, the scattering from randomly arranged identical nanoparticles will add up coherently at the reflection angle, as the phase difference of the excitation (of the incident light) and the re-emission (scattering) cancel in this direction. This can be used to describe reflections from bulk material interfaces where an infinite number of dipoles at the interface add up in phase at the reflection angle, see Figure 3.1. While coherent scattering is the dominating effect, there is also diffuse scattering due to the lack of long-range order in the array, imperfections in the array, nanoparticle inhomogeneities, etc.

One should, however, be careful to assume a single particle-like spectra in reflections from a sample fabricated using the HCL method. Although the scattering from the nanoparticles add up in phase in the reflection angle, there is always a contribution from the support on which the structure is fabricated. The reflection spectra can show either peaks, dips or anything in between, if the experiment is not designed with the two component interference in mind. The spectroscopic extrema are thus not solely related to the plasmon resonance, as will be described in further detail in the following sections.

3.2 Nanoparticle Arrays as a Metasurface

There are (at least) two equivalent methodologies to derive the optical properties of a nanoparticle array metasurface [68, 89]. The first one utilizes Maxwell's equations in the boundary in order to define new boundary conditions, taking into account the polarizabilities of the nanoparticles [68]. The second metasurface approach is based on the interference between the reflectance from the nanoparticle layer and the reflection from the interface on which the nanoparticles are supported [89]. These two approaches are equivalent, as they result in the same Fresnel coefficients. In this section, the modified Fresnel coefficients will be derived using the modified boundary conditions and it will also be shown that these are equivalent to the second approach.

The first assumption is to describe the nanoparticles as point dipoles, aligned

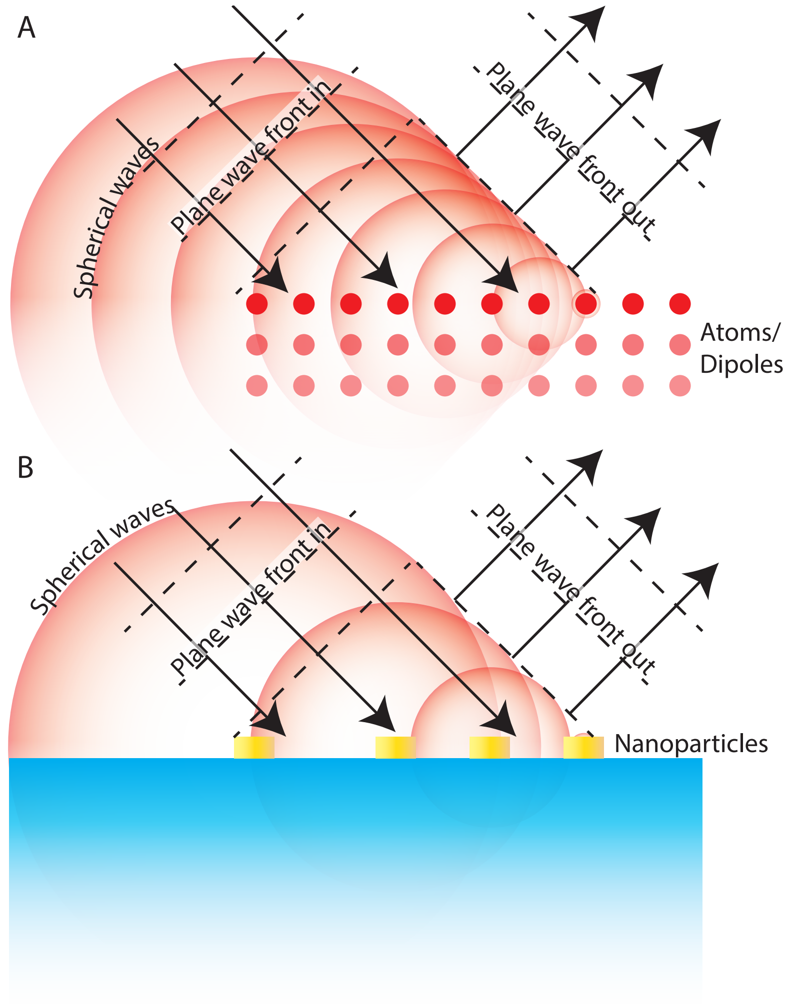

Figure 3.1: Reflection of a plane wave as a result of scattering. (A) For a general dielectric interface the atoms to the right are illuminated and excited later than the atoms to the left. The phase difference acquired cancel at the reflection angle, where the spherical waves scattered from the atoms again add up in phase. For clarity, the spherical waves illustrated in this cartoon originates only from the top layer of atoms. (B) Similarly, for an nanoparicle array without long range order, the phase delays of excitation and scattering counteract at the reflection angle.

according to the excitation polarization. With the boundaries situated in the $x - y$ plane, we may define $z = 0$ at the support/ambient interface, with positive and negative values in the ambient and supporting media, respectively. The dipole layer should then be situated somewhere between $z = 0$ and $z = h$, where h is the height of the nanoparticles.

For very thin nanoparticles, a common approximation is to define an infinitesimally thin surface comprising the nanoparticle response, in order to simplify the problem by only considering a single interface. The combined polarizabilities of the nanoparticle layer can then be described by a surface polarization, $\vec{P^s} = \rho(\alpha_x, \alpha_y, \varepsilon^+\alpha_z) \cdot \vec{E^+}$, dependant on the mean polarizability, α, and surface density, ρ, of the nanoparticles, together with the permittivity, ε, and electric field, $\vec{E}$, in the ambient medium. Maxwell's equations for non-magnetic materials are given by:

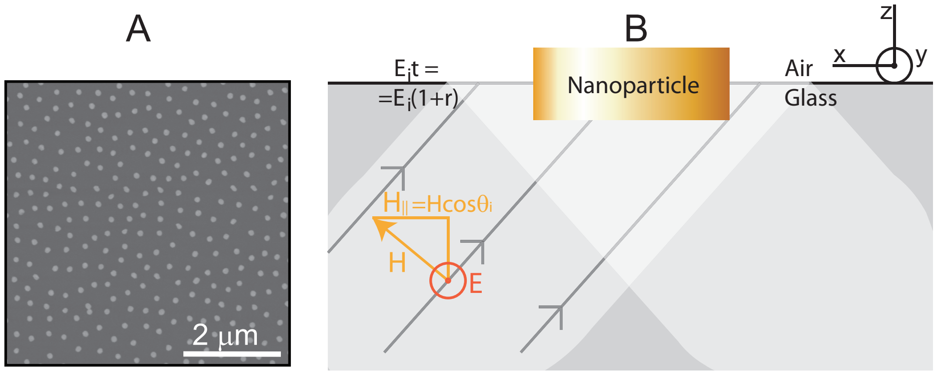

Figure 3.2: Short-range ordered gold nanodisks. (A) A scanning electron micrograph (SEM) image of 120 nm in diameter and 30 nm tall Au nanodisks fabricated by HCL. (B) Cartoon of the transverse electric fields used for deriving modified Fresnel reflection coefficients for nanoinclusions in a dielectric boundary.

$$\vec{\nabla} \cdot \varepsilon \vec{E} = 0, \tag{3.1a}$$

$$\vec{\nabla} \cdot \vec{H} = 0, \tag{3.1b}$$

$$\vec{\nabla} \times \vec{E} = -\frac{1}{c}\frac{\partial \vec{H}}{\delta t}, \tag{3.1c}$$

$$\vec{\nabla} \times \vec{H} = \frac{\varepsilon}{c}\frac{\partial \vec{E}}{\delta t}. \tag{3.1d}$$

Generally, applying equations (3.1a)-(3.1d) to any dielectric boundary results in well-known boundary conditions, from which Fresnel reflection and transmission coefficients can be derived. However, the nanoparticle surface polarization lead to modified boundary conditions, due to the abrupt jumps in the fields at the boundary. All fields are not only described with the components residing in the ambient and supporting media, but also with a surface contribution. As an example, we may write the electrical fields as $\vec{E} = \vec{E^-}\Theta(-z) + \vec{E^s}\delta(z) + \vec{E^+}\Theta(z)$, where Θ and δ are the Heaviside and Dirac delta functions, respectively. Naturally, any differentiation along the z-component will result in new boundary conditions, compared to the more natural case with no surface contribution. The modified boundary conditions, for a non-magnetic system, may be written as [68]:

$$D_z^+ - D_z^- = -\nabla_{||} \cdot P_{||}^s, \tag{3.2a}$$

$$B_z^+ = B_z^-, \tag{3.2b}$$

$$E_{||}^- - E_{||}^- = -\nabla_{||} P_z^s, \tag{3.2c}$$

$$H_{||}^- - H_{||}^- = i\frac{\omega}{c}\vec{z} \times P_{||}^s, \tag{3.2d}$$

The reflection coefficients may be retrieved from, for instance, equation (3.2d). For simplicity, the out-of-plane polarizability and hence P_z^s is set to zero, as $\alpha_z \ll \alpha_{||}$ for thin nanoparticles in the wavelength ranges considered in this thesis, although including the out-of-plane polarizability is straightforward [68, 82, 84]. For isotropic nanoparticles, transverse electric (TE or s-polarization) and transeverse magnetic (TM or p-polarization) modes may be solved for separately.

For TE, the polarization is along the y-axis and the term $\vec{z} \times \vec{P} = -\rho\alpha_{||} E_{exc}\vec{x}$. With field incident from the supporting medium side, i.e. from $z < 0$, $\vec{E_{exc}} = E_t\vec{y} = (E_i + E_r)\vec{y}$, where the subscripts i, r and t denote the incident, reflected and transmitted fields, respectively. Furthermore, $H_{||}^{-} = n_i(-E_i + E_r)\cos\theta_i\vec{x}$ and $H_{||}^{+} = -n_t E_t \cos\theta_t\vec{x} = -n_t(E_i + E_r)\cos\theta_t\vec{x}$, which lead to the following boundary condition:

$$n_t(E_i + E_r)\cos\theta_t + n_i(-E_i + E_r)\cos\theta_i = i\frac{\omega}{c}\rho\alpha_{||}(E_i + E_r), \tag{3.3}$$

which yields the following modified Fresnel coefficient:

$$r^{TE} = \frac{E_r^{TE}}{E_i^{TE}} = \frac{n_i\cos\theta_i - n_t\cos\theta_t + i\frac{\omega}{c}\rho\alpha_{||}}{n_i\cos\theta_i + n_t\cos\theta_t - i\frac{\omega}{c}\rho\alpha_{||}}. \tag{3.4}$$

Still $t_s = r_s + 1$, which lead to the transmission coefficient:

$$t^{TE} = \frac{E_t^{TE}}{E_i^{TE}} = \frac{2n_i\cos\theta_i}{n_i\cos\theta_i + n_t\cos\theta_t - i\frac{\omega}{c}\rho\alpha_{||}}. \tag{3.5}$$

Further, for TM, the polarization is paralell to the x-axis and therefore the right hand term of equation (3.2d) equals $i\frac{\omega}{c}\rho\alpha_{||}E_{exc}\vec{y}$, where $E_{exc} = \cos\theta_t E_t = \cos\theta_i(E_i - E_r)$. On the left-hand side $H_{||}^{-} = n_i(E_i + E_r)\vec{y}$ and $H_{||}^{+} = E_t\vec{y}$ and thus:

$$n_t E_t - n_i(E_i + E_r) = i\frac{\omega}{c}\rho\alpha_{||}\cos\theta_i(E_i - E_r), \tag{3.6}$$

from which the reflection and transmission coefficients can be extracted, by using $\cos\theta_t E_t = \cos\theta_i(E_i - E_r)$:

$$r^{TM} = \frac{n_t\cos\theta_i - n_i\cos\theta_t - i\frac{\omega}{c}\rho\alpha_{||}\cos\theta_i\cos\theta_t}{n_t\cos\theta_i + n_i\cos\theta_t - i\frac{\omega}{c}\rho\alpha_{||}\cos\theta_i\cos\theta_t}, \tag{3.7}$$

$$t^{TM} = \frac{2n_i\cos\theta_i}{n_t\cos\theta_i + n_i\cos\theta_t - i\frac{\omega}{c}\rho\alpha_{||}\cos\theta_i\cos\theta_t}. \tag{3.8}$$

It is a simple task to convince oneself that these reflection coefficients result from the interference between the direct reflections from a bare interface, without the nanoparticle array, and the collective scattering (or reflection) from the array itself. For TE and TM polarization, respectively, such a two-layer interference phenomenon may be written as:

$$r_{tot}^{TE} = r_0^{TE} + \frac{(1 - (r_0^{TE})^2)r_{NP}^{TE}}{1 + r_{NP}^{TE}r_0^{TE}}, \tag{3.9a}$$

$$r_{tot}^{TM} = r_0^{TM} + \frac{(1 - (r_0^{TM})^2)r_{NP}^{TM}}{1 + r_{NP}^{TM}r_0^{TM}}, \tag{3.9b}$$

where the subindices 0 and NP denote the bare interface reflection and the nanoparticle array reflections, respectively. The r_0 terms are the same as for usual media, i.e. they may be found by removing the α-dependent terms in equations (3.4) and (3.7), while r_{NP} is found by placing the array in a homogeneous medium, here in the ambient. The resulting reflection coefficients are indeed identical to equation (3.4) and (3.7). Similar reflection coefficients can also be derived using the coupled dipole approximation (CDA), from which the same reflection coefficients emerge [89].

3.3 Reflecting Fano Resonances

The reason why the metasurface description previously introduced is so appealing is the simplicity of analysis. As noted above, the total reflection from the interface supporting nanoparticles can be described as an interference between the reflections from the bare interface itself, neglecting any nanoparticle contributions, and the coherent scattering in the reflection angle emerging from the array. As the bare interface reflection between two non-absorbing media with negligable dispersion is spectroscopically flat and the typical metal nanoparticle scattering have a Lorentzian spectral response, the resulting line shape will greatly depend on the respective strengths of these components. Line shapes emerging from the interference between a sharp Lorentzian response and a much broader continuum is commonly described as a Fano resonance, with a line shape given by [54, 90, 91]:

$$I_F = y_0 + H\frac{(q+\epsilon)^2}{1+\epsilon^2}, \tag{3.10}$$

where y_0 is a background term, H is the resonance amplitude, q the asymmetry factor and $\epsilon = (\omega - \omega_F)/\Gamma$ is a dimensionless energy, with E denoting energy, E_{res} the resonance energy, and Γ the half width of the resonance. The maximum and minimum positions are given by $\omega_{max} = \Gamma/q + \omega_F$ and $\omega_{min} = -\Gamma q + \omega_F$, respectively. Large and small $|q|$ are associated with spectral peak and dip positions near ω_F, respectively.

Given a Lorentzian in-plane polarizability of the inclusions in the boundary, $\alpha_{||}$, all the parameters in equation (3.10) can explicitly be found from equation (3.4) and (3.7). Figure 3.3 A show a surface plot of normalized TE reflection spectra, calculated from equation (3.4), where the main features of the line shape can be seen. Analytic expressions for the angular dependence of the maximum, minimum and Fano resonance positions are plotted, together with the spectral width of the Fano resonance. $\rho\alpha_{||}$ is described by a Lorentzian polarizability:

$$\rho\alpha_{||} = A'\frac{\gamma_0}{\omega_P - \omega - i\gamma_0}, \tag{3.11}$$

with $\omega_P = 1.91$ eV, $\gamma_0 = 0.09$ eV and $A' = 3.4 \cdot 10^{-7}$ m. Depending on the amplitude of the product $\rho\alpha_{||}$, the reflection line shapes below the critical angle either contains distinct peaks (resonances) or dips (anti-resonances) for a given incident angle. Typically for rather dense samples, or inclusions with a large α, there are resonant states at low incident angles, which changes into anti-resonances at larger angles, as the reflectance from the bare interface increases. During the transition from resonance to anti-resonance, the line shape supports highly dispersive spectral features, as illustrated in Figure 3.3 A.

The Fano parameters are found by identification from $I_F = |r_{p,s}|^2$, using $A = A'/c$, $a_s = n_i \cos\theta_i$, $b_s = n_t|\cos\theta_t|$, $a_p = n_t \cos\theta_i$, $b_p = n_i|\cos\theta_t|$ and $d_p = |\cos\theta_t|\cos\theta_i$. This results in the following resonance conditions:

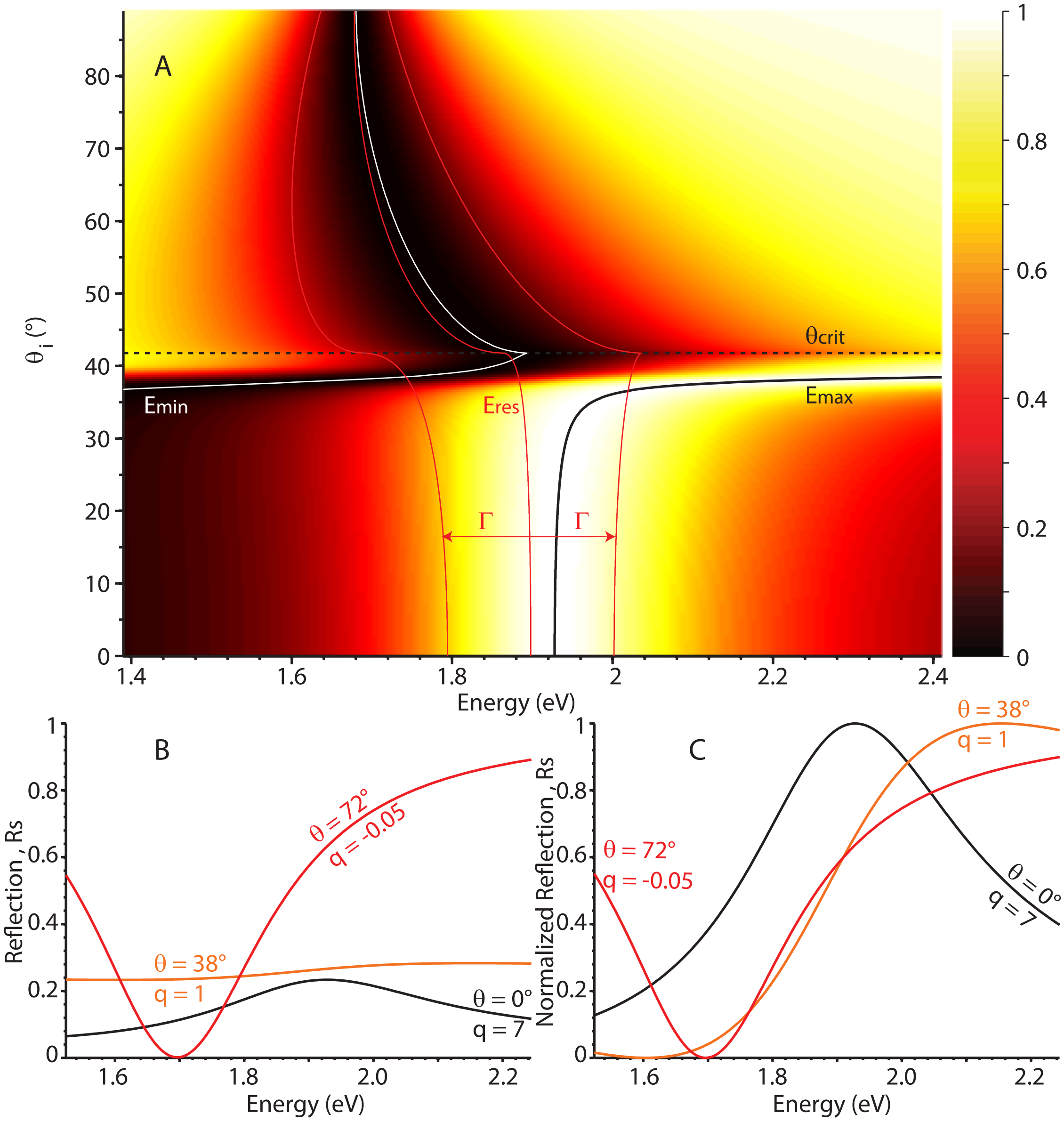

Figure 3.3: The angular dependence of the spectral line shapes calculated using the equation 3.4. (A) Normalized reflection line shapes calculated with $n_i = 1.5$, $n_t = 1$, $\alpha_{||}$ modeled as a Lorentzian, i.e. $\rho\alpha = A\gamma_0/(E_0 - E - i\gamma_0)$. The surface plot show normalized TE-reflection spectra together with analytically calculated maximum, minimum and Fano resonance positions. (B-C) The interference between the Lorentzian polarizability and the flat dispersion of the reflection from the n_t/n_i-interface lead to spectral peaks ($\theta_i = 0°$), dips ($\theta_i = 72°$) and asymmetric resonances ($\theta_i = 38°$). The destructive interference above the critical angle lead to perfect absorbance at 1.7 eV around $\theta_i = 72°$.

$$\omega_{F,s} = \begin{cases} \frac{(a_s^2+b_s^2)\omega_P + A\gamma_0(b_s\omega_P - a_s\gamma_0)}{a_s^2+(b_s+A\gamma_0)^2}, & \theta_i > \theta_c \\ \frac{\omega_P-(A\gamma_0^2)/(a_s+b_s)}{1+A^2\gamma_0^2/(a_s+b_s)^2}, & \theta_i < \theta_c, \end{cases} \tag{3.12a}$$

$$\omega_{F,p} = \begin{cases} \frac{(a_p^2+b_p^2)\omega_P - Ad_p\gamma_0(a_p\omega_P + b_p\gamma_0)}{b_p^2+(a_p-Ad_p\gamma_0)^2}, & \theta_i > \theta_c \\ \frac{\omega_P-Ad_p\gamma_0^2/(a_p+b_p)}{1+(A^2d_p^2\gamma_0^2)/(a_p+b_p)^2}, & \theta_i < \theta_c. \end{cases} \tag{3.12b}$$

Moreover, the spectral line widths of the Fano resonance can be written as:

$$\Gamma_s = \begin{cases} \gamma_0 \frac{a_s(a_s+A\omega_P)+b_s(b_s+A\gamma_0)}{a_s^2+(b_s+A\gamma_0)^2}, & \theta_i > \theta_c \\ \gamma_0 \frac{(a_s+b_s)(a_s+b_s+A\omega_P)}{(a_s+b_s)^2+A^2\gamma_0^2}, & \theta_i < \theta_c, \end{cases} \tag{3.13a}$$

$$\Gamma_p = \begin{cases} \gamma_0 \frac{a_p(a_p-Ad_p\gamma_0)+b_p(b_p+Ad_p\omega_P)}{b_p^2+(a_p-Ad_p\gamma_0)^2}, & \theta_i > \theta_c \\ \gamma_0 \frac{(a_p+b_p)(a_p+b_p+Ad_p\omega_P)}{(a_p+b_p)^2+A^2d_p^2\gamma_0^2}, & \theta_i < \theta_c). \end{cases} \tag{3.13b}$$

Finally, there are the Fano parameters, which are given by:

$$q_s = \begin{cases} \frac{\omega_{F,s}-\sqrt{\omega_{F,s}^2+\Gamma_s^2}}{\Gamma_s}, & \theta_i > \theta_c \\ -\frac{A\omega_{F,s}\gamma_0^2+b_s(\Delta\omega_{F,s}^2+\Delta\Gamma_s^2)+\frac{a_sA^3\gamma_0^3/\rho|\alpha_0|}{(a_s+b_s)^2+A^2\gamma_0^2}\sqrt{(1+\delta_{sq}}}{(2b_s\Delta\omega_{F,s}-A\gamma_0^2)\Gamma_s}, & \theta_i < \theta_c, \end{cases} \tag{3.14a}$$

$$q_p = \begin{cases} \frac{-\Gamma_p}{\omega_{F,p}+\sqrt{\omega_{F,p}^2+\Gamma_p^2}}, & \theta_i > \theta_c \\ \frac{(2a_p\Delta\omega_{F,p}-Ad_p\gamma_0^2)\Gamma_p}{Ad_p\omega_P\gamma_0^2+\frac{A^3b_pd_p^2\gamma_0^3/\rho|\alpha_0|\sqrt{(1+\delta_{pq}}}{(a_p+b_p)^2+A^2d_p^2\gamma_0^2}+a_p(\Delta\omega_{0,p}^2+\Delta\Gamma_p^2)}, & \theta_i < \theta_c. \end{cases} \tag{3.14b}$$

Here, $\Delta\omega_{F,s} = \omega_P - \omega_{F,s}$, $\Delta\Gamma_s^2 = \gamma_0^2 - \Gamma_s^2$, $\delta_{qs} = \left(\frac{a_s^2-b_s(b_s+A\omega_{F,s})}{a_sA\gamma_0}\right)^2$ and $|\alpha_0| = |\alpha(\omega = 0)|$. Furthermore, for p-polarization $\Delta\omega_{F,p} = \omega_P - \omega_{F,p}$, $\Delta\Gamma_p^2 = \gamma_0^2 - \Gamma_p^2$ and $\delta_{pq} = \left(\frac{b_p^2-a_p(a_p+Ad_p^2\omega_P)}{A^2b_p^2d_p^2\gamma_0^2}\right)^2$. Some of these equations may seem complicated and therefore of limited use. However, the formulas given in equation (3.12)-(3.14) proves the Fano nature of the far-field properties of nanoparticle arrays on an interface. The Fano resonance is sometimes described through different excitation pathways as q was originally described as the ratio between the transition probabilities to the modified discrete and unperturbed continuum states [90]. A large q therefore imply a lower probability of the excitation to the continuum, while for a low q this transition is more likely. Consequently, the continuum, that is, the interface reflectance, perturbs the plasmonic states with different amounts depending on the individual strengths of the two components, related to the refractive index of the surrounding media, the incidence angle and the surface density and other optical proberties of the nanoparticles.

Therefore, the nanoscale plasmonic excitations may be controlled macroscopically, by tuning properties such as the excitation polarization and incidence angle. In fact, the excitation and absorption efficiency of the nanoparticle array is easily controllable and can even lead to complete absorption of the incident light, as described in the following section.

3.4 Perfect Absorption

Transmission is nullified above the critical angle. Therefore, the distinct minimum in the reflection spectra denotes the position of maximized absorption. Such a minimum can be deep enough to achieve $R = 0$ and $T = 0$ simultaneously, as illustrated in Figure 3.3 B. Even though the reflectance at normal incidence show a relatively weak spectral peak at the Lorentzian resonance position, perfect absorbance is achieved around 1.7 eV at an incident angle of 72°.

So-called coherent perfect absorption is based on the time-reversal of the eigenmodes of a system [92–94]. Here it is shown that the modified Fresnel coefficients previously presented is equivalent to time reversed eigenmodes of the surface and therefore can be classified as *coherent* absorption.

In the following, the dispersion relation of surface modes residing in the metasurface is derived. Surface modes are bound to the interface between two materials and decay exponentially perpendicular to the surface. In order to derive the dispersion of such a surface mode, a bound wave is assumed, propagating along the surface between a substrate and an ambient medium with dielectric constants ε^- and ε^+, respectively. Following [95], with the boundary in the $x-y$ plane, the surface mode's fields may have the following solution:

$$\vec{E} = \begin{cases} E^- e^{k_z^- z} e^{i(k_x x - \omega t)}, z \leq 0 \\ E^+ e^{-k_z^+ z} e^{i(k_x x - \omega t)}, z > 0, \end{cases} \tag{3.15a}$$

$$\vec{H} = \begin{cases} H^- e^{k_z^- z} e^{i(k_x x - \omega t)}, z \leq 0 \\ H^+ e^{-k_z^+ z} e^{i(k_x x - \omega t)}, z > 0. \end{cases} \tag{3.15b}$$

Here the notation implies that $k_z^{\pm}$ should be real and positive. Applying equation (3.1a)-(3.1d) on equation (3.15a)-(3.15b) make the separation of transverse electric (TE) and transverse magnetic (TM) modes evident, as E_y, H_x and H_z as well as E_x, E_z and H_y form two interacting subgroups. However, both the TE and the TM modes have similar properties of the perpendicular k-component:

$$k_z^{+2} = k_x^2 - \varepsilon^+ \left(\frac{\omega}{c}\right)^2, \tag{3.16a}$$

$$k_z^{-2} = k_x^2 - \varepsilon^- \left(\frac{\omega}{c}\right)^2. \tag{3.16b}$$

Proper boundary conditions must be used in order to find the dispersion relations for the surface modes. As in the derivation of the modified Fresnel coefficients, the continuity of the H-fields is lost for a surface polarizability parallel to the surface. Furthermore, also the continuity of D_z across the surface is effected.[68] In this derivation the polarizability of the out-of-plane dipole, α_z, is neglected, although one may derive similar modes when a significant α_z is present, in which case the continuity of the parallel E-fields also may also be lost [68]. For a non-zero in-plane polarizability, $\alpha_{||}$, and out-of-plane polarizability, α_z, the boundary conditions are given by equations (3.2a)-(3.2d).

We first analyze TE-modes. Normally, these modes are not supported in non-magnetic materials. However, utilizing the modified boundary condition in equation (3.2d), a mode can be found that fulfills the condition:

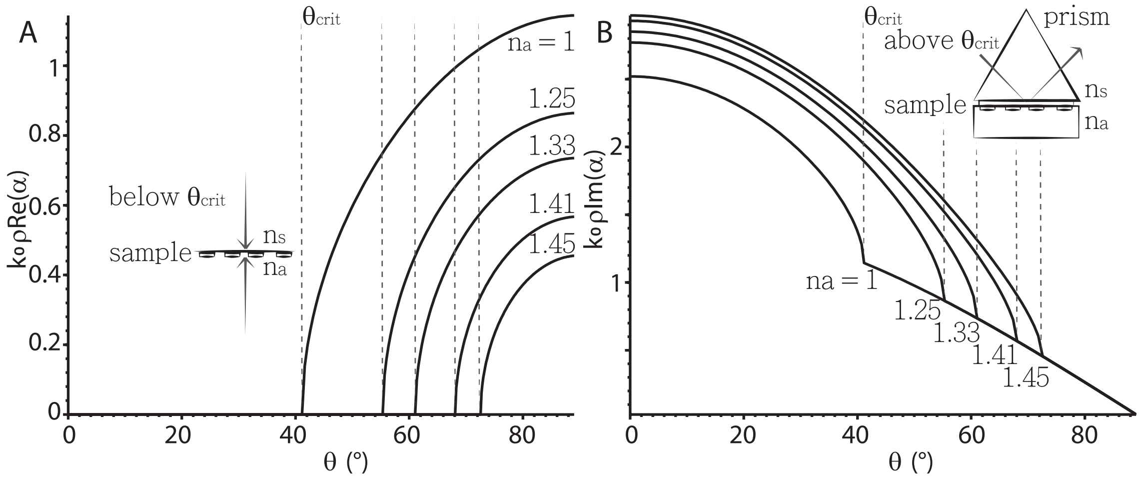

Figure 3.4: Coherent perfect absorption criteria. For a given dielectric boundary, n_s/n_a, and incidence angle, θ_i, there is a matching condition for complete absorption of light, given by the time-reversal of equation (3.19). Consequently, by having two coherent beams incident from opposing sides of the boundary can result in coherent perfect absorption for incidence angles below the critical angle, θ_c, while illumanation with $\theta_i \geq \theta_c$ only need a single incident beam, as illustrated in the inset cartoons.

$$k_z^+ + k_z^- = \left(\frac{\omega}{c}\right)^2 \rho\alpha_{||}, \tag{3.17}$$

which, together with equation (3.16a) and (3.16b), yields new expressions for $k_z^{\pm}$:

$$k_z^{\pm} = \frac{1}{2}\left[\left(\frac{\omega}{c}\right)^2 \rho\alpha_{||} \pm \frac{\Delta\varepsilon}{\rho\alpha_{||}}\right], \tag{3.18}$$

where $\Delta\varepsilon = \varepsilon^- - \varepsilon^+$. Using $\rho\alpha_{||} = \rho(\alpha_{||}^{'} + i\alpha_{||}^{''})$ equation (3.18) may be written on the form:

$$k_z^{\pm} = \frac{1}{2}\left(\rho\alpha_{||}^{'}\left[\left(\frac{\omega}{c}\right)^2 \pm \frac{\Delta\varepsilon}{|\rho\alpha_{||}|^2}\right] + i\rho\alpha_{||}^{''}\left[\left(\frac{\omega}{c}\right)^2 \mp \frac{\Delta\varepsilon}{|\rho\alpha_{||}|^2}\right]\right), \tag{3.19}$$

The real parts of $k_z^{\pm}$ must be positive for any physical modes, i.e. $\left(\frac{\omega}{c}\right)^2 \geq \frac{\Delta\varepsilon}{|\rho\alpha_{||}|^2}$, which here mean that there are no pure surface modes in the system, as both k_z^+ and k_z^- can not be purely real and positive simultaneously. A bound mode in above the interface ($\left(\frac{\omega}{c}\right)^2 = \frac{\Delta\varepsilon}{|\rho\alpha_{||}|^2}$) needs to be supplied with energy from below, as k_z^- is positive and imaginary. Such modes are termed lateral modes and are related to the so-called Goos-Hänchen effect [96, 97]. It can be shown that the case of $R_s = 0$ above the critical angle corresponds to such lateral modes.

Now turning the focus towards the TM-mode, only E_x, E_z and H_y in equation (3.15a) and (3.15b) are nonzero. By solving the equation system using equation (3.16a) and (3.16b), an indirect expression for the dispersion of the TM-mode is obtained:

$$\frac{\varepsilon^+}{k_z^+} + \frac{\varepsilon^-}{k_z^-} = -\rho\alpha_{||}. \tag{3.20}$$

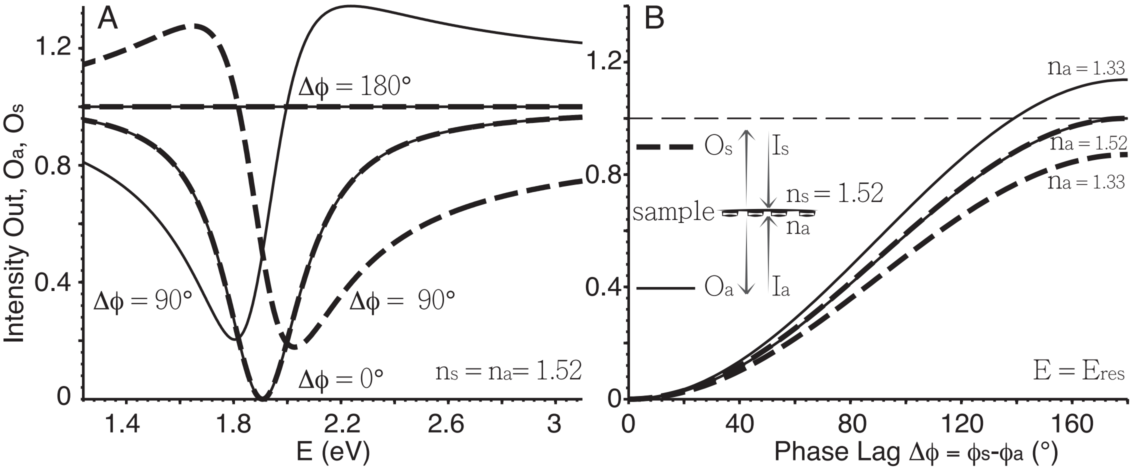

Figure 3.5: Calculated coherent absorption at normal incidence using two coherent beams from opposing sides. (A) In a symmetric environment, $n_s = n_a = 1.52$, a layer of absorbing nanoinclusions with a Lorentzian polarizability can be tuned into a perfect absorption condition, as the light output into respective media, O_s and O_a cen be nullified. $O_s = O_a = 0$ occurs if the two incident beams, I_s and I_a, are in phase, $\Delta\phi = \phi_s - \phi_a = 0°$, and have the same amplitude. Adjusting $\Delta\phi$ decreases the absorption until $\Delta\phi = 180°$, when the layer is completely transparent. (B) Studying the output at the resonance energy, E_{res} as a function of $\Delta\phi$ illustrates the control of absorption that could be obtained. The directionality of the output is symmetric in a symmetric environment, but using $n_a \neq n_s$ result in more light emitted into the lower refractive index media.

From equation (3.20) we find that light bound above the interface corresponds to lateral modes that needs to be pumped from below. Again, the condition for $R_p = 0$ fulfills such a condition.

In both the TE- and the TM-polarized case, the excitation of lateral modes implies that the incident momentum along the surface is conserved, $k_{||}^{inc} = \frac{\omega}{c} n_s \sin\theta_i = k_x$, where $n_s^2 = \varepsilon^-$ and $n_a^2 = \varepsilon^+$ are the refractive indices of the ambient and the substrate, respectively. Inserting the incident momentum into equation (3.17) and (3.20), result in the same coupling condition as for $\rho\alpha_{||} = \rho\alpha_{||}|_{R_{s,p}=0}$. The latter may be found from the numerator of equation (3.4) and (3.7), respectively. These are:

$$\rho\alpha_{||}|_{R_{s,TE}=0} = \frac{n_a|\cos\theta_t|}{\frac{\omega}{c}} + i\frac{n_s\cos\theta_i}{\frac{\omega}{c}}, \tag{3.21a}$$

$$\rho\alpha_{||}|_{R_{p,TM}=0} = \frac{-n_a}{\frac{\omega}{c}|\cos\theta_t|} + i\frac{n_s}{\frac{\omega}{c}\cos\theta_i}. \tag{3.21b}$$

Equation (3.21a) and (3.21b) mean that the light is incident from the substrate side, but is then refracted into the medium above the interface in which it is propagating along the x-direction, while being pumped from below. In this formalism, such modes have very long (even diverging) propagation lengths, as long as energy is supplied from below the interface.

From the discussion above, complete absorption can be achieved by illumination from the high index side, when illuminated above the critical angle. The conclusion is that imposing $R = T = 0$ in equation (3.4) and (3.7) is the same as some of the time reversed surface modes found in equation (3.19) and (3.20). However, from the dispersion relations of the surface modes, there also exist perfect absorption conditions using two incident beams, incident below the critical angle from opposing sides of the surface. In the two-beam configuration, the respective transmission and reflection beams will interfere destructively on both sides of the interface.

The coherent perfect absorption criteria for different media and incidence angles are plotted in Figure 3.4. Below the critical angle, the coherent perfect absorption occurs at the point where the real part of α is zero. For a Lorentzian polarizability, $\mathrm{Re}\,\alpha = 0$ occurs close to the resonance position, where the polarizability is the strongest. As a consequence, achieving complete absorption at θ_c requires the smallest ρ, for a given Lorentzian α. Further, as θ_c increases with decreasing dielectric contrast of the interface, a smaller difference between the support and ambient refractive index decreases the surface density needed for 100% absorption.

Figure 3.5A show spectra emerging from the interface when illuminated coherently at $\theta_i = 0°$ from both sides of the interface. When two beams are in-phase, in accordance with equation (3.19), the spectra show no light emitted into either media. It is also possible to coherently control the absorption in these metasurfaces by altering the phase difference between the two beams. The absorption could then be coherently controlled by a control beam, as shown in Figure 3.5B. Depending on the interface dielectric contrast, the output into respective media can also be manipulated.

The possibility of zero reflection and perfect absorption could be of potential use for both refractive index sensing and surface enhanced spectroscopy applications. The phase associated with near zero reflections are expected to vary rapidly across the resonance condition in a similar way to the rapid phase changes observed in p-polarized reflections near the surface plasmon polariton in thin films [98–104]. Using the polarizabilities of ellipsoidal gold nanoparticles situated in a glass/water interface, as seen in Figure 3.6, and by varying the surface coverage of the nanoparticles, the minimum reflected intensity varies as well. As ρ is altered towards the zero coupling condition, Figure 3.6 shows that the reflected phase changes more and more rapidly, which indicates that a small resonance shift yields a large response in the reflected phase. Therefore, the system should be promising to be used, for instance, in refractive index sensing applications.

Further, in the calculated system of Figure 3.3 and 3.6 the only absorbing material is the nanoparticles, meaning that all light is absorbed in them, resulting in enhanced optical near fields. If the nanostructures could be designed to further concentrate the light using, for instance, dimers or nanocones, some areas near the nanostructures could support extremely intense fields. The systems may therefore by applicable in techniques that directly rely on the intensity of the light, such as surface enhanced spectroscopies, optical trapping and catalytic activities [16–19, 21, 56, 58, 105–111].

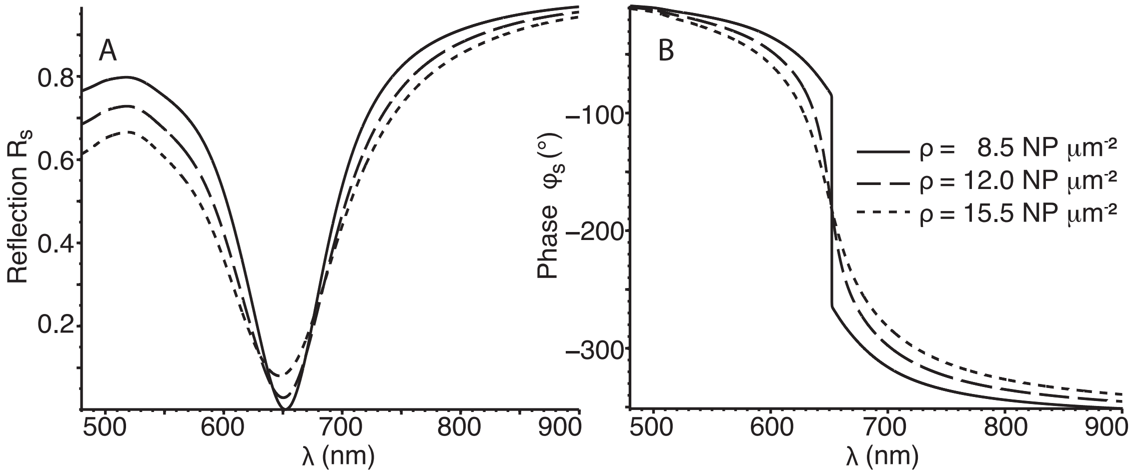

Figure 3.6: Reflection properties of s-polarized light. The reflected intensity varies much slower with wavlength than the reflected phase. Calculated using equation (3.4) with gold ellipsoids, 80 nm in diameter and 20 nm tall, at a glass/water interface illuminated with s-polarized light at 63°.

Chapter 4

Plasmonic Refractive Index Sensing

4.1 Introduction

Biosensors are generally based on three components: The biorecognition layer, the signal transducer and the read out components. In plasmonic biosensors, the transducer is supporting surface plasmons. The spectroscopic properties of the plasmon changes upon biorecognition events. The signal is most often detected with additional optical components, such as a spectrometer or a photodiode, converting the plasmonic response to an electrical signal. The biorecognition layer could be antibodies, nucleic acids, lipid membranes etc.

Plasmonic biosensors are generally categorized as "label free" sensors, as they respond to the refractive index contrast between the sample medium and the bound molecule. The analyte does not have to be labeled by a fluorescent or enzymatic molecule to yield a signal from the sensor. Label-free techniques has several advantages, however, plasmonic sensors are not the only alternative of this type. Label-free sensors may have photonic, electronic or mechanical transducers. In recent years nanofabrication has catalyzed the development of micro- and nanosensors in all these fields, including plasmonics [112, 113]. The recent development of photonic crystals, semiconductor nanowires, carbon nanotubes and micro-cantilevers for sensing purposes are only but a few examples [29, 114–116]. The nano-sensor trend begs the question: Why is there such an interest in nanosensors? What information can a nanosensor give that macroscopic sensors miss?

One reason for the large interest in nanosensors is described by the expected kinetics of protein-protein interactions at relatively low concentrations, addressed by Squires et. al [117]. Low concentrations of targets are relevant, especially for diagnostic purposes. As an example, the authors report that with 1000 nanowires studied continuously only four would, on average, have a target protein bound. The number of bound molecules may seem very few, but consider the alternative: A macroscopic surface with the same total area and number of bound molecules. Detecting the four molecules would be most difficult as the surface density of the target is extremely low. Nanoscale sensors are described as more sensitive because of the overlap between the size of the sensor surface, or the sensing volume, and the target to be detected. A single binding event translates to a relatively large surface density coverage. Hence, the nanowires may give a detectable signal for a single

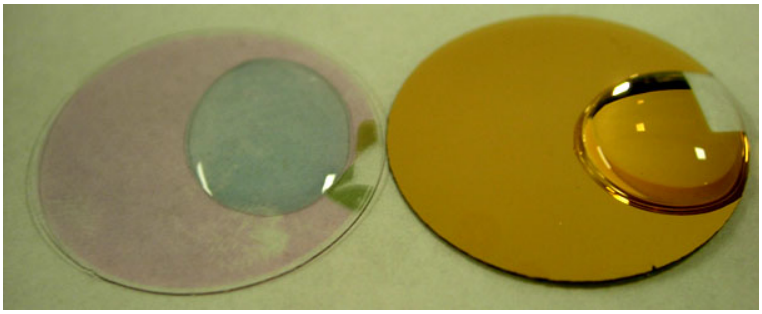

Figure 4.1: Illustration of colorimetric refractive index sensing using LSPR. The photograph shows a gold nanodisk array (left) and a thin gold film (right) with water droplets on top. The localized surface plasmon resonance in the nanodisks is always excitable, which is why a clear plasmon shift / color change can be seen between the areas covered by air and water. The surface plasmons in the thin film, on the other hand, cannot be excited without additional optics and therefore no color change can be seen.

binding event and the number of nanowires yielding such signals scales with several parameters, including the concentration and affinity of the molecular interaction. There are micro-resonators that have shown sensitivities down to single molecule levels as well, however due to very large interaction times with the analyte [25]. In practice, such a system is relatively difficult to excite as it requires rather elaborate coupling mechanisms, which are unpractical for multiplexing purposes.

Plasmonic nanoparticle arrays may serve as a viable alternative, if single molecule sensitivity can be reached for large arrays, where individual nanostructures can be interrogated individually [118–120].

Nylander et. al in 1982 and Liedberg et. al in 1983 was the first to report refractive index sensing using thin film SPRs [45, 46]. The methodology has developed throughout the years, leading to remarkable technological advancements and commercialization of instruments. Nowadays, conventional thin film SPR sensing is a mature technology, heavily utilized in industry and as a research tool and therefore serves as a natural benchmark for novel nanoplasmonic sensor alternatives [121–130]. Several technologies enabled the SPR sensing platform to evolve more quickly. These include effective surface chemistry and advanced liquid handling systems. In much the same manner, the sensing methodologies based on LSPRs are highly dependent on the development of both nanofabrication methods and electrodynamic simulations.

During the 1980's and the 1990's LSPRs were used as a contrast mechanism in biosensing and immunoassays, for example in colorimetric assays [131]. The large optical cross section of the nanoparticles can be used as labels, as they, in contrast to regular fluorescent dyes, do not bleach. Alternatively, the sensitivity of the plasmons can be used in aggregation assays, where the color will change due to the interaction between nanoparticles. It was not until 1998 that Englebienne et. al first experimentally demonstrated that the resonance position of colloidal gold nanoparticles shifted upon molecular adsorption in analogy with the thin film plasmon [132]. Even though thin film plasmonic sensing and localized plasmonic sensing have the same origin, the latter may have benefits in both cost and portability. As LSPRs have a relaxed excitation condition, the sensing instrumentation can more easily be made very compact and even small enough for hand-held devices with an additional benefit of a lower instrumental cost [133]. Additionally, the short penetration depth of LSPRs make them less sensitive to noise, such as temperature fluctuations and unbound molecules far from the metal surface.

The trend during the last decade has been more directed towards the development of refractometric LSPR sensing with plasmonically active features immobilized on substrates [134–139]. This enables convenient fluidic solutions for surface functionalization and analyte delivery. Furthermore, it opens the possibility for flexible design of both individual and arrays of nanostructures through the rapid development of nanofabrication technologies.

Although thin film- and localized plasmons have much in common, one of the distinctive differences between the two is shown in Figure 4.1. The photograph show the comparison between an array of short-range ordered 80 nm wide and 50 nm tall gold nanodisks and a 50 nm thin gold film. The LSPR of the former make the sample look red in air, but the color shifts to blue-greenish in water, due to the plasmonic sensitivity to the surrounding refractive index. The thin film, on the other hand, show the same golden color irrespective of the dielectric environment, as the surface plasmons of the film are not excited unless special illumination conditions are fulfilled.

4.2 Sensing with plasmons in thin films

In order to excite thin film plasmons with light it is necessary to match both the energy and the momentum of the incident photons with the plasmonic eigenmode of the boundary. The Surface Plasmon Polaritons (SPPs) in a metal/dielectric ambient interface has always a larger momentum than light in the ambient, making direct excitation from the ambient side impossible. The energy-momentum relationship is dictated by the plasmon dispersion, which conveniently is approximated by the dispersion of a plasmon residing in the interface between two semi-infinite materials: A metal and an ambient dielectric. The dispersion relation is solvable directly from the boundary equations and is given by equation (2.4).

Figure 4.2 illustrates the SPP dispersion at a gold/water boundary and the dispersion of light propagating along the interface in water and glass media. The dielectric function of gold is approximated by the Drude formula. As the water and SPP dispersion lines do not cross, conservation of both energy and momentum is not possible simultaneously. SPPs can therefore not be excited from the ambient side. A plasmon running along a water/gold interface is, however, excitable from a glass medium, as light in glass has an increased wave number compared to light in water. The so-called Kretschmann configuration utilizes this fact by placing a glass prism in optical contact with a thin film, exciting a plasmon on the opposite side of the film [44].

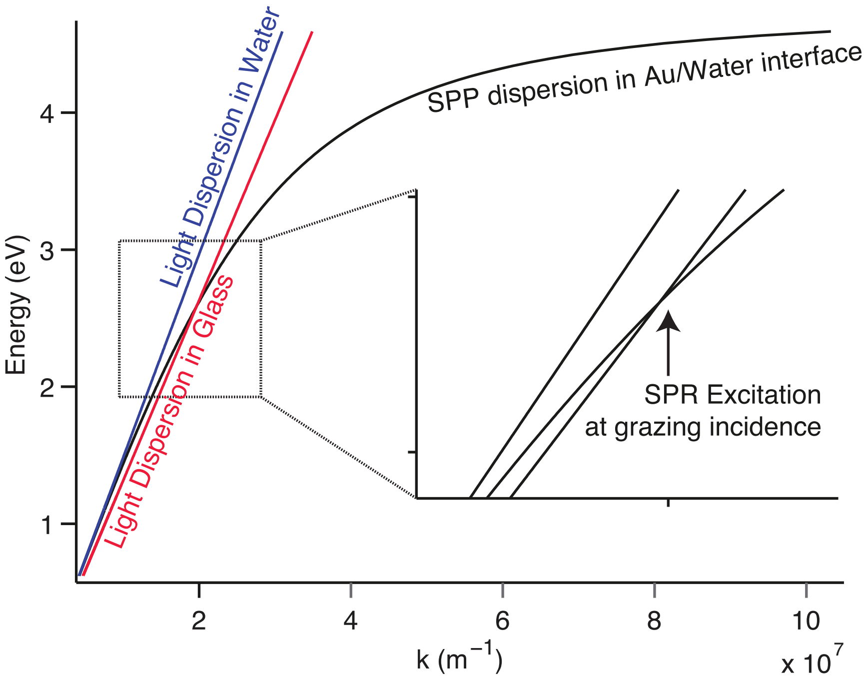

Figure 4.2: Dispersion of surface plasmons and light. The momentum of the surface plasmon at a gold-water interface is always larger than the momentum of light in water ($n = 1.33$), but the larger momentum of light in high refractive index media, such as glass ($n = 1.5$), make excitation possible through the use of a prism coupler. The figure illustrates this by visualizing that the light-line in the water never crosses the plasmon dispersion line, while the light line in glass does.

Reflection measurements in Kretschmann geometry is perhaps the most common approach to measure plasmon excitation in thin films. A dip in the reflectance indicates the absorption of light by the surface plasmon mode. The reflection can be described through combinations of Fresnel reflection coefficients for the individual interfaces:

$$R = |r_{pmd}|^2 = \left|\frac{E_r}{E_{inc}}\right|^2 = \left|\frac{r_{pm} + r_{md}e^{2ikt}}{1 + r_{pm}e^{2ikt}}\right|^2 . \tag{4.1}$$

Here r_{AB} is the Fresnel reflection coefficient between medium A and B, with respective permittivity ε; p denotes the prism, m the metal film, and d the dielectric ambient and t is the film thickness. From equation (4.1) it is clear that the reflection minimum can also be viewed as destructive interference between the light reflected from the prism/metal interface and light from the metal/ambient boundary. Optimum coupling is accomplished when the reflectance is as small as possible for a certain wavelength, which requires that the nominator in equation (4.1) is minimized. The depth of the reflectance minimum is therefore related to the thickness of the film. Consequently, for given plasmon frequency and momentum, corresponding to a certain incident angle and wavelength, optimum coupling is achieved for a specific thickness of the metal film. For gold films on glass in water and plasmon excitation in the red, the optimum film thickness turns out to be around 50 nm [130].

4.3 Nanoplasmonic Sensing

The refractometric sensitivity of metallic nanoparticles has been demonstrated for bio/chemo sensing in numerous experimental setups, combining a plentiful of target molecules and a vast amount of different nanostructures. However, in order to introduce refractometric sensing based on LSPRs, the dipolar polarizability of a conducting sphere obtained from the quasi-static approximation, given in equation (2.5), is a good starting point. The spectrally dominant term of equation (2.5) is a Lorentzian line shape. This suggest that the collective response of the conduction electrons can be modeled as a damped harmonic oscillator. The external field induces resonating surface charges producing an induced field inside and outside the particle, acting to restore charge neutrality. This restoring force decreases if the field lines pass through a medium with a high dielectric constant. Hence, refractometric plasmonic sensing is ultimately a product of the dielectric screening of surface charges. The refractometric sensitivity of a plasmon is related to the ease of electron polarization and the strength of the restoring force. The sensitivity is therefore related to the material properties of the nanoparticle, but also the geometrical shape. For example, a plasmon localized in the gap between two metal surfaces will be very sensitive to dielectric screening within the gap.

The aspects described above focused on the *bulk* refractive index sensitivity. However, the extension of the resonant field into the ambient becomes of prime importance when considering molecular adsorption at or very close to the surface of a nanostructure. Thin homogeneous layers with a given refractive index can model monolayers of molecules to some extent, but individual molecules are described by their polarizability. A model that takes the polarizabilities of both the nanoparticle and the molecule(s) into account is therefore a more appropriate starting point for discussing nanoplasmonic biosensing. By approximating the nanoparticle and the molecule as dipoles, the so-called Coupled Dipole Approximation (CDA) can be used to find the new, modified, polarizability through coupling effects from their induced fields [72, 73]. In the case of one particle and a single molecule, the two dipole moments can be written as:

$$\vec{P}_{NP} = \alpha_{NP}\left(\vec{E}_0 + \vec{\mathbf{A}}\vec{P}_{molecule}\right), \tag{4.2a}$$

$$\vec{P}_{molecule} = \alpha_{molecule}\left(\vec{E}_0 + \vec{\mathbf{A}}\vec{P}_{NP}\right), \tag{4.2b}$$

where α_{NP} and $\alpha_{molecule}$ are the polarizabilities of the nanoparticle and the molecule, respectively, and $\vec{E}_0$ is the incident field. The interaction between the individual dipoles is described using the matrix $\vec{\mathbf{A}}$, so that $\vec{\mathbf{A}}\vec{P}_{NP}$ corresponds to the field induced by the nanoparticle at the location of the molecule and vice versa for $\vec{\mathbf{A}}\vec{P}_{molecule}$. Further, the dipole polarizabilities are described as:

$$\alpha_{NP} = 4\pi a_{NP}^3 \frac{\omega_0}{\omega_0^2 - \omega^2 - i\omega\gamma_0}, \tag{4.3a}$$

$$\alpha_{molecule} = 4\pi a_{NP}^3 \frac{n^2 - n_d^2}{n^2 + 2n_d^2}, \tag{4.3b}$$

where a_{NP} and $a_{molecule}$ are the radii of the nanoparticle and the molecule, respectively, ω_0 is the resonance frequency of the nanoparticle and γ_0 is a damping factor. Further, n and n_d are the refractive indices of the small molecule and the surrounding

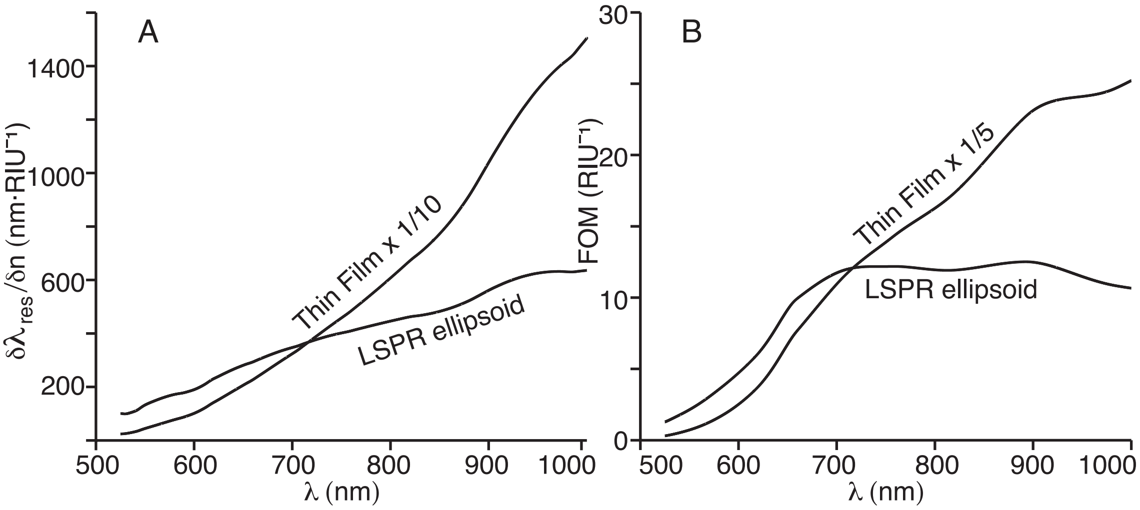

Figure 4.3: Theroretical comparison of LSPR in Au ellipsoidal nanoparticles and thin film SPRs. (A) Bulk refractive index sensitivity and (B) the figure of merit of propagating SPR and Localized SPR in ellipsoidal particles in water ambient medium, using equation (4.5) and (4.7) with dielectric function of gold from [63].

medium respectively. Inserting $\vec{P}_{molecule}$ into equation (4.2a) and assuming $n > n_d$, we find a red shift of the particle resonance according to:

$$\tilde{\omega}_0^2 = \omega_0^2 \left(1 - \frac{V_{molecule}}{V_{NP}} \frac{n^2 - n_d^2}{n^2 + 2n_d^2} (a_{NP}^3 A)^2 \right) . \tag{4.4}$$

In this model the red shift is determined by three factors: The volume ratio between the molecule and the nanoparticle, determining the stiffness of the particle resonance; a refractive index contrast factor indicating the refractometric footprint of the molecule in the surrounding medium, and a coupling factor, directly related to the local intensity enhancement factor at the molecule's location. The final factor suggest varying LSPR shifts depending on the adsorption position with respect to the induced dipole moment of the nanoparticle. Further, local hot spots with high enhancement factors, for example near sharp edges or small gaps between particles, can be expected to yield large responses.

4.4 Propagating versus Localized Plasmons: Bulk Refractive Index Sensitivity

Propagating plasmons in thin metal films and localized plasmons in nanoparticles clearly have the same physical origin and they are both sensitive to the surrounding refractive index. The obvious question is then if one is superior to the other. The differences in bulk sensing properties between SPR and LSPR sensors can be understood from simplified theoretical models. Homola et al. showed that the SPR bulk sensitivity can be derived from the SPP dispersion relation given by equation (2.4) by differentiating k_{SPP} with respect to n [130]. Miller and Lazarides showed that the sensitivity of LSPR can be derived in a similar manner from the dipole polarizability of an ellipsoidal particle [140]. The resulting expressions are:

$$\frac{\partial \lambda_{res}^{SPP}}{\partial n} = -\frac{2\varepsilon^2}{n^3 \frac{\partial \varepsilon}{\partial \lambda_{res}}}, \tag{4.5a}$$

$$\frac{\partial \lambda_{res}^{LSPR}}{\partial n} = \frac{2\varepsilon}{n \frac{\partial \varepsilon}{\partial \lambda_{res}}}. \tag{4.5b}$$

Equations (4.5a) and (4.5b) indicates that the bulk refractive index sensitivity of plasmons is mainly determined by the wavelength-dependent metal dielectric function and the refractive index of the surrounding media. In particular, the bulk sensitivity expression for LSPR explains why nanostructures of different shapes but with the same composition and resonance wavelength exhibit very similar bulk refractive index sensitivities. The bulk sensitivity is however not the only parameter of importance. Therefore, a Figure-of-Merit has been suggested: $FOM = \frac{\partial \lambda_{res}}{\partial n}/\Gamma$, where Γ is the full width at half maximum of the resonance [141]. The FOM was introduced as it is easier to visualize a small shift in a narrow resonance than in a broad resonance. It can be shown that the widths of the resonances can be written as [142, 143]:

$$\Gamma_{SPP} = \frac{4\varepsilon''}{\left|\frac{\partial \varepsilon'}{\partial \lambda_{res}}\right|}, \tag{4.6a}$$

$$\Gamma_{LSPR} = \frac{2\varepsilon''}{\left|\frac{\partial \varepsilon'}{\partial \lambda_{res}}\right|}. \tag{4.6b}$$

Combining equation (4.5)- (4.6) yields the FOM for the two methodologies:

$$FOM_{SPP} = \left|\frac{\varepsilon'}{2n^3\varepsilon''}\right|, \tag{4.7a}$$

$$FOM_{LSPR} = \left|\frac{\varepsilon'}{n\varepsilon''}\right|. \tag{4.7b}$$

The theoretical FOM and bulk sensitivities are plotted in Figure 5.2 using experimentally obtained dielectric data for gold [63]. Note that the analytical expression for the LSPR case is considering a free particle in a homogeneous medium with no radiative damping. This is commonly not the case, for instance for nanodisks immobilized on a glass substrate. The glass itself effectively decreases the sensitivity by approximately 50 % as about half of the plasmon induced field can be assumed to reside in the glass rather than in the ambient [144]. Additionally, depending on the size of the particle, radiative losses are often significant and may for relatively large nanodisks decrease the FOM with another ∼50%.

4.5 Molecular Sensing: The Role of Field Confinement

Generally in biosensing experiments, molecules will accumulate close to the metal interface. It is therefore not enough to consider only the bulk refractive index sensitivity, as the sensitivity confinement is of crucial importance. It is therefore useful to introduce an effective refractive index, weighted on the induced plasmonic near field. For propagating plasmons in thin films, the electric field decays exponentially from the metal surface into the ambient media. The effective refractive index can then be defined as [145]:

$$n_{effective} = \frac{2}{L}\int_0^\infty n(z)E(z)^2\delta z = \frac{2}{L}\int_0^\infty n(z)e^{-2z/L}\delta z, \tag{4.8}$$

where $L = 1/|k_z|$ is the plasmon field decay length into the ambient medium and $n(z)$ is the refractive index at distance z from the metal surface. The decay length can be approximated, using Maxwell's equations and equation (2.4), as:

$$L_{SPR} = \frac{\lambda}{2\pi}\sqrt{\frac{\varepsilon' + n_d^2}{n_d^4}}, \tag{4.9}$$

where ε' is the real part of the dielectric constant of the metal. Typically, the decay length is of the order of 200-300 nm for gold films in the visible and near infra-red. Now assume that a layer of molecules with thickness d and refractive index n_{layer} is adsorbed on the substrate. This gives rise to a response of the sensor:

$$\Delta\lambda = \Delta n \frac{\partial\lambda_{res}}{\partial n}\left(1 - e^{-2d/L}\right), \tag{4.10}$$

where $\Delta n = n_{layer} - n_d$ is the effective refractive index change and $\frac{\partial\lambda_{res}}{\partial n}$ is the bulk refractive index sensitivity of the sensor. Equation (4.10) can be used to convert plasmon shifts to refractive index change and further to the amount of adsorbed molecules. This is typically done in terms of the adsorbed molecular mass per sensor area unit, which can be estimated from[146]:

$$\Gamma_{ads} = \frac{\Delta n}{\frac{\partial n}{\partial c}} d, \tag{4.11}$$

where $\frac{\partial n}{\partial c}$ is the molecule specific refractive index increment.

Even though the exponential decay model is excellent for thin film SPR measurements, it is not obvious that it can be used also for localized plasmons. For example, Xu et. al theoretically studied the response of gold and silver spheres immobilized on glass substrates, thereby simulating experiments by Okamoto et. al on supported colloidal particles covered with varying thicknesses of nanometric PMMA layers [134, 147]. Using extended Mie-theory for core-shell particles, and including the effects of the surrounding medium, particle-particle and particle-substrate interactions, the influence of the adsorption layers on the plasmon resonance position was investigated for different particle sizes.

Both experiments and theory showed that the plasmon in smaller particles shifted faster with increasing coating thickness, d. The results was interpreted in terms of a particle dependent field decay and it was concluded that the plasmon induced field in the vicinity of the nanoparticle drops as $(a_{NP}/r)^6$, where a_{NP} is the particle radius. This is the expected result for a dipolar plasmon resonance, which dominate the induced field for a sub-wavelength metal particle. Using the dipolar power-law decay, it is then straightforward to define an effective refractive index $n_{effective}$ in the same manner as for the SPR case:

$$n_{effective} = n_{layer} - \frac{n_{layer} - n_d}{(1 + d/a_{NP})^3}. \tag{4.12}$$

Equation (4.12) does not show much resemblance with the thin film case, although the field fall off rapidly from the metal surface. Using the dielectric function of gold and the resonance condition of colloidal nanoparticles, the plasmon wavelength shift can be written as:

$$\Delta\lambda = \frac{2}{\frac{\partial\varepsilon}{\partial\lambda}} \left(n_{layer}^2 \left(1 - \frac{1 - n_d/n_{layer}}{(1 + d/a_{NP})^3} \right)^2 - n_d^2 \right). \tag{4.13}$$

The $(a_{NP}/r)^6$ power law above, as well as the coupled dipole analysis discussed previously, demonstrates that the optical near-field intensity distribution is crucial for understanding LSPR sensing. However, nanostructures positioned in more complicated dielectric environments can exhibit much more complex sensing characteristics. This can be illustrated by the study of Rindzevicius et. al, reporting on the possibility of long-range LSPR sensing by utilizing interference and dipolar interactions [148]. In contrast to the colloid example above, where ∼75% of the saturated shift was expected for a layer thickness equal to the radius of the nanosphere, the studied nanodisk arrays showed an oscillatory behaviour of the LSPR as a function of layer thickness. In particular, there were high-sensitivity regions as far away as 100 and 300 nm from the metal surface, which is far outside the expected near-field decay length.

For non-spherical particles, such as nanodisks, it is however common to use equation (4.8) instead of equation (4.12), with L denoting an empiric length related to the *effective* decay length as the actual decay length will vary depending on the position on the nanoparticle. These effective decay lengths are in the range of tens of nanometers for gold nanoparticles. A useful approximation for gold nanodisks is $L_{LSPR} \approx D/4$, where D is the nanodisk diameter [149].

4.6 Common LSPR Sensing Methodologies

In this section, some common measurement techniques are reviewed. All the different methodologies have their respective advantages and disadvantages, but the measurements are still dependent on the descriptions given in the previous sections of this chapter.

Spectroscopic Measurements

Spectroscopic interrogation of the LSPR is based on measuring either the transmitted, reflected or scattered light as a function of wavelength. It is the most common measurement methodology of LSPR sensing today and can be used for both macroscopic samples and for single particle measurements in microscopes [119, 132, 134–137, 150–152]. The ease with which such measurements can be conducted is illustrated in Figure 4.4A-B. All that is needed is a light source (halogen lamp, labeled 1 in Figure 4.4B) a simple lens system (2,4) and a miniature spectrometer (5) for precise measurements of the LSPR in the nanoparticle layer (3). The simple device is small (about 30x10x15 cm) and performs similar in signal-to-noise (SNR) as the best LSPR sensors previously reported [151], that is, with SNR $\approx 10^3 - 10^4$ for monolayer protein formations, as illustrated in 4.4 C-D.

Generally, the wavelength of maximum scattering or extinction is followed as a function of time during the adsorption process. The peak wavelength can, in turn, be tracked by a number of means, for instance, by fitting suitable functions to the spectra, such as a Lorentzian. It is, however, also possible to fit a high degree polynomial to the spectrum, in order to reconstruct and convert the pixelated spectrum into a continuous function. The peak position is then easily followed by differentiating the function with respect to the wavelength. The perhaps most efficient method is to calculate the so-called centroid of the resonance, that is, to find the center of mass [151]. The centroid methodlogy is used in to form the curve in Figure 4.4D, using the parts of the spectra exemplified by the colored areas in Figure 4.4C. The span of the resonance used to calculate the centroid position is constant throughout the measurement, but the wavelength range changes as the centroid position changes. Depending on the asymmetry of the resonance, the centroid position differs slightly from the maximum position in the spectra, but generally the shifts are very similar.

Intensity Based Measurements

A simpler methodology is to measure the extinction or scattering of a single wavelength [135, 136, 151, 153–156]. In such a setup less expensive optical components are needed, as only a (semi-)monochromatic light source and a photo detector are required, while the other optical components would be identical to the spectroscopically based setups. Basically, the idea can already be spotted in Figure 4.4C, where the reflected intensity, for a single wavelength, changes during the adsorption of molecules. To elucidate the difference, Figure 4.5A show the reflection spectrum taken at 90 min subtracted by the spectrum at the beginning of the experiment. Clearly, the largest reflection difference occurs slightly off-resonance, here at 629 nm ($\lambda_{res} = 612$ nm). The asymmetry of the difference spectrum is due to the asymmetry of the spectra shown in Figure 4.4C. A more symmetric resonance would lead to more symmetric difference spectra, with a deeper negative dip to the blue of the resonance wavelength. The symmetry of the resonance can be used by illuminating the nanoparticles with two different wavelengths and tracking the intensity fluctuations in these [151].

Apart from high sensitivity, that is, large reflection intensity difference upon changes of the local refractive index, high *contrast* would be beneficial in sensing schemes. The contrast can, for instance, be evaluated by a Figure of Merit (FOM*)

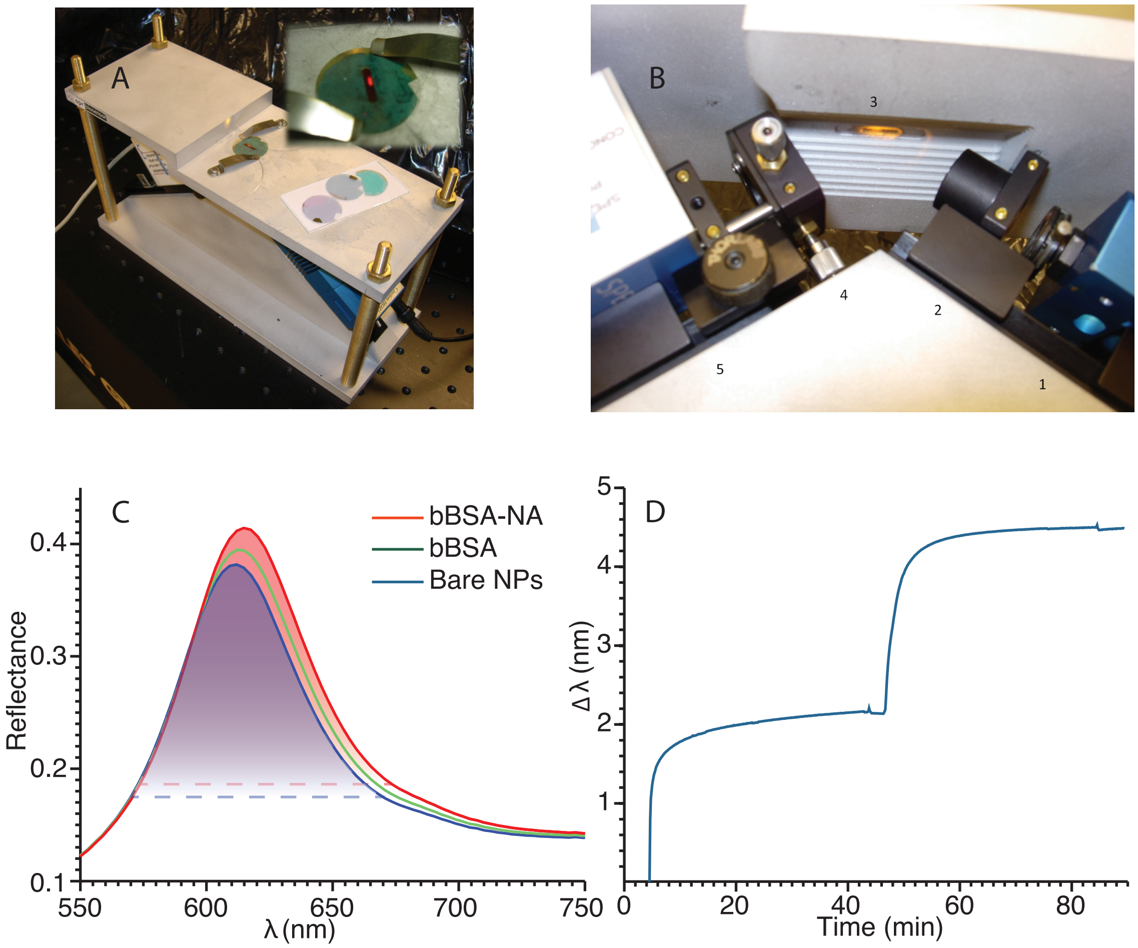

Figure 4.4: A simple prototype macro scale LSPR biosensor. (A-C) By illuminating the substrates at the Brewster angle using p-polarized light, mainly reflected light from the nanoparticle layer will be detected by the spectrometer. (D) The compact prototype performs on the level of state-of-the-art macro scale LSPR biosensors. The adsorption kinetics first show 100 μg/ml biotinylated bovine serum albumin binding to bare gold nanoparticles (80 nm in diameter and 20 nm tall) and the subsequent adsorption of 10 μg/ml Neutravidin.

[157]:

$$FOM* = \frac{\partial I(\lambda)/\partial n}{\overline{I(\lambda)}}, \tag{4.14}$$

where the intensity change $\delta I(\lambda)$ upon refractive index exchange δn is normalized to the mean intensity, $\overline{I(\lambda)}$. In a sense, this formula denote the visibility of the intensity change per refractive index. Naturally, with a reflection coefficient that is zero, for example in water, and then changes slightly as the refractive index is increased (or decreased), the visibility is maximized at ±1. However, as very few photons are likely to be reflected with slight changes of the refractive index, stable and sensitive detectors and light sources are needed to fully utilize the visibility.

However, with a stable light source, single wavelength measurements are fully feasible and perhaps a good alternative if the same structures are repeatedly interrogated. For a cheap device, this interrogation method is perhaps the most practical.

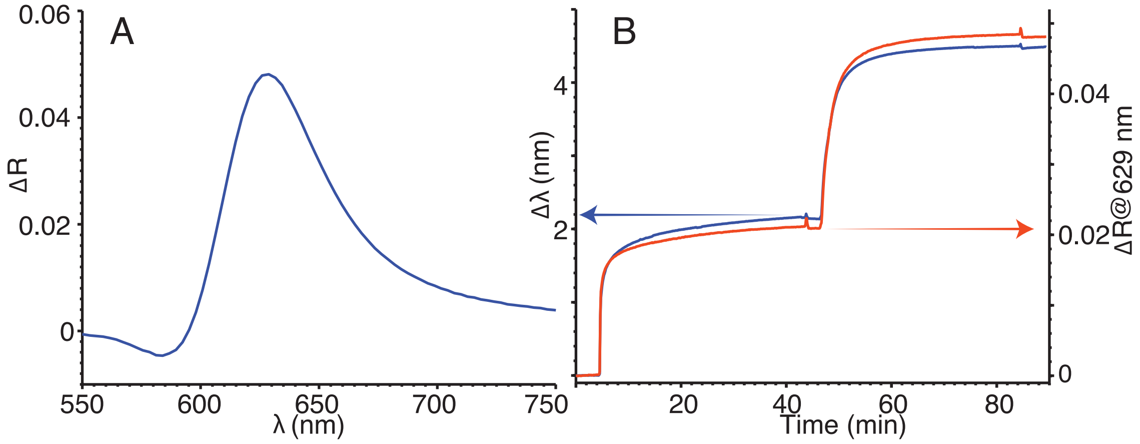

Figure 4.5: Intensity based LSPR biosensing. Based on the spectroscopic data in Figure 4.4, the intensity of the reflected light can be used for sensing purposes, instead of the spectral position of the LSPR. (A) The intensity difference between $t = 90$ min and $t = 0$ min depends on λ. (B) A single wavelength could then be tracked as a function of time to yield similar kinetics as spectrosopic data.

The downside of the simple setup is, however, that the signal is much more sensitive to fluctuations of the light source intensity compared to the spectroscopic interrogation methodology.

Phase Measurements

Although spectroscopy and intensity are by far the two most widely used techniques to measure the plasmonic response to molecular adsorption or other changes of the local dielectric surroundings, a third category have recently been proposed as an alternative measurement methodology. Resonances can be described by their response in frequency and amplitude, but also by their phase. For instance, the phase of a Lorentzian resonance varies 180° as the resonance frequency is traversed from low to high frequencies. Thus, investigating the phase may be as effective as spectroscopic measurements. However, in general, phase detection measurements require more elaborate optical methodologies and/or equipment, as optical phase cannot be detected directly due to the high frequency of visible light. Therefore, it is necessary to compare the phase to a so-called reference signal, generally of the same or very similar frequency.

Polarimetry and ellipsometry involve the phase difference between two orthogonally polarized waves, such as p- and s-polarized light. Thus, one of the polarizations may work as a reference signal, to which the phase of the other may be compared. Generally when linearly polarized light is reflected from or transmitted through a medium, the outgoing beam is elliptically polarized. The ellipticity carries information of the media under investigation and is therefore regularly used to investigate, for instance, the optical properties of thin films. The same information is present in reflected light from nanostructured surfaces [82]. As an example, gold nanorods, illuminated through a prism in a total internal reflection geometry, can be aligned with respect to the plane of incidence, while varying the incident ellipticity of the light, to increase the sensitivity of the reflected intensity to the local refractive index

[158].

In addition to the phase response of resonators and plasmonic nanostructures, a resonant surface with a Fresnel reflection coefficient that traverses zero has an additional phase jump. The latter, additional, phase jump occurs also for non-resonant surfaces, for instance at Brewster angles in dielectric interfaces. For instance, arrays of nanoparticles can be used to achieve zero reflectance for a particular wavelength when placed at the interface between two dielectric materials. Thus, the reflected phase will not only have a signature of the plasmonic resonance of the nanostructures, but also an additional component, increasing the phase shift as the resonance is traversed. With this in mind and taking advantage of the narrow resonances of diffractively coupled nanostructures, Kravets et al investigated the amplitude and phase bulk sensitivity of collective plasmons in arrays of nanodot dimers and monomers in both gaseous and aqueous environment using spectroscopic ellipsometry[159]. Due to the effective coupling between the individual nanostructures, resonances as narrow as 6 nm were found, with bulk refractive index sensitivities of the phase difference between p- and s-polarized light, Δ, of the order of 10^5 °/RIU. The detection limit of the typical biotin-streptavidin interaction was, however, quite moderate around 1-4 molecules per nanodot with a monolayer shift of the resonance of around 25° [160].

Similar zero reflection properties can be found in less ordered arrays of gold nanodisks, for example, prepared by Hole Mask Colloidal Lithography (HCL), as predicted previously in Figure 3.6. As seen in Figure 4.6, Δ varies very rapidly across the zero reflection condition of s-polarized light. A small difference at the zero reflection wavelength can therefore yield a significant phase response. Figure 4.7 show that upon molecular adsorption processes Δ at 637 nm shifts about 25°. The phase shift compared to the width of the resonance is about one order of magnitude larger for Δ than the spectroscopic shift of λ_{res}. However, if studying the signal-to-noise ratio (SNR) of the adsorption process, where the change of a particular parameter upon molecular adsorption is normalized to the fluctuations without any antigens present, the spectroscopic measurements of the s-polarized reflections are still better. The experimental setup, is detailed in Figure 5.3.

Another interrogation method of Δ is, for instance, using a single wavelength light source and creating spatially varying polarization states, see reference [161] and Figure 5.4. Fringes will appear due to the interference between the reflections of the two polarizations. Even though such an implementation is quite different from the direct measurement of Δ, the phase shifts upon molecular adsorption were similar, almost 20° for a protein monolayer formation, with similar kinetics, as seen in Figure 4.7C-D.

Another pathway is to couple nanostructures with high quality resonators, such as Fabry Perot etalons, and study the coupling efficiencies, which will largely depend on the phase properties of the two (plasmonic- and non-plasmonic-) resonators. In principle, one may view this as placing a nanostructured surface as one of the mirrors in a Fabry-Perot interferometer [148, 162–165]. Although most of these studies utilize arrays of nanostructures, it is also possible to utilize a single nanoparticle as one end of the cavity [166].

Several articles have argued favorably for phase-based detection schemes as compared to amplitude or intensity measurements and even to spectroscopic interrogation methodologies [159, 160, 167]. Although there are clear benefits in some inter-

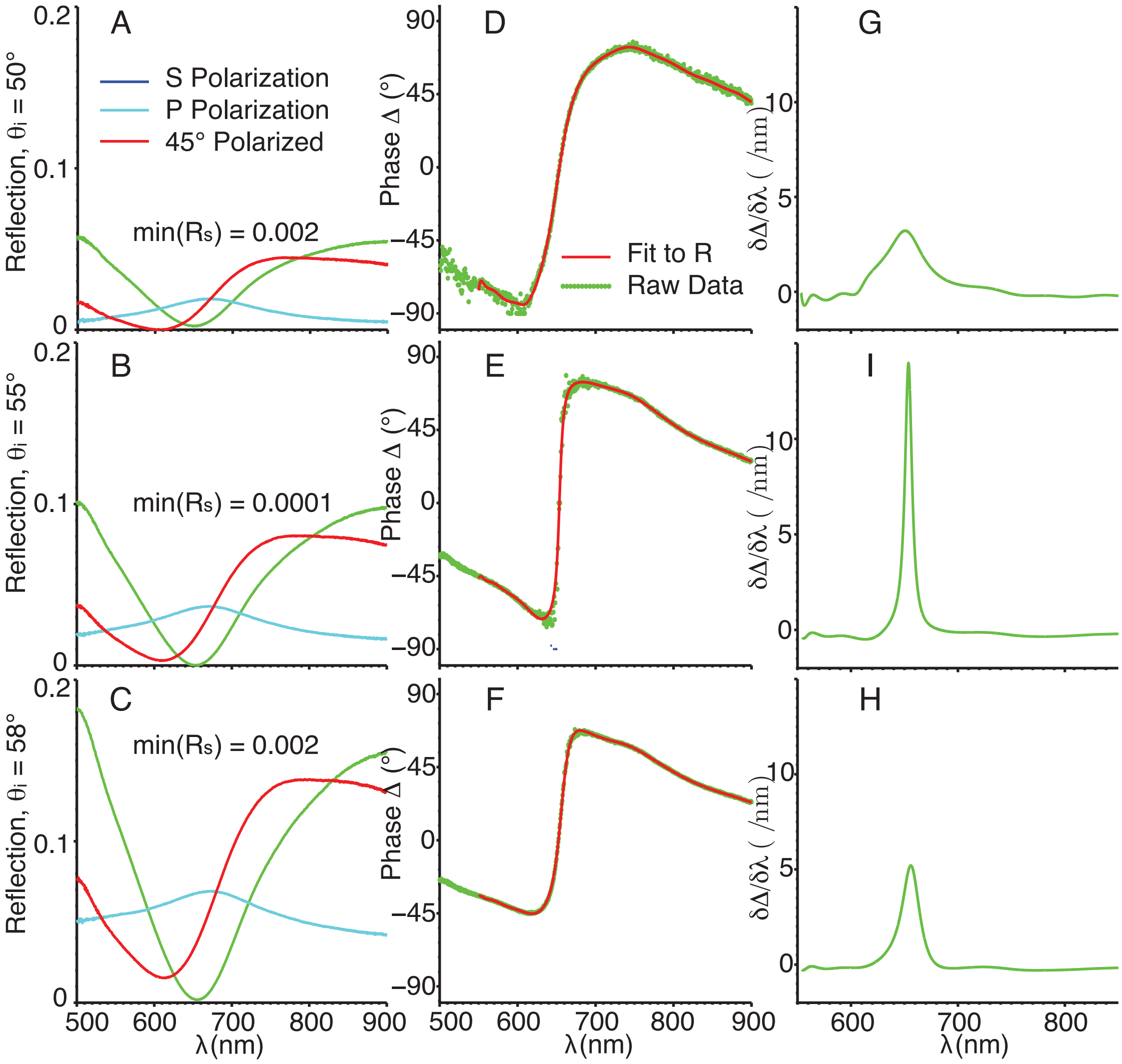

Figure 4.6: Reflected phase measurements from an array of gold nanodisks in a glass/water interface. As the s-polarized reflections approaches zero, the phase difference, Δ, varies faster and faster across the zero reflection wavelength. The phase measurements presented here are based on the three reflection spectra in panels (A-C), from which $\sin \Delta$ is solved, see Chapter 5.3 and Figure 5.3. Δ is therefore only defined between ±90°. The lowest reflection also yield the fastest phase response.

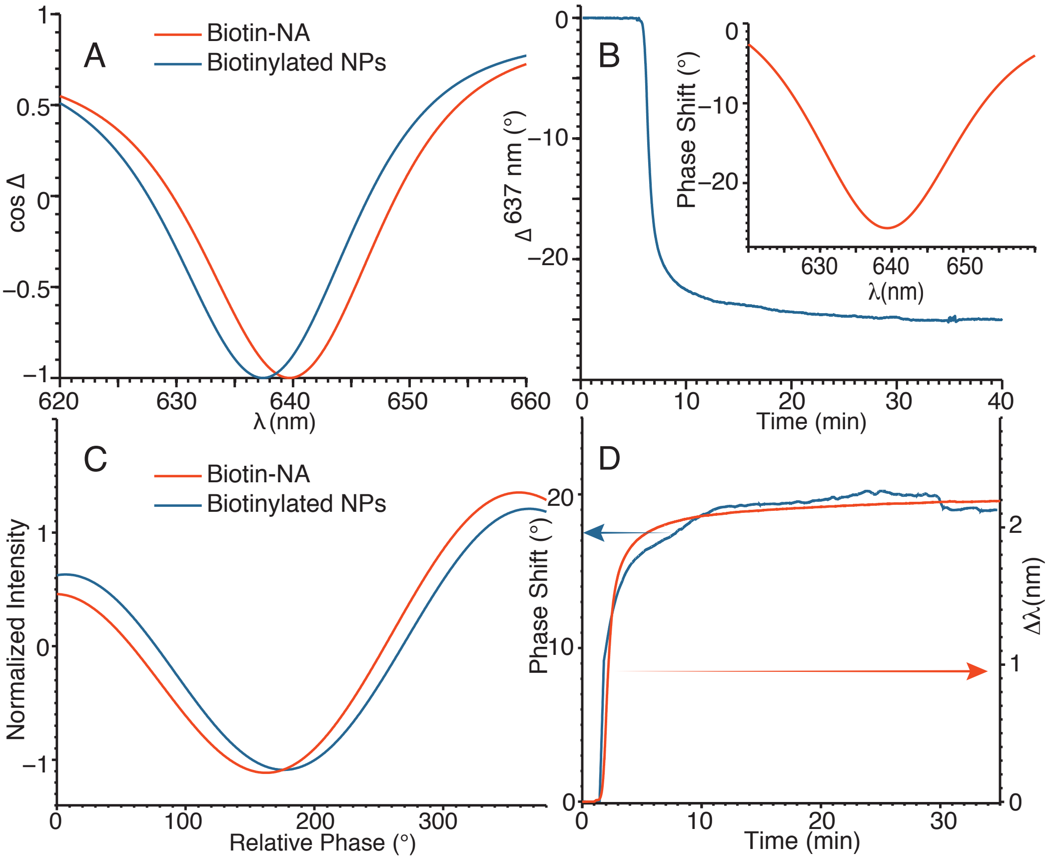

Figure 4.7: Phase-based biosensing. Spectroscopic based (A-B) and single wavelength based biosensing (C-D). A metasurface can be tuned into a zero reflection condition for a certain polarization and wavelength. By measuring the phase difference between p- and s-polarized light, Δ, enhanced phase sensitivity to the surrounding medium can accomplished. (A) The narrow line shape of Δ near the zero reflection wavelength, yields a large spectroscopic visibility of the molecular adsorption. (B) The phase for a single wavelength can be tracked during the adsorption process, keeping in mind that the largest sensitivity is limited to wavelengths in close proximity to the zero reflection condition. (C) In a single wavelength interferometric setup, similar visibility of the adsorption can be obtained in the tracking of fringes, with (D) kinetics in line with typical extinction measurements. (A-B) stems from spectroscopic measurements, detailed in Figure 5.3, while (C-D) are single wavelength measurements using a setup described by Figure 5.4.

ferometric and ellipsometric techniques, partly due to the in-line reference, but also due to the impressive sensitivities reported, there has not, to my knowledge, been any reports of a phase or interferometric methodology showing lower experimental detection limits of biologically or chemically relevant molecules. One reason behind this discrepancy could be the stability of the experimental setups used. More sensitive interrogation methods also put larger requirements on the stability of optical components, as well as on thermal and vibrational stabilization of the setup and the media under interrogation. In either case, further investigations will certainly answer these questions and help develop the sensing field as such.

Directionality Based Measurements

Antennas are generally used for sending and receiving information. In order to reduce the interference from unwanted sources, *directional* antennas are commonly used. The typical antenna example is the old Yagi-Uda TV-antennas that was used before digital-TV and cable-TV completely overpowered the market. These antennas had to be positioned and directed in a certain way to achieve a good TV-signal. The TV-antennas naturally dealt with much longer wavelengths compared to visible light, but the same interference perspective can be used for plasmonic nanoantennas [168].

In the simplest case, two slightly detuned antennas, positioned a certain distance from each other, can show remarkable directionality [87, 169]. As first shown by Evlyukhin *et al.*, the directionality changes with the local dielectric surroundings of the antennas.[169] The change in detuning, and perhaps in the respective intensity of the two antennas, is the main parameter for the different directionality.

The feasibility of this approach has been shown both for the application of materials science, studying the hydrogen absorption in Pd nanoparticles [170]. The directionality measurements generally uses a single probing wavelength with which the directionality into certain regions are probed. Due to the simultaneous measurement technique, the system is self-referenced and thus less sensitive to intensity fluctuations of the light source, compared to direct intensity measurements.

Optical Activity

In recent years, there has been significant interest in fabricating chiral plasmonic nanostructures that could enhance the chiral signature of biomolecules. The idea is based on so-called super-chiral fields in the vicinity of the nanostructures. As chiral nanostructures themselves will enhance the super-chiral fields preferentially for either left- or right handed light, chiral molecules will be exposed to different fields at different structures, possibly leading to enhanced absorption of the preferred handedness [171, 172]. Therefore, more or less identical structures, but with different handedness, must be fabricated for an evaluation of the molecules in question.

Another pathway is to use non-chiral nanostructures for the same means, however, without the necessity of fabricating two different structures [173–179]. Although non-chiral, it seems that both electrical- and magnetic dipoles are necessary for best performance. Both the chirality of the molecules themselves and the geometrical formation of the ligands as they adsorb near nanoparticle surfaces can be detected [175].

The niche of circular dichroism enhancement make nanoplasmonic sensing unique. There are few other techniques that can be used to enhance the optical activity of molecules on the nanoscale. Therefore, this field of research will be very interesting to follow in the coming years.

Photothermal Measurements

The final note on LSPR-based refractometric sensing techniques one should mention the photo-thermal imaging technique. It is based on the intensity change of a detection beam due to a time-dependent thermal lens effect. Using this technique it is possible to spot small metal nanoparticles or even small absorbing molecules [120, 180–182].

Zijlstra *et al.* showed that single binding events to the tips of metal nanorods can be measured using this technique [120]. A detection beam at 693 nm was studied during the adsorption of different proteins to biotinylated nanorods using a heating beam at 785 nm. As the heating beam was modulated, a lock-in amplifier was connected to the detector, measuring the 693 nm light. Step-wise jumps in the photothermal signal was then interpreted as the adsorption of individual proteins.

4.7 Molecular Sensing: Adsorption Kinetics

While the former parts of this Chapter is focused on fundamental aspects and measurement techniques of plasmonic refractometric sensing, mainly for biosensing applications, this section will briefly describe *how* molecules end up in close vicinity of the plasmonic fields. Thus, there are two main components in this discussion: Surface chemistry and mass transport. The surface chemistry should capture the target molecules and repel other molecules at the sensor surface and perhaps also direct the adsorption by keeping other, insensitive regions inert. The mass transport supplies molecules to the surface, where they may form adsorbed complexes.

The actual rate with which an adsorption reaction occurs is always determined by both the chemistry and the mass transport to the surface, as illustrated in Figure 4.8A. In some cases the reaction rate is completely dominated by one of the two components, it can either be reaction or mass transport limited. The limiting step can be evaluated using the Damköhler number, Da, which is the ratio between the adsorption rate and the mass transport rate.

Molecular Adsorption Reactions

The receptors need to capture the correct antigens. The receptor/antigen interaction is generally described by their affinity or $K_D = k_{off}/k_{on}$. A simple time dependent interaction at the sensor surface can be written as:

$$\frac{\delta\Gamma}{\delta t} = k_{on}C\left(\Gamma_{max} - \Gamma\right) - k_{off}\Gamma, \tag{4.15}$$

where C is the analyte concentration, t is time, Γ is the surface concentration of adsorbed molecules, Γ_{max} is the receptor surface concentration and k_{on} and k_{off} are the adsorption and desorption rates of the receptor-analyte interaction. Note that C is the target concentration in the immediate surrounding of the sensor surface.

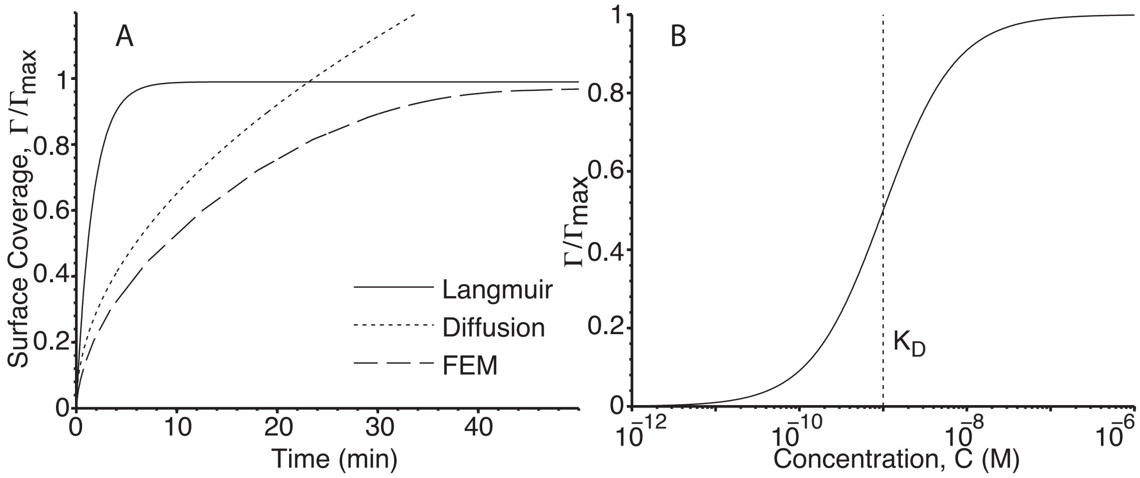

Figure 4.8: Adsorption kinetics and limitations. (A) For an infinitely large planar sensor, the surface coverage is not solely determined not by neither the Langmuir isotherm nor the diffusion rate to the surface, but by the interaction between these, as shown by a finite elements method calculation, for the case of $C = 100$ nM, $K_D = 1$ nM, $\Gamma_{max} = 4$ pmol cm^{-2}. (B) The reaction is limited by the affinity of the two molecules. Inspired by [183].

Therefore, an adsorption event decreases the local concentration of freely diffusing molecules:

$$\frac{\delta \Gamma}{\delta t} = -D \frac{\delta C}{\delta n_{surface}}. \tag{4.16}$$

Here D is the analyte diffusivity and $n_{surface}$ is the sensor surface normal. It is thereby possible to couple the adsorption with the mass transport, for instance, using the diffusion of free molecules, governed by Fick's law:

$$\frac{\delta C}{\delta t} = D \nabla^2 C. \tag{4.17}$$

Therefore, depending on the specific adsorption rate versus the diffusivity of the target molecules, the concentration of antigens might decrease around the surface sensor. The region with lower concentration of target molecules is generally termed the depletion region. Thus, again, as illustrated in Figure 4.8A, one generally need to take all equations (4.15)-(4.17) into account when trying to understand the adsorption process. Naturally, the depletion region can be counteracted, for instance, by using a continuous flow of molecules over the sensor surface, although for an individual nanoscale sensor, the physical size versus flow velocity should indeed be taken into account [117].

Even with much faster mass transport than binding kinetics, the equilibrium Γ is determined by $\Gamma_{eq} = \frac{\Gamma_{max}}{K_D/C+1}$ and thus limits the sensor probing a specific interaction process. As noted in the previous section, the signal-to-noise of a typical LSPR biosensor response to a monolayer protein formation is about $10^3 - 10^4$. Since the equilibrium surface coverage of the sensor will be limited by the equilibrium formula, a concentration two orders of magnitude lower than K_D yields about 1% receptors bound to an analyte, as seen in Figure 4.8B. If there are about 200 receptors (or possible adsorption sites) on a single nanoparticle, it is therefore very challenging to have detection limits below pM concentrations, given a $K_D \approx 1$nM.

Surface Chemistry

Normally, nanoplasmonic sensors are materially heterogenic, that is, the surfaces contain several different materials. The heterogeneity can be a nuisance, but it can also be taken advantage of, as different surface chemistry thus can be applied to the different materials [184–186]. By forcing the antigens to adsorb in specific locations, for example in a dimer hot-spot, the signal per molecule will be significantly larger [186].

The ideal surface chemistry only captures antigens near the nanoparticles, repels all other molecules, and prevents the antigen to end up anywhere else. A significant part of surface chemistry is the formation of self-assembled monolayers (SAMs) [187]. A typical SAM consists of three parts: The head, the tail and the functional group. The head is the part that fastens the SAM to the specific surface on which it is formed, for instance, silanes are used for silicon and thiols for gold surfaces. The tail stabilizes the overall structure of the monolayer, while the functional group is exposed to the surrounding volume and therefor should add a specific function to the surface. Depending on the geometry and location of the SAM, the function could be either to repel or to capture specific molecules. Often, the functional groups can be hydroxy, in order to avoid adsorption, or a functional group that can be activated in order to attach the capturing agents.

To passivate surfaces, the perhaps most common methodology is based on thick and dense poly-ethyleneglycol (PEG) brushes [188], even though this might interfere with the typical extension of the plasmonic fields. If too thick, a receptor on top of the brush would only yield a very small signal due to the field confinement. Serum or bovine serum albumin (BSA) is also commonly used to reduce non-specific binding.

Another example of a functional group is carboxylic acid, that can form bonds with amines of, for example, antibodies [189]. It is also common to have biotin as a functional group, as the biotin-avidin have extremely high affinity, which can be used for functionalization purposes or for proof-of-principle studies. The biotin-streptavidin affinity can be as large as $K_D \approx 10^{-14}$ M in solution, although lower affinities have been reported from surface based measurements [138, 190, 191]. This can be compared to regular antigen-antibody interactions that have $K_D \sim 10^{-9}$ M [192–194]. While biotin is a small molecule, with a molecular weight around 244 kDa, streptavidin is a larger protein, around 50 kDa with dimensions of about 5.4 x 8.4 x 4.6 nm^3 [195]. The high affinity is due to several factors, including the formation of multiple hydrogen bonds, see Figure 4.9E, van der Waals interactions between the two complexes and the order of surface polypeptide loops, effectively enclosing the biotin within the protein [196].

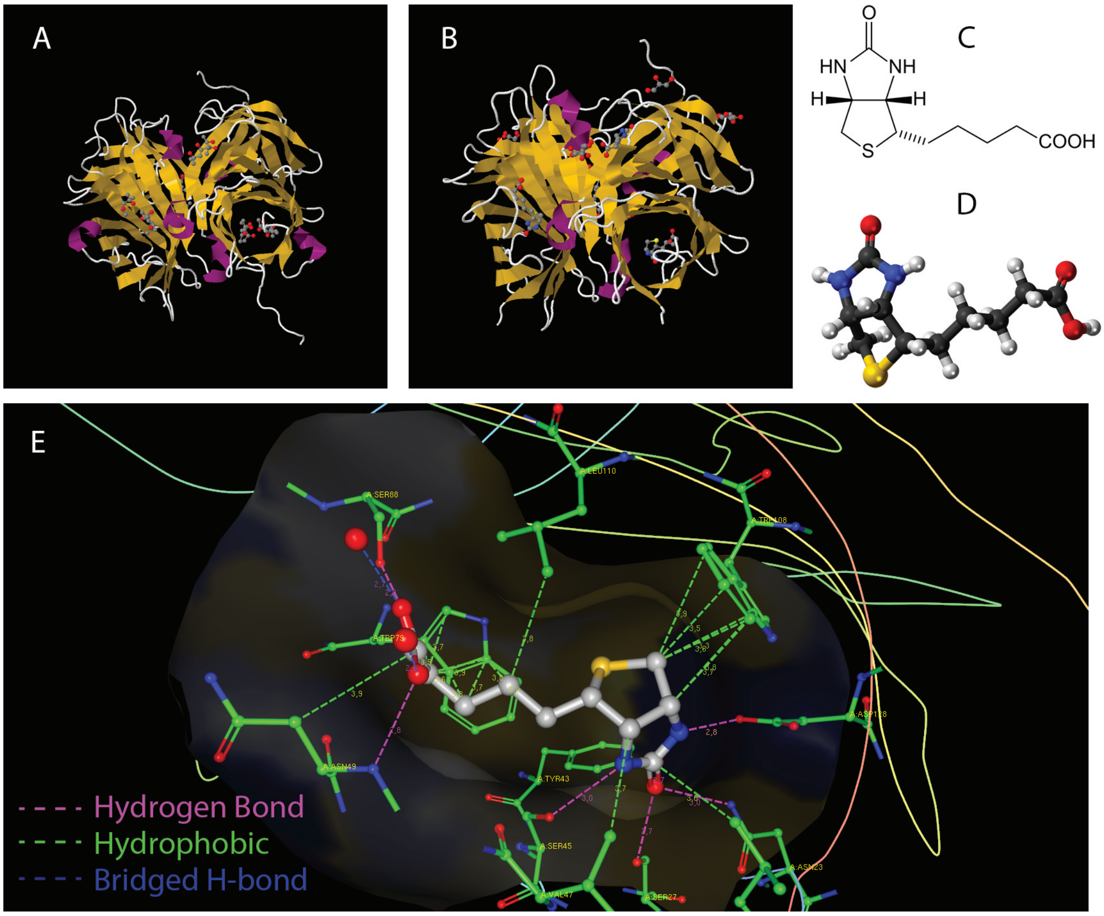

Figure 4.9: Biotin and Streptavidin. Biological assemblies of (A) wild-type core Streptavidin and (B) wild-type core Streptavidin-biotin complex. (C-D) The chemical structure of biotin. (E) Schematic showing the ligand binding of biotin. Figures (A), (B) and (E) originate from the Research for Collaborative Structural Bioinformatics Protein Data Bank (RCSB PDB) [195, 197–199].

Chapter 5

Methods and Sample Characterization

5.1 Optical spectroscopy of Thin Film Plasmons

Figure 5.1 A-D illustrate the most common excitation and detection geometries of surface plasmons in thin metal films. The most commonly used method of excitation is the Kretschmann configuration, shown in Figure (5.1)A and B[44]. Transverse magnetic light incident via a high refractive index prism couples to the metal film using an incidence angle above the critical angle. The in-plane propagation constant of the light at the prism/thin film interface, k_{inc}, is thus dependent on the incident angle, θ_{inc}, which using equation (2.4) yields the following condition for SPP excitation:

$$k_{inc}(\omega) = \frac{\omega}{c} n_{prism} \sin\theta_{inc} = \frac{\omega}{c}\sqrt{\frac{\varepsilon_m(\omega)\varepsilon_d}{\varepsilon_m(\omega)+\varepsilon_d}} = k_{spp}. \tag{5.1}$$

Here, ω is the frequency and c the speed of light, respectively, and n_{prism} is the refractive index of the prism. Figure 5.1A illustrates a technique where the wavelength of the incident light is kept constant, while the illumination takes place from multiple incident angles. This yields a range of propagation constants, k, along the metal film. The reflected light is diverging if the incident light is focused on the film and a minimum is found at the angle where the energy and momentum coupling conditions are met simultaneously.

As seen in Figure 5.1B, white light incident via a prism toward the thin metal film results in a spectral dip at the wavelength that couples most effectively to the SPP. The minimum wavelength, λ_{SPR}, depends on the (fixed) incident angle and the refractive index of the ambient. Tracking λ_{SPR} is a direct measure of the ambient refractive index change. The Kretschmann configuration with spectral interrogation was used throughout this work.

The most common alternative to prism coupling in the Kretschmann geometry is to use so-called grating coupling. Depositing the metal film on a diffraction grating opens the possibility for incident photons to gain or lose virtual momentum (crystal momentum) in units governed by the grating constant a. This leads to the coupling condition:

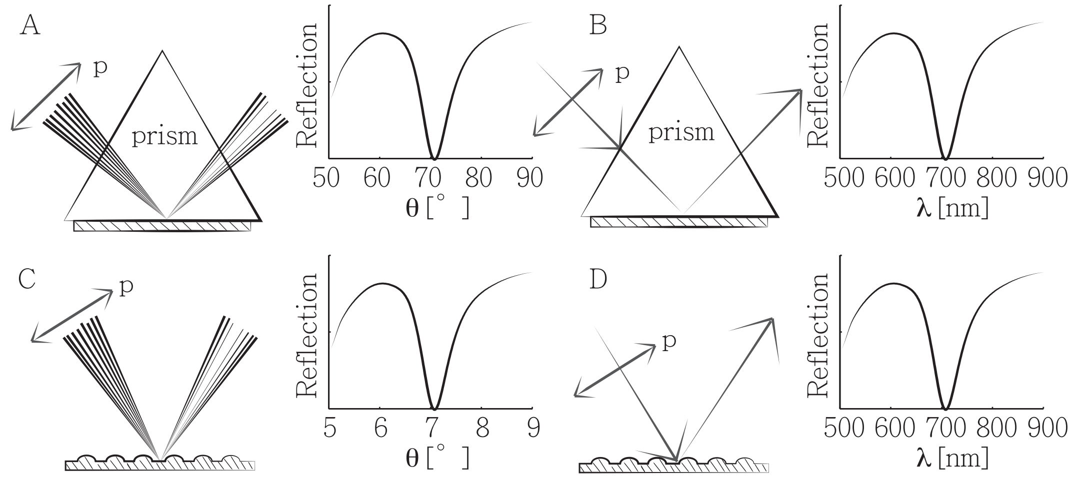

Figure 5.1: Detection methods of surface plasmon resonances in thin films. (A) and (B) are examples of grating coupling excitation of the SPP with angular and wavelength detection, respectively. (C) and (D) illustrates angular and wavelength detection using Kretschmann geometry, respectively.

$$k_{diffracted}(\omega) = k_d + m\frac{2\pi}{a} = k_{spp}, (m = \pm 0, 1, 2, 3...), \tag{5.2}$$

where $k_{diffracted}$ denotes the in-plane propagation constant of the diffracted light in the ambient and m the diffraction order. The additional second term for the diffracted momentum make it possible to excite the plasmon from the ambient side. Grating coupling to the surface plasmon is illustrated in Figure 5.1C and D. Similarly to the Kretschmann configuration above, both spectroscopic and angular detection techniques can be used for probing refractive index changes[200–202]. Interestingly, the grating based SPR sensors show smaller bulk refractive index sensitivity compared to the Kretschmann geometry, but they exhibit similar detection limits [203]. Additionally, by proper design of the grating coupled SPR the resonance can be made sufficiently narrow to allow low cost light sources such as Light Emitting Diodes (LEDs), thus making the grating coupled SPR a low cost alternative to conventional SPR prism sensors[202].

Naturally, monitoring the intensity at a fixed wavelength and incident angle is possible in both grating- and prism based SPR sensors, although this implementation suffers from a smaller dynamic range (Δn_d) as the intensity fluctuations can only be monitored within the width of the resonance. By exchanging the detector to a camera or a CCD detector, this method can be used for detection of multiple analytes simultaneously, using imaging SPR[204–206]. To overcome the low dynamic range, it is also possible to take images with varying incident angles or wavelength, creating a stack of images from which the resonance position can be determined [207, 208]. The latter methodology has some disadvantages though, as imaging from varying angles may create different image distortions.

5.2 Optical spectroscopy of Localized Plasmon Resonances

One of the most attractive properties of nanoplasmonics is the simplicity and variety of optical characterization methods that can be used for a given sample. As mentioned above, the excitation conditions for LSPRs are much more relaxed than for propagating plasmons. Figure 5.2 illustrates the most common optical setups for micro- and macroscopic LSPR sensing. Dark field spectroscopy is a popular technique for measuring the response of single nanoparticles and is illustrated in Figure 5.2A [118, 209–211]. The light is typically incident at high angles and the scattered light is collected using low numerical aperture optics that does not pick up the directly transmitted light. Using dark-field imaging it is also possible to study a large number of single particles simultaneously, thereby improving measurement statistics and potentially enabling multiplexed measurements of several analytes [118, 212]. Dark field measurements of many hundreds of individual nanoparticles can be accomplished using a CCD detector and liquid crystal tunable filter, which can be used to alter the wavelength of illumination or detection[118]. By imaging the nanoparticle array at each wavelength, an image stack is created from which individual scattering spectra of all nanoparticles in the array can be constructed.

Although dark field measurements, or scattering measurements in general, are usually advantageous at low particle densities, the highest signal-to-noise ratios (SNRs) for dense samples has been obtained using extinction measurements[151, 152]. Figure 5.2B illustrates such a measurement in transmission mode, which is related to the extinction cross section of the nanostructures:

$$\sigma_{ext}(\omega) = \frac{1-T}{N}, \tag{5.3}$$

where T is the transmittance trough the sample and N the number of nanoparticles illuminated. It is, however, also common to connect extinction, E, and transmission through Beer-Lambert's Law: $E = -\log T$. The extinction comprises both light scattered in other directions and absorbed in the sample and is therefore a measure of the light that is not detected.

It can also be advantageous to record specular reflection, since a dense layer of nanostructures behave similarly to a homogeneous metamaterial surface, as discussed in Chapter 3. In the case of a low interparticle coupling and low reflectance from the substrate supporting the particle layer, the specular reflectance spectrum can show characteristics similar to a single particle scattering spectrum.

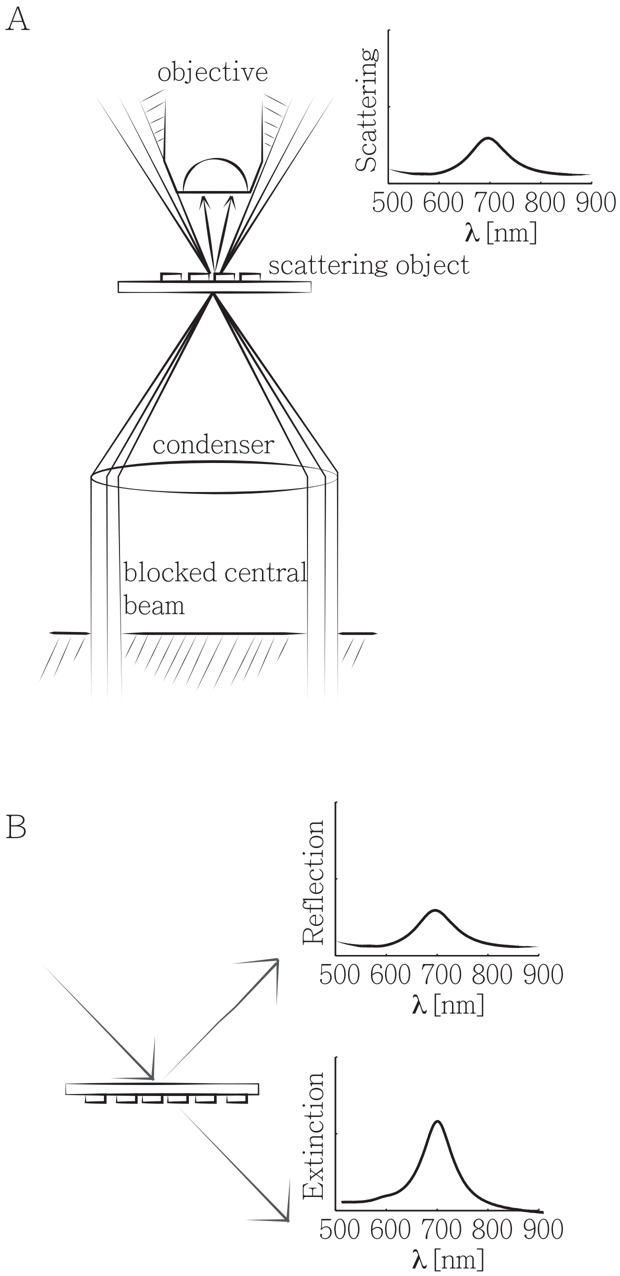

Figure 5.2: Illustration of LSPR detection setups. (A) Dark field spectroscopy in an optical microscope. (B) Macroscopic measurements of a layer of supported nanoparticles using extinction and specular reflection.

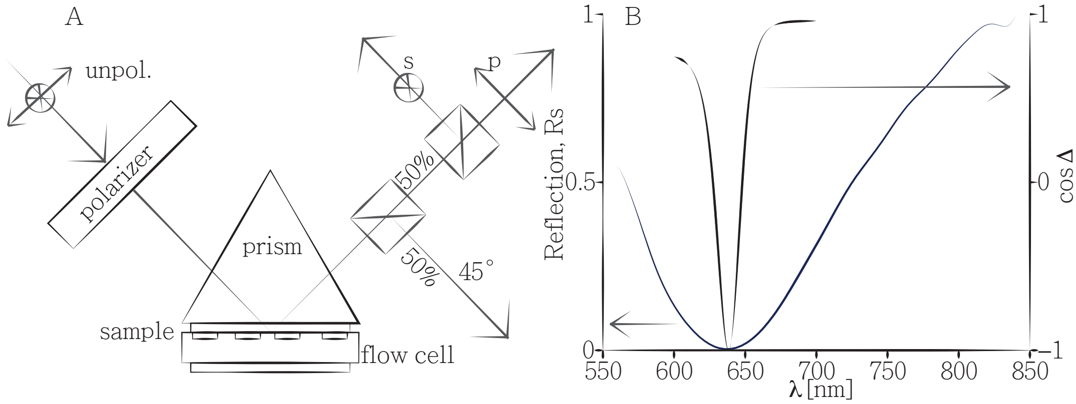

Figure 5.3: Spectroscopic measurement of the sharp phase response near the zero reflection wavelength. By measuring reflection spectra of p-, s- and 45°-polarized light (A), the phase difference between p- and s-polarized reflections can be measured (B). As the s-polarized reflection is zero, the phase component shows a rapid response, varying about one order of magnitude sharper than the intensity component.

5.3 Phase Measurements

The phase between p- and s-polarized light, Δ, can be measured spectroscopically, for instance, using different polarizer angles. As an example, a polarizer set to 45°, yields an, in this case reflected, intensity:

$$I_{45^\circ}(\lambda) = \frac{|r_p(\lambda)|^2 + |r_s(\lambda)|^2 + 2|r_p(\lambda)||r_s(\lambda)|\cos\Delta(\lambda)}{2}. \tag{5.4}$$

Here, $r_p(\lambda)$ and $r_s(\lambda)$ are the Fresnel reflection coefficients from the sample, for p- and s-polarization, respectively.

An optical setup used to measure Δ can be seen in Figure 5.3. Collimated white light, linearly polarized at 45°, illuminate the sample through a right angle glass prism. The reflected light is divided into three parts: One mixed channel, corresponding to $I_{45^\circ}(\lambda)$ in equation (5.4), and two channels measuring the purely p- and s-polarized light, respectively. The phase can then be determined by inversion of equation (5.4). As seen in Figure 5.3B, as one of the unmixed channels show zero reflection, the phase ($\cos\Delta(\lambda)$) varies much faster across the resonance position than the reflected intensity. Illumination using circularly polarized light, by the introduction of a quarter wave plate, results in $\cos\Delta(\lambda) \rightarrow \sin\Delta(\lambda)$. This type of measurement methodology was used to retrieve the spectra in Figure 4.6.

A more straightforward method of measuring the phase could be to use a single wavelength, tuned into the zero reflection wavelength, as illustrated in Figure 5.4 [161, 213, 214]. Here, a laser diode is collimated and linearly polarized before passing through a so-called depolarizer, which is a double birefringent wedge prism (DBWP). The DBWP is made from two birefringent wedge prisms that are mounted together with their respective fast axis misaligned by 45°. Because of the wedge-like structure of the prisms, the retardation of a specific wavelength of light depend on the beam position on the depolarizer. If the incoming beam is large enough, the transmitted light will have spatially varying polarization states along one direction, as explained in more detail below. After the reflection from the nanoparticle layer a linear polarizer, or analyzer, generate a fringe pattern due to the interference be-

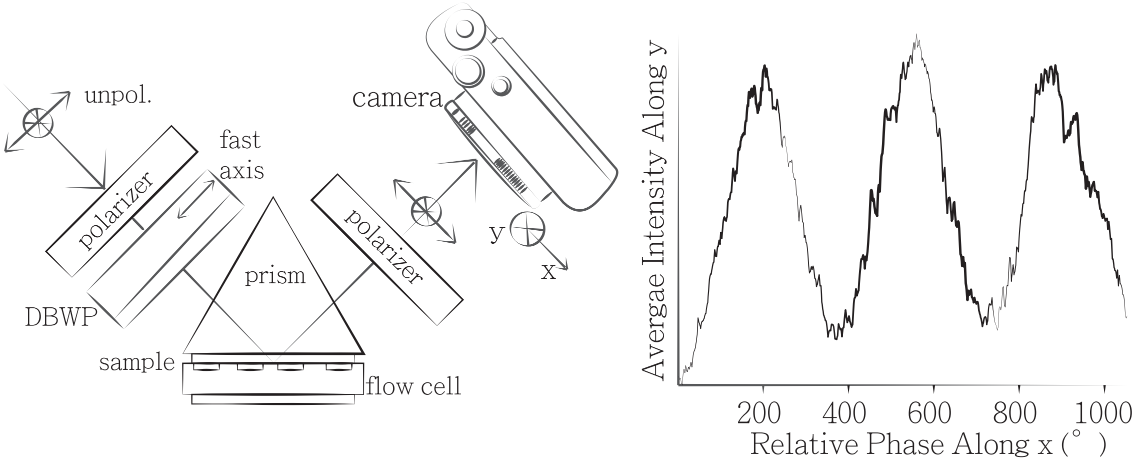

Figure 5.4: Single wavelength phase detection scheme. A laser diode emission is collimated and linearly polarized before entering a depolarizer, which creates spatially varying polarization states, and illuminating a gold nanodisk array through a glass prism. The resulting reflection is analyzed using a polarizer, creating interference fringes from the interference between the p- and s-polarized reflection components. The fringes were detected using a CCD, where the intensity was averaged along one axis to form sinusoidal patterns.

tween p- and s-polarized reflection components. The analyzer has to be tuned to achieve a proper ratio of s-and p-polarized reflected light, as these may differ significantly in intensity. The fringes can then be collected by a CCD camera and, as the pattern is generated along x, the intensity can be averaged along the opposite axis, y, of the image, to create sinusoidal intensity variations, which are tracked during the experiments.

The key optical element in these measurements is the DBWP. Figure 5.5 show an illustration of the polarization states transmitted by the DBWP calculated through Jones matrices[161]. By alternating the polarizer positioned behind the DBWP and studying the fringe patterns caught by the camera, the pattern for a perpendicular polarizer angles are indeed complementary. Thus, the polarization states varies as (retardation from -$\lambda/2$ to $\lambda/2$): Vertical, elliptical, right circular, elliptical, horizontal, elliptical, left circular, elliptical and then back to vertical.

5.4 Thermal Measurements

Temperature relates to vibrations, or kinetic energy, and as the charged particles, like ions, protons and electrons, interact they accelerate or oscillate, leading to electromagnetic radiation. All materials with a temperature above 0 K emit radiation, due to the movements and collisions of charged particles. For a perfect black body, the emitted radiation follows Planck's law.

$$B(T) = \frac{2h\nu}{c^2}\frac{1}{e^{\frac{h\nu}{k_B T}} - 1}, \tag{5.5}$$

where h is the Planck constant, ν is the frequency of the light, k_B is Boltzmann's constant, c is the speed of light and T is the temperature of the material. A material of higher temperature emits more radiation, as exemplified in Figure 5.6A. Using

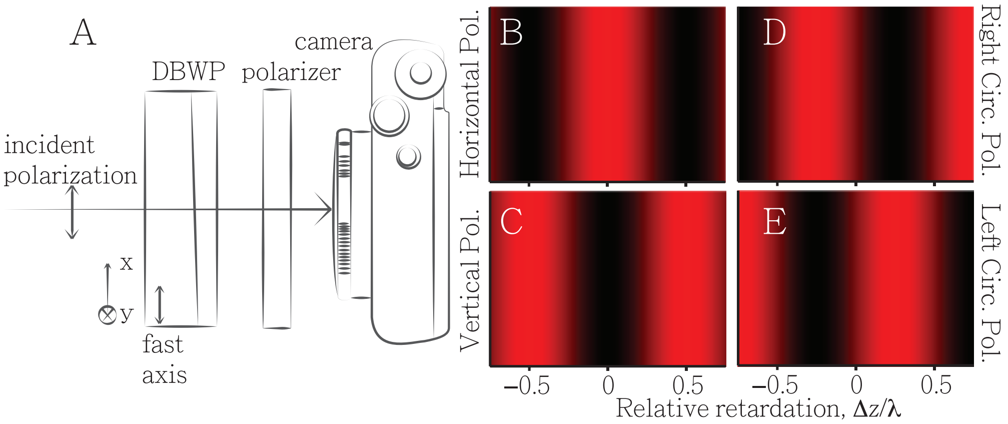

Figure 5.5: Illustration of the polarization states transmitted by the double birefringent wedge prism (DBWP). The polarizer acts as an analyzer, creating different fringe patterns on the camera with different orientation. As the retardation difference between horizontal and vertical polarization depends on x, opposing fringe patterns are transmitted when the polarizer is aligned in either of these states (B-C). Simlarly, assuming two circular polarizers, the fringe patterns move half-way in between the two linear states.

this property, heat cameras can be used to measure the temperature of a material by measuring the radiance in a given optical window in the infrared.

Most elements are, however, not perfect black bodies and therefore emit somewhat lower amounts of radiation. The radiation emitted at a specific wavelength of light depend on the absorptivity, or equivalently on the emissivity, of the material at this frequency. The emissivity can vary between 0 and 1, with low values for highly reflecting materials and high values for highly absorbing materials. As an example, polished gold has a rather poor emissivity as it acts, more or less, as a perfect conductor in the infrared region of the spectrum. Glass, on the other hand, is highly absorbing around 10 μm and has therefore a high emissivity. Often the so-called gray body approximation is used, where the emissivity of a material is assumed not to depend on wavelength. Figure 5.6B show the variation of spectral radiance for emissivities similar to glass and polished gold. Measuring the temperature of glass/gold in thermal equilibrium is therefore easier in the glass case. Furthermore, the emissivity is dependent on the thickness of a given material and often given for an *optically thick* material. Thinner materials, or smaller materials in general, have a reduced emissivity as the radiated power is decreased.

There are different types of detectors in so-called thermal cameras. The detectors may either be cooled or un-cooled and measure in the mid- or long wavelength infrared region (3-8 or 8-14 μm, respectively). Uncooled detectors utilize microbolometers of, for example, vanadium oxide or amorphous Silicon or ferroelectric techniques with barium strontium titanate [215]. The latter uses a ferroelectric phase transition, where the electrical polarization of the material is highly sensitive to temperature. In the microbolometer case, the sensor elements are small and placed on a well thermally isolated large area silicon with low heat capacity. As the incident radiation heats the small sensors the resistance changes and can be converted into an infrared image. Vanadium oxide microbolometer detectors are by far the most common type of detectors today.

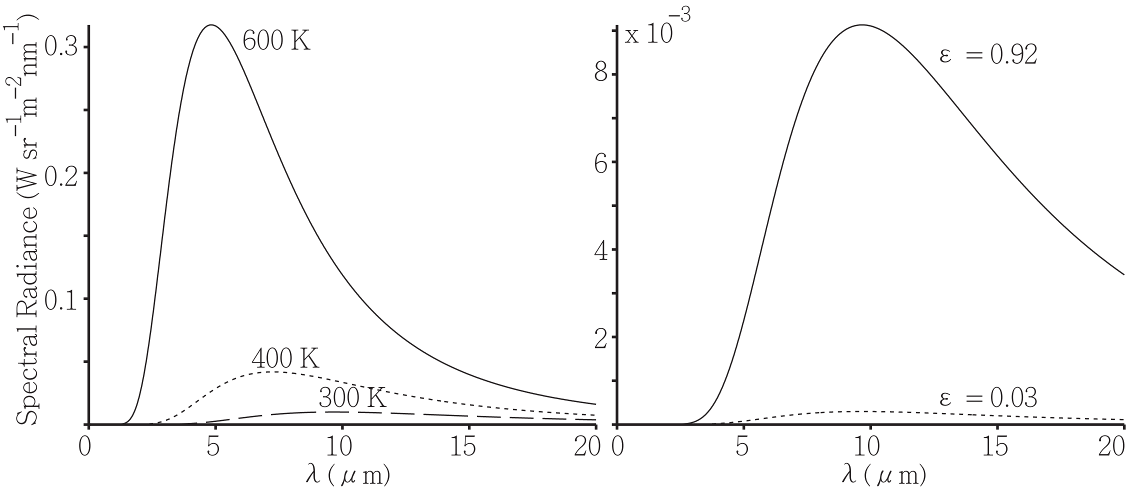

Figure 5.6: Black body radiation. (A) A perfect black body radiation spectrum for different temperatures and (B) gray body radiation at 300 K for two materials with emissivity 0.92 and 0.03.

The large optical absorption cross section of noble metal nanoparticles lead to a significant portion of the incident radiation being converted into heat in the nanoparticles [216–218]. If the nanoparticle would have been floating in vaccuum, completely isolated from other media, the only heat dissipation channel still open would be the radiative emission, i.e. gray body radiation. In other cases, however, heat can be dissipated into neighboring media. The heat dissipation is then related to the materials heat conductivity and heat capacity. For nanoparticles immobilized on a glass substrate, a large portion of the heat does indeed transfer to the supporting material, especially if the ambient element is air, due to the large heat conductivity of glass compared to air [107].

Illuminating a nanoparticle array, with interparticle distances of about two particle diameters, lead to a quick increase in the nanoparticle and supporting materials' temperature, as seen in Figure 5.7. The relative closeness of the nanoparticles lead to a homogeneous temperature throughout the surface, independent on material. Due to the nanoscopic nature of the metal particles and their intrinsic low emissivity, most of the gray body radiation will, however, most likely emerge from the supporting material. Therefore, a first approximation in thermal imaging measurements of nanoparticle array surfaces is to use the emissivity of the supporting material, for example glass. As the nanoparticles cover some portion of the surface, this approximation is most likely an upper limit, especially when considering glass with high emissivity ($\varepsilon > 0.9$). The temperatures measured by the infrared camera is therefore likely to be slightly under estimated from the true values.

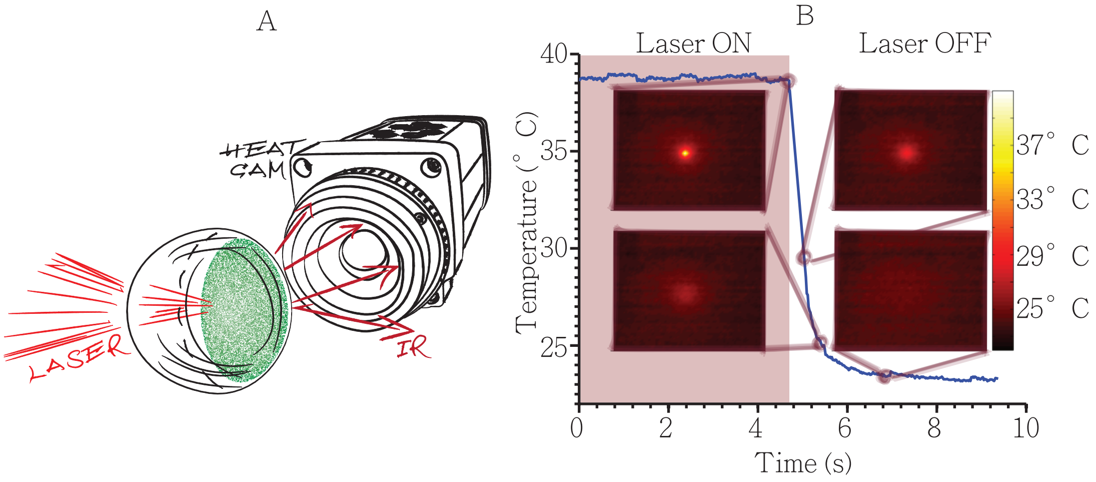

Figure 5.7: Thermal measurements of heat from absorbing nanoparticles. (A) The nanoparticles were illuminated with a monochromatic laser diode from the prism side and an infra-red camera measured the temperature in the illuminated spot. (B) Laser illumiation lead to a temperature that quickly dissipates into the surroundings as the laser is switched off.

Chapter 6

Summary and Outlook

6.1 Summary of Appended Papers

In Paper I, *Refractometric sensing using propagating versus Localized Surface Plasmons: A direct comparison*, a direct comparison of the biosensing properties of propagating surface plasmons (SPRs) in thin films and localized plasmons in nanodisks (LSPRs) were reported. The study used the same interaction chamber, light source and detector for both methodologies. By tuning the SPR and LSPR into the same wavelength range, both bulk refractive index sensitivity and responses to molecular adsorption could be compared. Although the SPR showed almost 20 times larger bulk sensitivity, both methodologies showed the same resonance shifts in actual biorecognition experiments. These effects can be explained by a more the effective field confinement of the nanodisks.

Paper II, *Ultrahigh sensitivity made simple: nanoplasmonic label-free biosensing with an extremely low limit-of-detection for bacterial and cancer diagnostics*, describes several biosensing assays performed, showing extremely low limit-of-detection due to effective noise reduction: The standard deviations of the resonant wavelength were decreased to around 0.1 pm. Two relevant biomarkers were investigated, including prostate specific antigen (PSA), an antigen for prostate cancer, and extracellular adherence protein, which is a marker for *Staphylococcus aureus* detection.

Pushing the number of detectable molecules down even further, Paper III, *Plasmon-Enhanced Colorimetric ELISA with Single Molecule Sensitivity*, shows how one may increase the refractive index footprint of every binding event on nanoparticles through a enzymatic precipitation reaction. The adsorption of horseradish peroxidase (HRP)-conjugated Streptavidin (SA) molecules to biotinylated gold nanoparticles was studied. The subsequent precipitation reaction facilitated using DAB in the presence of H_2O_2 enhances the impact of each individual adsorbed molecule. The enhancement reaction was used to develop a biosensing assay with single molecule sensitivity in measurements of many individual gold nanodisks, using a hyperspectral imaging interrogation technique.

The fourth appended paper IV, *Fano Interference between Localized Plasmons and Interface Reflections*, is more fundamental and describes how to interpret specular reflection spectra from HCL arrays of gold nanodisks as a function of incident angle, surface density of nanoparticles and polarization. It is found that the reflections can be described as an interference effect between the collective scattering in the reflection angle from the nanoparticles and the reflection from a nanoparticle-free interface. The interference can lead to strongly assymmetric resonances, that is, so-called Fano resonances, and strongly dispersive modes.

In paper V, *Plasmon-Enhanced Enzyme-Linked Immunosorbent Assay on Large Arrays of Individual Particles Made by Electron Beam Lithography*, the sources of noise in the sensing system described in paper III is studied. The HRP-SA-assay was studied by following 700 nanoparticles simultaneously using hyperspectral imaging. The main conclusion of the article is that even though the assay has single molecule sensitivity, it may not yet be at the single molecule *resolution*-limit. The reason for the discrepancy is that different precipitates have different morphology and yield different plasmon wavelength shifts depending on the specific adsorption site. Further, the nanoparticles in a given array experience slight refractive index sensitivity variations, which also contributes to the resulting distributions of shifts per particle.

Paper VI, entitled *Complete Light Annihilation in an Ultrathin Layer of Gold Nanoparticles*, stems from the work in paper IV, but is more specific, as we here describe how gold nanodisk arrays can be tuned into a perfect absorption condition, where all incident light of a given wavelength and polarization is absorbed within the array. The condition can be fulfilled when the layers are illuminated above the critical angle of the interface on which it is immobilized. The refraction then cancels the transmitted light and, through complete destructive interference between the scattering from the nanoparticles and the bare interface reflections, the total reflected light can vanish as well. The inserted energy is transformed into heat, which is measured directly using a thermal camera.

Further, zero reflections can be put to good use, as described in paper VII, *Phase-based Optical Biosensing in a Nanoplasmonic Metamaterial Layer*. Here, we utilize the rapid phase changes for wavelengths in the vicinity of the zero reflection condition. The phase varies almost one order of magnitude faster than the reflected intensity. A single wavelength optical setup is developed where the phase between p- and s-polarized reflections can be measured. The phase shows better visibilities of refractive index changes in the medium surrounding the gold nanodisks, both when the entire ambient medium is altered and during molecular adsorption processes.

6.2 Outlook

Light on the nanoscale can be used to increase our understanding of nature, light and material properties on these length scales. Although a significant part of this thesis has been devoted to far-field optical properties, these are directly linked to nanoscale light and interactions. In the following, some ongoing studies are presented, together with a final concluding remark.

Chirality

During the last couple of years, chiral nanostructures have been presented with much larger optical rotation properties compared to chiral molecules and crystals [219–221]. Based on the formalism presented in Chapter 3, giant chirality in achiral anisotropic nanoparticles is possible, when illuminated at an angle. Optical chirality in achiral subwavelength structures has been reported previously and is due to the symmetry break by the illumination angle [222, 223]. The theoretical work, presented in Chapter ,3, however, postulates that complete absorption is possible for right or left handed circularly polarized light, depending on the orientation of the anisotropic nanoparticles. Simultaneously, the absorption of the opposite handedness could be quite low. In such a case, the in-plane surface polarizations, P_x^s and P_y^s, in equation (3.2) are coupled together, leading to off-diagonal reflection components, such as r_{ps} and r_{sp}, that is, optical rotation.

If the absorption difference can be large enough, perhaps larger than 90%, such surfaces can be useful, for instance as a switchable device, which can be turned on or off depending on the phase lag between s- and p-polarized beams. The system would then resemble the coherent perfect absorber with two opposing beams, described in Chapter 3, but with two coherent parallel beams.

Surface Propagation of Light

A more fundamental physics question is regarding the difference between thin metal films and nanoparticles immobilized on a substrate. Both systems show dispersive resonances and complete absorption above the critical angle, when certain constraints are fulfilled. The fundamental differences between these systems should decrease with the nanoparticle surface coverage. It may therefore be interesting to investigate the surface density influence of the system at larger filling factors. Perhaps it is possible to excite propagating modes with un-ordered nanoparticles with long propagation lengths, using much less metal than in a thin film.

In fact, such surface modes are allowed, according to the modified boundary conditions in equation (3.2), although a significant out-of-plane polarizability is needed. In fact, surface densities similar to those used in papers IV and VI, can be used.

Optimized Surface-Enhanced Spectroscopies

As the transmission and reflection can be nullified simultaneously by the metasurface, the absorption of the nanostructures is increased. The absorbed light should lead to enhanced near-fields that could be used, for instance, in surface-enhanced spectroscopies, such as surface-enhanced Raman scattering (SERS) or surface-enhanced fluorescence (SEF).

Similar studies have been conducted with metalayers on top of a metallic mirror [224], with increased signals as a result. If the cheap fabrication process used in paper VI can be applied to achieve complete absorption at normal incidence, for example by fabricating them on top of a mirror/dielectric spacer support, it would surely be an interesting SERS substrate to study. As the technique already has shown great versatility in particles and clusters that can be produced, the combination of complete absorption and confinement of light within, for instance, a nanoparticle dimer gap might lead to further enhancement of the SERS signal.

Furthermore, the directionality and other properties of the Raman scattering would be interesting to study. The Raman scattering is a incoherent process, but there could be some coherency left from the excitation process, leading to directional Raman scattering as well.

Additionally, as a complement to the heat measurements in paper VI, the Raman scattering also provide temperature information. Using the relation between Stokes and anti-Stokes, perhaps the temperature can be measured from a perfect absorber metamaterial.

Angular dependence on Refractive Index Sensitivities

The bulk refractive index sensitivity measured in reflectance has a strong angle dependence, in accordance with the metasurface description in paper IV and Chapter 3. Interestingly, there exists regions where the minimum and/or maximum wavelength of the reflection spectrum will shift to the blue of the original position for increasing refractive index, for instance exemplified in paper VII. The blue shift is counter intuitive since the surface plasmon resonance wavelength red shifts with increased refractive index. However, the spectral feature is not a purely plasmonic response, but a Fano resonance minimum or maximum, which also depend on the strengths of the two interfering components. Thus, the interface reflection itself can cause the effective blue shift, as the reflection generally decreases with increasing refractive index of the ambient for $\theta_i < \theta_c$. Naturally, there exists angles in which the plasmonic and interface response spectrally cancel, leading to no shifts what so ever. Typically, there will be an intensity change, but the spectral position of, for instance, a dip will be constant. The bulk insensitivity could be of use in, for instance, biosensing applications of with high concentrations of protein, like measurements in serum.

The spectral shifts for a given incidence angle and wavelength can also be much larger than expected for a single nanoparticle. However, in order to utilize the sensitivity for molecular sensing purposes, other surface chemistry might be beneficial, for instance, like the dextran matrix used in Biacore's thin film SPP-based sensors. Target molecules can then be adsorbed within the whole dextran volume, which may much thicker than the region probed by the LSPR's of the nanoparticles [225, 226]. Possibly, such an interface may change also the reflection properties from the bare interface, and the high sensitivity to bulk refractive index can be maintained also while studying molecular interactions.

A more challenging measurement methodology is to measure the reflection minimum as a function of angle, again for monochromatic or semimonochromatic light.

If the metasurface is properly designed, the minimum reflection angle should shift upon changes of the local dielectric environment close to the plasmonic nanostructures, for a specific wavelength and polarization. Perhaps it is even possible to design the metasurface to be compatible with the thin film sensing platforms, with samples that could be mounted in, for instance, a Biacore instrument.

Nanoplasmonic Metasurfaces and Individual Nanosensors: A Final Remark

The aim of most surface based biosensors is to detect as small surface coverages of an analyte as possible, and thus also to have low detection limits in terms of volume concentration of analyte. One pathway is to increase the signal-to-noise ratio (SNR) of the instrumental setup or to find means of measurement that yield the largest SNR. The FOM was suggested as a parameter to maximize in order to achieve a more accurate resonance position determination. There has also been other suggestions, such as the alternative FOM*: related to the detected intensity change at a specific wavelength per refractive index change of the surrounding media [157]. However, these parameters are only describing the property of the plasmonic resonator and therefore, the question still remains - what is the optimum measurement technique to achieve the best SNR?

The current trends in nanoplasmonic refractometric sensing include Fano resonances and metamaterials with tailored optical properties. Fano resonances are describing the line-shapes of strongly interacting modes. In plasmonics, at least one of these interacting modes is a plasmon resonance, which may interact with other plasmonic modes or with resonances of other origins, such as waveguides, whispering gallery and Bloch modes [227–229]. Fano resonances based on the strong interaction of metal nanoparticle clusters and multimers are however prominent as they show both narrow and sensitive line shapes [230, 231]. Metamaterials can, for example, be designed to support waveguiding modes, create "superchiral" fields or perfect absorbance of the incident light [171, 232, 233]. These examples have been shown to exhibit interesting sensing properties, such as a better overlap between the resonance mode volume and the sensing medium and the possibility to investigate the supermolecular structure of molecules.

One of the problems with highly interacting multimers and designed metamaterials is the often complicated nanofabrication methods. In Paper IV, we describe the reflections from a short-range ordered nanodisk array sample. Strongly dispersive modes and perfect absorption conditions were found, both properties due to the interference between the nanoparticle scattering and the bare interface reflection. The strong dispersion make the spectral mode highly sensitive to the position and the amplitude of the nanoparticle resonance. It may therefore yield an enhanced spectral response compared to regular transmission measurements. The perfect absorbance, on the other hand, have several advantages. The reflection spectra with deep anti-resonances may be useful in refractometric sensing schemes using angular, phase or intensity modulation detection schemes [103, 233–235]. Furthermore, the deep dip in reflection may increase the SNR, due to the large amplitude of the resonance, and therefore increase the detectability of molecular interactions [83].

The phase detection scheme presented in paper VII, shows the possibility of increasing the sensitivity of metamaterial-based sensors, however, the signal-to-noise ratio (SNR) of a typical molecular interaction was not improved by using this technique. The decreased SNR could, however, be explained by the one order of magnitude cheaper detection scheme used in the experiments. In the future, more work should elucidate the applicability of using phase as an interrogation methodology. Although several reports have suggested improved sensitivity using phase-based sensing schemes [159, 160, 167], none have surpassed the SNR of regular spectroscopic measurements. The miniaturization of the methodology and simpler excitation geometries, such as normal incidence illumination schemes, would increase the usefulness of the methodology. Zero reflection is possible at normal incidence using similar gold nanodisks as presented in paper VI, using a backside mirror and a dielectric spacer. An anisotropic nanoparticle would make phase measurements between two perpendicular polarizations possible also at normal incidence.

So, does nanoplasmonic sensors have a prominent future? There are so-far not many companies around the world that is trying to push the technique to commercialization, despite the great papers and wonderful results published during the last decade in prominent scientific journals. Even though even single molecule sensitivity has been claimed, there is little impact in industry. Perhaps there is a gap between what the nanoplasmonic sensing community provide and the need from the chemical, materials, pharmaceutical, food safety, life science and medical industry. In either case, studying a single nanoparticle over time is not an efficient means of measurement. Although the detection of single molecules may be possible, the time it may take for the single molecule to arrive at the specific nanostructure of interest could be very long [117, 236]. Therefore, the imaging technique used in this work is very interesting, as thousands of individual nanoparticle sensors can be interrogated simultaneously. This improves statistics and can actually increase the sensitivity of the device as a whole [237]. However, the technique is not fast. As single binding event can occur within fractions of a second [119, 120], fast readout is a must, not to smear these signals, if the kinetics of the adsorption process should be studied in detail. As stated in the first Chapter, enabling technologies such as fast, sensitive and stable CCD cameras and bright light sources are key to these kinds of measurements.

As of today, the main advantage of nanoplasmonic sensors is the ease of measurement and the miniaturization possibility. Perhaps the future for LSPR-based sensing is not to compete with large, ready-made sensors, but to be a supporting technique, that can be easily implemented to yield additional information. It can perhaps also be combined with other means of measurement, such as electrical read out, fluorescence, or similar, due to their conductive and strong field enhancement properties.

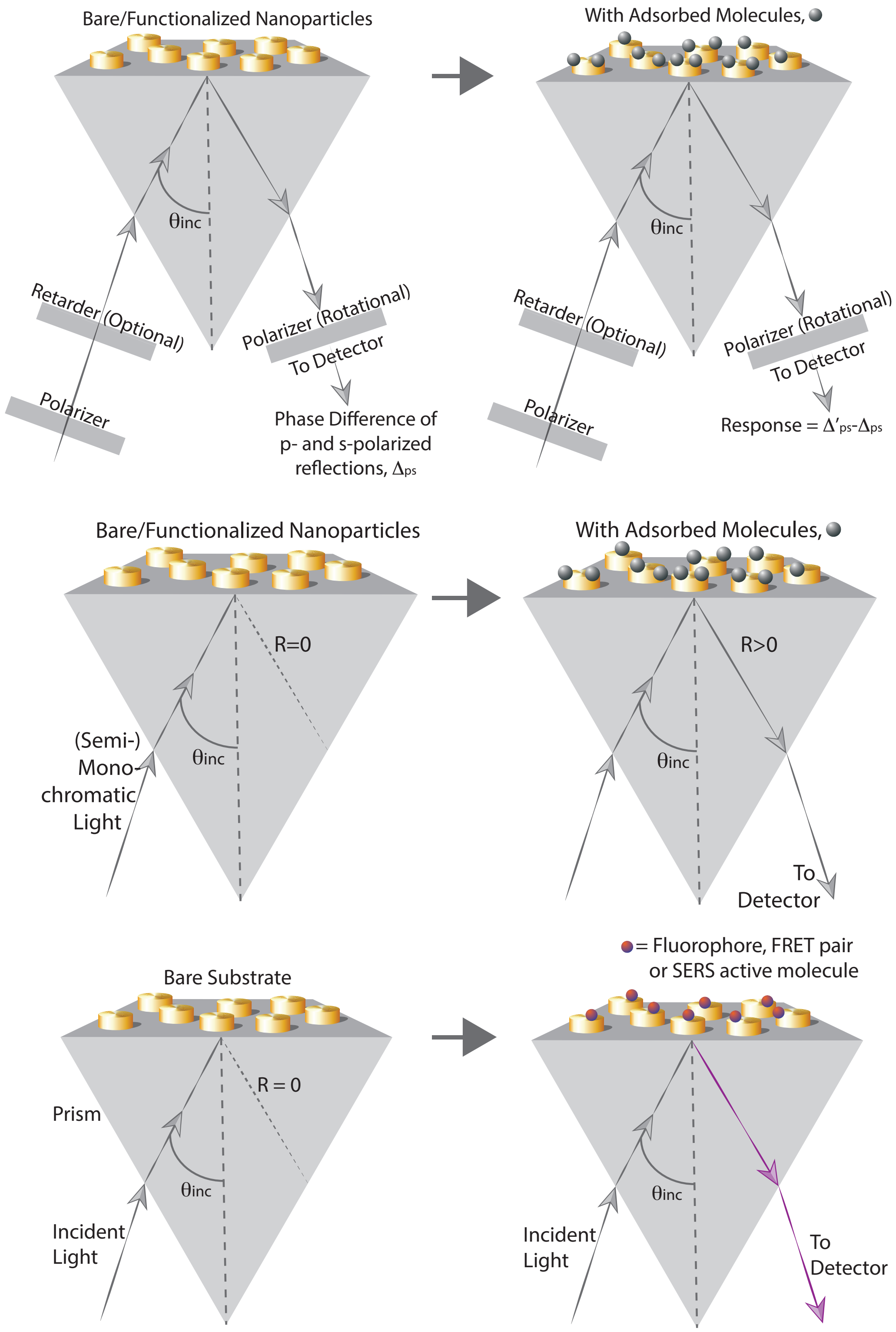

Figure 6.1: Sensing possibilities using zero reflection and complete absorption of light. The zero reflections and complete absorption of light enables enhanced phase sensitivity, background free detection schemes and enhanced optical near fields, applicable for surface enhanced spectroscopies.

Acknowledgments

I wish to thank my supervisor, employer and boss: Professor Mikael Käll for all the opportunities and all the work with our articles, book chapters, patent applications, for pointing out weak points in my arguments and for the great title suggestions. But mainly: Thanks for believing in me.

Next, I would like to thank all the co-authors: Professor Peter Johansson for wonderful numerical assistance and for, sometimes, pointing out things that I should understand....but not really do...or will. Thanks to Si Chen, for all the hard work in our common projects and for letting me help in the small ways that I can. Thanks for all the clean room work, nowadays led by Ruggero and Robin. Thanks Sasha and Per for the work on our sensing papers and projects.

I have spent five years in the same office as Dr. Timur Shegai. I am still amazed over the shear excitement over physics that you have. Remember when you, Björn, Vladimir, Si and others started the old BNPScienceProject? It got us all interacting to a much larger degree, which helped lifting the spirits in the group significantly. OK, perhaps we didn't manage to really DO anything (didn't we make the toy solar cell work?), but still.

Ruggero: Thanks for making me do tons of measurements. Really.

Aron: Thanks for all the work on the SERS project! And for all the nice company in the bars of Umeå...

Tomasz: At least we had a few magical nights in Spain. I know you won't forget them.

I would also like to acknowledge our collaborators at FOI: Per-Ola Andersson, Lars, Christian and Maggan.

Thanks to Vlada, Robin, Kristof, Anni and Gülis for nice companionship in wet, sunny, warm, white and snowy vacations. And to Vladimir, Björn and Koffe for all those evenings and mornings in the gym and on the running track, for all the interesting discussions, the help in courses and in the lab and for all the nice long coffee breaks. Thanks to Mokhtar, Virginia and Ruggero for not letting me kill myself (yet) on the climbing walls.

And again, most importantly, I have to thank all the BNP group members for a great work environment. It seems that even the chem prep lab will be nice with time.

And last, but not least, to my family in Stockholm: I have felt your support during all my time here. It is a strange feeling to be so close, but still so far away. I hope to see you more often in the future.

Bibliography

[1] R. Hooke. *Micrographia or Some physiological descriptions of minute bodies made by magnifying glasses.* London, 1665.

[2] Helmholtz and H. Fripp. On the limits of the optical capacity of the microscope. *The Monthly Microscopical Journal*, 16(1):15–39, 1876.

[3] E. Abbe. The relation of aperture and power in the microscope. *Journal of the Royal Microscopical Society*, 3(6):790–812, 1883.

[4] G. B. Airy. On the diffraction of an object-glass with circular aperture. *Transactions of the Cambridge Philosophical Society*, 5:283–291, 1835.

[5] F.R.S. Rayleigh. Xxxi. investigations in optics, with special reference to the spectroscope. *Philosophical Magazine Series 5*, 8(49):261–274, 1879.

[6] S. W. Hell and J. Wichmann. Breaking the diffracion resolution limit by stimulated-emission - stimulated-emission-depletion fluorescence microscopy. *Optics Letters*, 19(11):780–782, 1994.

[7] S. W. Hell. Far-field optical nanoscopy. *Science*, 316(5828):1153–1158, 2007.

[8] M. J. Rust, M. Bates, and X. Zhuang. Sub-diffraction-limit imaging by stochastic optical reconstruction microscopy (STORM). *Nature Methods*, 3(10):793–795, OCT 2006.

[9] E. Betzig, G. H. Patterson, R. Sougrat, O. W. Lindwasser, S. Olenych, J. S. Bonifacino, M. W. Davidson, J. Lippincott-Schwartz, and H. F. Hess. Imaging intracellular fluorescent proteins at nanometer resolution. *Science*, 313(5793):1642–1645, 2006.

[10] S. T. Hess, T. P. K. Girirajan, and M. D. Mason. Ultra-high resolution imaging by fluorescence photoactivation localization microscopy. *Biophysical Journal*, 91(11):4258–4272, 2006.

[11] Z. Liu, H. Lee, Y. Xiong, C. Sun, and X. Zhang. Far-field optical hyperlens magnifying sub-diffraction-limited objects. *Science*, 315(5819):1686, 2007.

[12] J. B. Pendry. Negative refraction makes a perfect lens. *Phys. Rev. Lett.*, 85:3966–3969, 2000.

[13] I. I. Smolyaninov, Y. J. Hung, and C. C. Davis. Magnifying superlens in the visible frequency range. *Science*, 315(5819):1699–1701, 2007.

[14] E. T. F. Rogers, J. Lindberg, T. Roy, S. Savo, J. E. Chad, M. R. Dennis, and N. I. Zheludev. A super-oscillatory lens optical microscope for subwavelength imaging. *Nature Materials*, 11(5):432–435, 2012.

[15] E. T. F. Rogers and N. I. Zheludev. Optical super-oscillations: sub-wavelength light focusing and super-resolution imaging. *Journal of Optics*, 15(9, SI), 2013.

[16] K. Kneipp, Y. Wang, H. Kneipp, L. T. Perelman, I. Itzkan, R. Dasari, and M. S. Feld. Single molecule detection using surface-enhanced Raman scattering (SERS). *Physical Review Letters*, 78(9):1667–1670, 1997.

[17] S. M. Nie and S. R. Emery. Probing single molecules and single nanoparticles by surface-enhanced raman scattering. *Science*, 275(5303):1102–1106, 1997.

[18] H. X. Xu, E. J. Bjerneld, M. Käll, and L. Borjesson. Spectroscopy of single hemoglobin molecules by surface enhanced raman scattering. *Physical Review Letters*, 83(21):4357–4360, 1999.

[19] A. Ashkin, J. M. Dziedzic, J. E. Bjorkholm, and S. Chu. Observation of a Single-Beam Gradient Force Optical Trap for Dielectric Particles. *Optics Letters*, 11(5):288–290, 1986.

[20] Y. Pang and R. Gordon. Optical trapping of a single protein. *Nano Letters*, 12(1):402–406, 2012.

[21] PV Kamat. Photophysical, photochemical and photocatalytic aspects of metal nanoparticles. *Journal of Physical Chemistry B*, 106(32):7729–7744, 2002.

[22] http://www.nano.gov.

[23] A. P. Alivisatos. Semiconductor clusters, nanocrystals, and quantum dots. *Science*, 271(5251):933–937, 1996.

[24] J. M. Perez, L. Josephson, T. O'Loughlin, D. Hogemann, and R. Weissleder. Magnetic relaxation switches capable of sensing molecular interactions. *Nature Biotechnology*, 20(8):816–820, 2002.

[25] F. Vollmer and S. Arnold. Whispering-gallery-mode biosensing: label-free detection down to single molecules. *Nature Methods*, 5(7):591–596, 2008.

[26] J. Chaste, A. Eichler, J. Moser, G. Ceballos, R. Rurali, and A. Bachtold. A nanomechanical mass sensor with yoctogram resolution. *Nature Nanotechnology*, 7(5):300–303, 2012.

[27] H. J. Chung, C. M. Castro, H. Im, H. Lee, and R. Weissleder. A magneto-DNA nanoparticle system for rapid detection and phenotyping of bacteria. *Nature Nanotechnology*, 8(5):369–375, 2013.

[28] H. Wang, X. Han, X. Ou, C. S. Lee, X. Zhang, and S. T. Lee. Silicon nanowire based single-molecule sers sensor. *Nanoscale*, 5:8172–8176, 2013.

[29] Y. Cui, Q. Q Wei, H. K. Park, and C. M. Lieber. Nanowire nanosensors for highly sensitive and selective detection of biological and chemical species. *Science*, 293(5533):1289–1292, 2001.

[30] S. J. Tans, A. R. M. Verschueren, and C. Dekker. Room-temperature transistor based on a single carbon nanotube. *Nature*, 393(6680):49–52, 1998.

[31] J. Fritz, M. K. Baller, H. P. Lang, H. Rothuizen, P. Vettiger, E. Meyer, H. J. Guntherodt, C. Gerber, and J. K. Gimzewski. Translating biomolecular recognition into nanomechanics. *Science*, 288(5464):316–318, 2000.

[32] R. Berger, E. Delamarche, H. P. Lang, C. Gerber, J. K. Gimzewski, E. Meyer, and H. J. Guntherodt. Surface stress in the self-assembly of alkanethiols on gold. *Science*, 276(5321):2021–2024, 1997.

[33] P. Poncharal, Z. L. Wang, D. Ugarte, and W. A. de Heer. Electrostatic deflections and electromechanical resonances of carbon nanotubes. *Science*, 283(5407):1513–1516, 1999.

[34] P. Spinelli, M. A. Verschuuren, and A. Polman. Broadband omnidirectional antireflection coating based on subwavelength surface Mie resonators. *Nature Communications*, 3, 2012.

[35] J. A. Schuller and M. L. Brongersma. General properties of dielectric optical antennas. *Optics Express*, 17(26):24084–24095, 2009.

[36] E. Yablonovitch. Inhibited Spontaneous Emission in Solid-State Phyiscs and Electronics. *Physical Review Letters*, 58(20):2059–2062, 1987.

[37] S John. Strong Localization of Photons in Certain Disordered Dielectric Superlattices. *Physical Review Letters*, 58(23):2486–2489, 1987.

[38] P. Drude. *Lehrbuch der Optik.* Hirzel, Leipzig, 1900.

[39] G. Mie. Articles on the optical characteristics of turbid tubes, especially colloidal metal solutions. *Journal of Physical Chemistry B*, 25:376–445, 1908.

[40] R.W. Wood. On a remarkable case of uneven distribution of light in a diffraction grating spectrum. *Philosphical Magazine*, 4:396, 1902.

[41] U. Fano. The theory of anomalous diffraction gratings and of quasi-stationary waves on metallic surfaces (sommerfeld's waves). *Journal of the Optical Society of America*, 31:213–222, 1941.

[42] T. Turbadar. Complete Absorption of Light by Thin Metal Films. *Proceedings of the Physical Society of London*, 73(469):40–44, 1959.

[43] A. Otto. Excitation of Nonradiative Surface Plasma Waves in Silver by Method of Frustrated Total Reflection. *Zeitschrift für Physik*, 216(4):398, 1968.

[44] E. Kretschmann and H. Raether. Radiative decay of non radiative surface plasmons excited by light. *Zeitschrift Fur Naturforschung Part a-Astrophysik Physik Und Physikalische Chemie*, A 23(12):2135, 1968.

[45] C. Nylander, B. Liedberg, and T. Lind. Gas-detection by means of surface-plasmon resonance. *Sensors and Actuators*, 3(1):79–88, 1982.

[46] B. Liedberg, C. Nylander, and I. Lundstrom. Surface-plasmon resonance for gas-detection and biosensing. *Sensors and Actuators*, 4(2):299–304, 1983.

[47] L. Novotny and N. van Hulst. Antennas for light. *Nature Photonics*, 5(2):83–90, 2011.

[48] R. F. Oulton, V. J. Sorger, T. Zentgraf, R. M. Ma, C. Gladden, L. Dai, G. Bartal, and X. Zhang. Plasmon lasers at deep subwavelength scale. *Nature*, 461(7264):629–632, 2009.

[49] M. A. Noginov, G. Zhu, A. M. Belgrave, R. Bakker, V. M. Shalaev, E. E. Narimanov, S. Stout, E. Herz, T. Suteewong, and U. Wiesner. Demonstration of a spaser-based nanolaser. *Nature*, 460(7259):1110–U68, 2009.

[50] V. G. Veselago. The electrodynamics of substances with simultaneously negative values of ε and μ. *Soviet Physics Uspekhi*, 10(509), 1968.

[51] J. B. Pendry, D. Schurig, and D. R. Smith. Controlling electromagnetic fields. *Science*, 312(5781):1780–1782, 2006.

[52] N. Yu, P. Genevet, M. A. Kats, F. Aieta, J. P. Tetienne, F. Capasso, and Z. Gaburro. Light Propagation with Phase Discontinuities: Generalized Laws of Reflection and Refraction. *Science*, 334(6054):333–337, 2011.

[53] S. Zhang, D. A. Genov, Y. Wang, M. Liu, and X. Zhang. Plasmon-induced transparency in metamaterials. *Physical Review Letters*, 101(4), 2008.

[54] B. Luk'yanchuk, N. I. Zheludev, S. A. Maier, N. J. Halas, P. Nordlander, H. Giessen, and C. T. Chong. The fano resonance in plasmonic nanostructures and metamaterials. *Nature Materials*, 9(9):707–715, 2010.

[55] T. Xu, A. Agrawal, M. Abashin, K. J. Chau, and H. J. Lezec. All-angle negative refraction and active flat lensing of ultraviolet light. *Nature*, 497(7450):470–474, 2013.

[56] M. Fleischmann, P. J. Hendra, and A. J. Mcquillan. Raman spectra of pyridine absobed at a silver electrode. *Chem. Phys. Lett.*, 26:163, 1974.

[57] D. L. Jeanmaire and R. P. van Duyne. Surface Raman spectroelectrochemistry: Part I. Heterocyclic, aromatic, and aliphatic amines adsobed on the anodized silver electrode. *J. Electroanal. Chem. Phys. Lett.*, 84:1, 1977.

[58] M. Moskovits. Surface roughness and the enhanced intensity of raman scattering by molecules absobed on metals. *J. Chem. Phys.*, 69 (9):4159, 1978.

[59] K. H. Drexhage. Influence of a dielectric interface on fluorescence decay time. *Journal of Luminescence*, 1-2:693–701, 1970.

[60] A. M. Glass, P. F. Liao, J. G. Bergman, and D. H. Olson. Interaction of metal particles with adsorbed dye molecules. *Optics Letters*, 5(9):368–370, 1980.

[61] H. A. Atwater and A. Polman. Plasmonics for improved photovoltaic devices. *Nature Materials*, 9(3):205–213, 2010.

[62] J. L. West and N. J. Halas. Engineered nanomaterials for biophotonics applications: Improving sensing, imaging, and therapeutics. *Annual Review of Biomedical Engineering*, 5:285–292, 2003.

[63] P. B. Johnson and R. W. Christy. Optical-constants of noble-metals. *Physical Review B*, 6(12):4370–4379, 1972.

[64] E. Palik. *Handbook of Optical Constants of Solids.* Academic Press, 1997.

[65] A. D. Rakic, A. B. Djurisic, J. M. Elazar, and M. L. Majewski. Optical properties of metallic films for vertical-cavity optoelectronic devices. *Applied Optics*, 37(22):5271–5283, 1998.

[66] M. Born and E. Wolf. *Principles of Optics.* Pergamon, 1959.

[67] J. D. Jackson. *Classical Electrodynamics, third edition.* John Wiley & Sons, 1999.

[68] D. Bedeaux and J. Vlieger. *Optical Properties of Surfaces.* Imperial College Press, London, 2001.

[69] E. J. Zeman and G. C. Schatz. An Accurate Electromagnetic Theory Study of Surface Enhancement Factors for Ag, Au, Cu, Li, Na, Al, Ga, In, Zn, and Cd. *Journal of Physical Chemistry*, 91(3):634–643, 1987.

[70] W. H. Yang, G. C. Schatz, and R. P. Van Duyne. Discret Dipole Approximation for Calculating Extinction and Raman Intensities for Small Particles with Arbitrary Shapes. *Journal of Chemical Physics*, 103(3):869–875, 1995.

[71] S. A. Maier. Plasmonic field enhancement and SERS in the effective mode volume picture. *Optics Express*, 14(5):1957–1964, 2006.

[72] B. T. Draine and P. J. Flatau. Discrete-dipole approximation for scattering calculations. *Journal of the Optical Society of America a-Optics Image Science and Vision*, 11(4):1491–1499, 1994.

[73] H. Devoe. Optical properties of molecular aggregates .i. classical model of electronic absorption and refraction. *Journal of Chemical Physics*, 41(2):393, 1964.

[74] E. M. Hicks, S. L. Zou, G. C. Schatz, K. G. Spears, R. P. van Duyne, L. Gunnarsson, T. Rindzevicius, B. Kasemo, and M. Käll. Controlling plasmon line shapes through diffractive coupling in linear arrays of cylindrical nanoparticles fabricated by electron beam lithography. *Nano Letters*, 5(6):1065–1070, 2005.

[75] F. J. Garcia de Abajo. Colloquium: Light scattering by particle and hole arrays. *Reviews of Modern Physics*, 79(4):1267–1290, 2007.

[76] B. Auguie and W. L. Barnes. Collective resonances in gold nanoparticle arrays. *Physical Review Letters*, 101(14), 2008.

[77] T. J. Antosiewicz, S. P. Apell, M. Zach, I. Zoric, and C. Langhammer. Oscillatory Optical Response of an Amorphous Two-Dimensional Array of Gold Nanoparticles. *Physical Review Letters*, 109(24), 2012.

[78] J. C. M. Garnett. Colours in metal glasses and in metallic films. *Proceedings of the Royal Society of London*, 73(495):443–445, 1904.

[79] E. David. Interpretation of the anomalies of the optical constants of thin metal layers. *Zeitschrift fur physik*, 114(7-8):389–406, 1939.

[80] S. Yamaguchi. Theory of optical properties of very thin inhomogeneous films. *Journal of the physical society of Japan*, 17(1):184–193, 1962.

[81] T. Yamaguchi, S. Yoshida, and A. Kinbara. Optical effect of substrate on anomalous absorption of aggregated silver films. *Thin solid films*, 21(1):173–187, 1974.

[82] A. Mendoza-Galvan, K. Jarrendahl, A. Dmitriev, T. Pakizeh, M. Kall, and H. Arwin. Optical response of supported gold nanodisks. *Optics Express*, 19(13):12093–12107, 2011.

[83] M. A. Otte, M. C. Estevez, D. Regatos, L. M. Lechuga, and B. Sepulveda. Guiding Light in Monolayers of Sparse and Random Plasmonic Meta-atoms. *ACS Nano*, 5(11):9179–9186, 2011.

[84] A. Mendoza-Galvan, K. Jarrendahl, A. Dmitriev, T. Pakizeh, M. Kall, and H. Arwin. Fano interference in supported gold nanosandwiches with weakly coupled nanodisks. *Optics Express*, 20(28):29646–29658, 2012.

[85] J. K. Gansel, M. Thiel, M. S. Rill, M. Decker, K. Bade, V. Saile, G. von Freymann, S. Linden, and M. Wegener. Gold Helix Photonic Metamaterial as Broadband Circular Polarizer. *Science*, 325(5947):1513–1515, 2009.

[86] H. Fredriksson, Y. Alaverdyan, A. Dmitriev, C. Langhammer, D. S. Sutherland, M. Zaech, and B. Kasemo. Hole-mask colloidal lithography. *Advanced Materials*, 19(23):4297, 2007.

[87] T. Shegai, S. Chen, V. D. Miljkovic, G. Zengin, P. Johansson, and M. Käll. A bimetallic nanoantenna for directional colour routing. *Nature Communications*, 2:481, 2011. doi: 10.1038/ncomms1490.

[88] A. Dmitriev, T. Pakizeh, M. Käll, and D. S. Sutherland. Gold-silica-gold nanosandwiches: Tunable bimodal plasmonic resonators. *Small*, 3(2):294–299, 2007.

[89] S. Thongrattanasiri and J. F. Garcia de Abajo. Optical Field Enhancement by Strong Plasmon Interaction in Graphene Nanostructures. *Physical Review Letters*, 110(18), 2013.

[90] U Fano. Effects of Configuration Interaction on Intensities and Phase Shifts. *Physical Review*, 124(6):1866–1878, 1961.

[91] A. E. Miroshnichenko, S. Flach, and Y. S. Kivshar. Fano resonances in nanoscale structures. *Reviews of Modern Physics*, 82(3):2257–2298, 2010.

[92] Y. D. Chong, Li Ge, Hui Cao, and A. D. Stone. Coherent Perfect Absorbers: Time-Reversed Lasers. *Physical Review Letters*, 105(5), 2010.

[93] W. Wan, Y. Chong, L. Ge, H. Noh, A. D. Stone, and H. Cao. Time-Reversed Lasing and Interferometric Control of Absorption. *Science*, 331(6019):889–892, 2011.

[94] H. Noh, Y. Chong, A. D. Stone, and H. Cao. Perfect coupling of light to surface plasmons by coherent absorption. *Physical Review Letters*, 108(18), 2012.

[95] B. Sernelius. *Surface modes in physics*. Wiley-VCH, Berlin, 2001.

[96] F. Goos and H. Hanchen. Ein neuer und fundamentaler versuch zur totalreflexion. *Annalen der Physik*, 1(7-8):333–346, 1947.

[97] C. Imbert. Calculation and experimental proof of transverse shift induced by total internal reflection of circularly polarized-light beam. *Physical Review D*, 5(4):787, 1972.

[98] F Abeles. Surface Electromagnetic Waves Ellipsometry. *Surface Science*, 56(1):237–251, 1976.

[99] A. A. Kruchinin and Y. G. Vlasov. Surface plasmon resonance monitoring by means of polarization state measurement in reflected light as the basis of a DNA-probe biosensor. *Sensors and Actuators B-Chemical*, 30(1):77–80, 1996.

[100] S. G. Nelson, K. S. Johnston, and S. S. Yee. High sensitivity surface plasmon resonance sensor based on phase detection. *Sensors and Actuators B-Chemical*, 35(1-3):187–191, 1996.

[101] A. V. Kabashin and P. I. Nikitin. Interferometer based on a surface-plasmon resonance for sensor applications. *Quantum Electronics*, 27(7):653–654, 1997.

[102] A. V. Kabashin and P. I. Nikitin. Surface plasmon resonance interferometer for bio- and chemical-sensors. *Optics Communications*, 150(1-6):5–8, 1998.

[103] Y. H. Huang, H. P. Ho, S. Y. Wu, and S. K. Kong. Detecting phase shifts in surface plasmon resonance: A review. *Advances in Optical Technologies*, 2012:12, 2011.

[104] Y. Huang, H. P. Ho, S. K. Kong, and A. V. Kabashin. Phase-sensitive surface plasmon resonance biosensors: methodology, instrumentation and applications. *Annalen der Physik*, 524(11):637–662, 2012.

[105] J. Gersten and A. Nitzan. Spectroscopic Preoperties of Molecules Interacting with Small Dielectric Particles. *Journal of Chemical Physics*, 75(3):1139–1152, 1981.

[106] W. Zhang, L. Huang, C. Santschi, and O. J. F. Martin. Trapping and Sensing 10 nm Metal Nanoparticles Using Plasmonic Dipole Antennas. *Nano Letters*, 10(3):1006–1011, 2010.

[107] K. Wang, E. Schonbrun, P. Steinvurzel, and K. B. Crozier. Trapping and rotating nanoparticles using a plasmonic nano-tweezer with an integrated heat sink. *Nature Communications*, 2, 2011.

[108] P. Christopher, D. B. Ingram, and S. Linic. Enhancing Photochemical Activity of Semiconductor Nanoparticles with Optically Active Ag Nanostructures: Photochemistry Mediated by Ag Surface Plasmons. *Journal of Physical Chemistry C*, 114(19):9173–9177, 2010.

[109] C. Wadell, T. J. Antosiewicz, and C. Langhammer. Optical Absorption Engineering in Stacked Plasmonic Au-SiO2-Pd Nanoantennas. *Nano Letters*, 12(9):4784–4790, 2012.

[110] S. Mubeen, J. Lee, N. Singh, S. Kraemer, G. D. Stucky, and M. Moskovits. An autonomous photosynthetic device in which all charge carriers derive from surface plasmons. *Nature Nanotechnology*, 8(4):247–251, 2013.

[111] M. J. Kale, T. Avanesian, and P. Christopher. Direct Photocatalysis by Plasmonic Nanostructures. *ACS Catalysis*, 4(1):116–128, 2014.

[112] A. J. Qavi, A. L. Washburn, J.-Y. Byeon, and R. C. Bailey. Label-free technologies for quantitative multiparameter biological analysis. *Analytical and Bioanalytical Chemistry*, 394(1):121–135, 2009.

[113] X. Fan, I. M. White, S. I. Shopova, H. Zhu, J. D. Suter, and Y. Sun. Sensitive optical biosensors for unlabeled targets: A review. *Analytica Chimica Acta*, 620(1-2):8–26, 2008.

[114] S. Mandal and D. Erickson. Nanoscale optofluidic sensor arrays. *Optics Express*, 16(3):1623–1631, 2008.

[115] K. Maehashi, T. Katsura, K. Kerman, Y. Takamura, K. Matsumoto, and E. Tamiya. Label-free protein biosensor based on aptamer-modified carbon nanotube field-effect transistors. *Analytical Chemisrty*, 79(2):782–787, 2007.

[116] M. Yue, J. C. Stachowiak, H. Lin, R. Datar, R. Cote, and A. Majumdar. Label-free protein recognition two-dimensional array using nanomechanical sensors. *Nano Letters*, 8(2):520–524, 2008.

[117] T. M. Squires, R. J. Messinger, and S. R. Manalis. Making it stick: convection, reaction and diffusion in surface-based biosensors. *Nature Biotechnology*, 26(4):417–426, 2008.

[118] J. M. Bingham, K. A. Willets, N. C. Shah, D. Q. Andrews, and R. P. Van Duyne. Localized surface plasmon resonance imaging: Simultaneous single nanoparticle spectroscopy and diffusional dynamics. *Journal of Physical Chemistry C*, 113(39):16839–16842, 2009.

[119] I. Ament, J. Prasad, A. Henkel, S. Schmachtel, and C. Soennichsen. Single Unlabeled Protein Detection on Individual Plasmonic Nanoparticles. *Nano Letters*, 12(2):1092–1095, 2012.

[120] P. Zijlstra, P. M. R. Paulo, and M. Orrit. Optical detection of single non-absorbing molecules using the surface plasmon resonance of a gold nanorod. *Nature Nanotechnology*, 7(6):379–382, 2012.

[121] D. Wassaf, G. N. Kuang, K. Kopacz, Q. L. Wu, Q. Nguyen, M. Toews, J. Cosic, J. Jacques, S. Wiltshire, J. Lambert, C. C. Pazmany, S. Hogan, R. C. Ladner, A. E. Nixon, and D. J. Sexton. High-throughput affinity ranking of antibodies using surface plasmon resonance microarrays. *Analytical Biochemistry*, 351(2):241–253, 2006.

[122] I. Navratilova and A. L. Hopkins. Fragment screening by surface plasmon resonance. *Acs Medicinal Chemistry Letters*, 1(1):44–48, 2010.

[123] A. Guidi, L. Laricchia-Robbio, D. Gianfaldoni, R. Revoltella, and G. Del Bono. Comparison of a conventional immunoassay (elisa) with a surface plasmon resonance-based biosensor for igf-1 detection in cows' milk. *Biosensors & Bioelectronics*, 16(9-12):971–977, 2001.

[124] D. Wei, O. A. Oyarzabal, T. S. Huang, S. Balasubramanian, S. Sista, and A. L. Simoman. Development of a surface plasmon resonance biosensor for the identification of campylobacter jejuni. *Journal of Microbiological Methods*, 69(1):78–85, 2007.

[125] J. P. Ferguson, G. A. Baxter, J. D. G. McEvoy, S. Stead, E. Rawlings, and M. Sharman. Detection of streptomycin and dihydrostreptomycin residues in milk, honey and meat samples using an optical biosensor. *Analyst*, 127(7):951–956, 2002.

[126] S. R. H. Crooks, G. A. Baxter, M. C. O'Connor, and C. T. Elliot. Immunobiosensor - an alternative to enzyme immunoassay screening for residues of two sulfonamides in pigs. *Analyst*, 123(12):2755–2757, 1998.

[127] C. E. Nilsson, S. Abbas, M. Bennemo, A. Larsson, M. D. Hamalainen, and A. Frostell-Karlsson. A novel assay for influenza virus quantification using surface plasmon resonance. *Vaccine*, 28(3):759–766, 2010.

[128] A. N. Naimushin, S. D. Soelberg, D. K. Nguyen, L. Dunlap, D. Bartholomew, J. Elkind, J. Melendez, and C. E. Furlong. Detection of staphylococcus aureus enterotoxin b at femtomolar levels with a miniature integrated two-channel surface plasmon resonance (spr) sensor. *Biosensors & Bioelectronics*, 17(6-7):573–584, 2002.

[129] A. D. Taylor, J. Ladd, Q. M. Yu, S. F. Chen, J. Homola, and S. Y. Jiang. Quantitative and simultaneous detection of four foodborne bacterial pathogens with a multi-channel spr sensor. *Biosensors & Bioelectronics*, 22(5):752–758, 2006.

[130] J. Homola. *Surface Plasmon Resonance Based Sensors.* Springer Series on Chemical Sensors and Biosensors. Springer, Berlin, 2006.

[131] T. C. J. Gribnau, J. H. W. Leuvering, and H. Vanhell. Particle-Labeled Immunoassays - A Review. *Journal of Chromatography*, 376:175–189, 1986.

[132] P. Englebienne. Use of colloidal gold surface plasmon resonance peak shift to infer affinity constants from the interactions between protein antigens and antibodies specific for single or multiple epitopes. *Analyst*, 123(7):1599–1603, 1998.

[133] P. Neuxil and J. Reboud. Palm-sized biodetection system based on localized surface plasmon resonance. *Analytical Chemistry*, 80(15):6100–6103, 2008.

[134] T. Okamoto, I. Yamaguchi, and T. Kobayashi. Local plasmon sensor with gold colloid monolayers deposited upon glass substrates. *Optics Letters*, 25(6):372–374, 2000.

[135] N. Nath and A. Chilkoti. A colorimetric gold nanoparticle sensor to interrogate biomolecular interactions in real time on a surface. *Analytical Chemistry*, 74(3):504–509, 2002.

[136] M. D. Malinsky, K. L. Kelly, G. C. Schatz, and R. P. Van Duyne. Chain length dependence and sensing capabilities of the localized surface plasmon resonance of silver nanoparticles chemically modified with alkanethiol self-assembled monolayers. *Journal of the American Chemical Society*, 123(7):1471–1482, 2001.

[137] M. Himmelhaus and H. Takei. Cap-shaped gold nanoparticles for an optical biosensor. *Sensors and Actuators B-Chemical*, 63(1-2):24–30, 2000.

[138] A. J. Haes and R. P. Van Duyne. A nanoscale optical blosensor: Sensitivity and selectivity of an approach based on the localized surface plasmon resonance spectroscopy of triangular silver nanoparticles. *Journal of the American Chemical Society*, 124(35):10596–10604, 2002.

[139] S. S. Acimovic, M. P. Kreuzer, M. U. Gonzalez, and R. Quidant. Plasmon Near-Field Coupling in Metal Dimers as a Step toward Single-Molecule Sensing. *ACS Nano*, 3(5):1231–1237, 2009.

[140] M. M. Miller and A. A. Lazarides. Sensitivity of metal nanoparticle surface plasmon resonance to the dielectric environment. *Journal of Physical Chemistry B*, 109(46):21556–21565, 2005.

[141] L. J. Sherry, R. C. Jin, C. A. Mirkin, G. C. Schatz, and R. P. Van Duyne. Localized surface plasmon resonance spectroscopy of single silver triangular nanoprisms. *Nano Letters*, 6(9):2060–2065, 2006.

[142] P. Kvasnicka and J. Homola. Optical sensors based on spectroscopy of localized surface plasmons on metallic nanoparticles: Sensitivity considerations. *Biointerphases*, 3(3):FD4–FD11, 2008.

[143] F. Wang and Y. R. Shen. General properties of local plasmons in metal nanostructures. *Physical Review Letters*, 97(20), 2006.

[144] A. Dmitriev, C. Hagglund, S. Chen, H. Fredriksson, T. Pakizeh, M. Käll, and D. S. Sutherland. Enhanced Nanoplasmonic Optical Sensors with Reduced Substrate Effect. *Nano Letters*, 8(11):3893–3898, 2008.

[145] L. S. Jung, C. T. Campbell, T. M. Chinowsky, M. N. Mar, and S. S. Yee. Quantitative interpretation of the response of surface plasmon resonance sensors to adsorbed films. *Langmuir*, 14(19):5636–5648, 1998.

[146] J. A. Defeijter, J. Benjamins, and F. A. Veer. Ellipsometry as a tool to study adsorption behavior of synthetic and biopolymers at air-water-interface. *Biopolymers*, 17(7):1759–1772, 1978.

[147] H. X. Xu and M. Käll. Modeling the optical response of nanoparticle-based surface plasmon resonance sensors. *Sensors and Actuators B-Chemical*, 87(2):244–249, 2002.

[148] T. Rindzevicius, Y. Alaverdyan, M. Kall, W. A. Murray, and W. L. Barnes. Long-range refractive index sensing using plasmonic nanostructures. *Journal of Physical Chemistry C*, 111(32):11806–11810, 2007.

[149] P. K. Jain, W. Y. Huang, and M. A. El-Sayed. On the universal scaling behavior of the distance decay of plasmon coupling in metal nanoparticle pairs: A plasmon ruler equation. *Nano Letters*, 7(7):2080–2088, 2007.

[150] A. D. McFarland and R. P. Van Duyne. Single silver nanoparticles as real-time optical sensors with zeptomole sensitivity. *Nano Letters*, 3(8):1057–1062, 2003.

[151] A. B. Dahlin, J. O. Tegenfeldt, and F. Hook. Improving the instrumental resolution of sensors based on localized surface plasmon resonance. *Analytical Chemistry*, 78(13):4416–4423, 2006.

[152] A. B. Dahlin, S. Chen, M. P. Jonsson, L. Gunnarsson, M. Käll, and F. Höök. High-resolution microspectroscopy of plasmonic nanostructures for miniaturized biosensing. *Analytical Chemistry*, 81(16):6572–6580, 2009.

[153] K. Hedsten, J. Fonollosa, P. Enoksson, P. Modh, J. Bengtsson, D. S. Sutherland, and A. Dmitriev. Optical Label-Free Nanoplasmonic Biosensing Using a Vertical-Cavity Surface-Emitting Laser and Charge-Coupled Device. *Analytical Chemistry*, 82(4):1535–1539, 2010.

[154] G. Bellapadrona, A. B. Tesler, D. Gruenstein, L. H. Hossain, R. Kikkeri, P. H. Seeberger, A. Vaskevich, and I. Rubinstein. Optimization of Localized Surface Plasmon Resonance Transducers for Studying Carbohydrate-Protein Interactions. *Analytical Chemistry*, 84(1):232–240, 2012.

[155] O. Kedem, A. B. Tesler, A. Vaskevich, and I. Rubinstein. Sensitivity and Optimization of Localized Surface Plasmon Resonance Transducers. *ACS Nano*, 5(2):748–760, 2011.

[156] A. Tittl, P. Mai, R. Taubert, D. Dregely, N. Liu, and H. Giessen. Palladium-Based Plasmonic Perfect Absorber in the Visible Wavelength Range and Its Application to Hydrogen Sensing. *Nano Letters*, 11(10):4366–4369, 2011.

[157] J. Becker, A. Trugler, A. Jakab, U. Hohenester, and C. Sonnichsen. The optimal aspect ratio of gold nanorods for plasmonic bio-sensing. *Plasmonics*, 5(2):161–167, 2010.

[158] M. Piliarik, H. Sipova, P. Kvasnicka, N. Galler, J. R. Krenn, and J. Homola. High-resolution biosensor based on localized surface plasmons. *Optics Express*, 20(1):672–680, 2012.

[159] V. G. Kravets, F. Schedin, A. V. Kabashin, and A. N. Grigorenko. Sensitivity of collective plasmon modes of gold nanoresonators to local environment. *Optics Letters*, 35(7):956–958, 2010.

[160] V. G. Kravets, F. Schedin, R. Jalil, L. Britnell, R. V. Gorbachev, D. Ansell, B. Thackray, K. S. Novoselov, A. K. Geim, A. V. Kabashin, and A. N. Grigorenko. Singular phase nano-optics in plasmonic metamaterials for label-free single-molecule detection. *Nature Materials*, 12(4):304–309, 2013.

[161] A. R. Halpern, Y. Chen, R. M. Corn, and D. Kim. Surface Plasmon Resonance Phase Imaging Measurements of Patterned Mono layers and DNA Adsorption onto Microarrays. *Analytical Chemistry*, 83(7):2801–2806, 2011.

[162] H. M. Hiep, H. Yoshikawa, M. Saito, and E. Tamiya. An Interference Localized Surface Plasmon Resonance Biosensor Based on the Photonic Structure of Au Nanoparticles and SiO2/Si Multilayers. *ACS Nano*, 3(2):446–452, 2009.

[163] H. M. Hiep, H. Yoshikawa, and E. Tamiya. Interference Localized Surface Plasmon Resonance Nanosensor Tailored for the Detection of Specific Biomolecular Interactions. *Analytical Chemistry*, 82(4):1221–1227, FEB 15 2010.

[164] T. Sannomiya, T. E. Balmer, C. Hafner, M. Heuberger, and J. Voros. Optical sensing and determination of complex reflection coefficients of plasmonic structures using transmission interferometric plasmonic sensor. *Review of Scientific Instruments*, 81(5), 2010. Sannomiya, Takumi Balmer, Tobias E. Hafner, Christian Heuberger, Manfred Voeroes, Janos.

[165] R. Ameling, L. Langguth, M. Hentschel, M. Mesch, P. V. Braun, and H. Giessen. Cavity-enhanced localized plasmon resonance sensing. *Applied Physics Letters*, 97(25), 2010.

[166] M. A. Schmidt, D. Y. Lei, L. Wondraczek, V. Nazabal, and S. A. Maier. Hybrid nanoparticle-microcavity-based plasmonic nanosensors with improved detection resolution and extended remote-sensing ability. *Nature Communications*, 3, 2012.

[167] K. Lodewijks, W. Van Roy, G. Borghs, L. Lagae, and P. Van Dorpe. Boosting the Figure-Of-Merit of LSPR-Based Refractive Index Sensing by Phase-Sensitive Measurements. *Nano Letters*, 12(3):1655–1659, 2012.

[168] L. Novotny. Effective wavelength scaling for optical antennas. *Physical Review Letters*, 98(26), 2007.

[169] A. B. Evlyukhin, S. I. Bozhevolnyi, A. Pors, M. G. Nielsen, I. P. Radko, M. Willatzen, and O. Albrektsen. Detuned electrical dipoles for plasmonic sensing. *Nano Letters*, 10(11):4571–4577, 2010.

[170] T. Shegai, P. Johansson, C. Langhammer, and M. Käll. Directional Scattering and Hydrogen Sensing by Bimetallic Pd-Au Nanoantennas. *Nano Letters*, 12(5):2464–2469, 2012.

[171] E. Hendry, T. Carpy, J. Johnston, M. Popland, R. V. Mikhaylovskiy, A. J. Lapthorn, S. M. Kelly, L. D. Barron, N. Gadegaard, and M. Kadodwala. Ultrasensitive detection and characterization of biomolecules using superchiral fields. *Nature Nanotechnology*, 5(11):783–787, 2010.

[172] W. Ma, H. Kuang, L. Xu, L. Ding, C. Xu, Li. Wang, and N. A. Kotov. Attomolar DNA detection with chiral nanorod assemblies. *Nature Communications*, 4, 2013.

[173] A. O. Govorov, Z. Fan, P. Hernandez, J. M. Slocik, and R. R. Naik. Theory of Circular Dichroism of Nanomaterials Comprising Chiral Molecules and Nanocrystals: Plasmon Enhancement, Dipole Interactions, and Dielectric Effects. *Nano Letters*, 10(4):1374–1382, 2010.

[174] A. O. Govorov. Plasmon-Induced Circular Dichroism of a Chiral Molecule in the Vicinity of Metal Nanocrystals. Application to Various Geometries. *Journal of Physical Chemistry C*, 115(16):7914–7923, 2011.

[175] I. Dolamic, S. Knoppe, A. Dass, and T. Buergi. First enantioseparation and circular dichroism spectra of Au-38 clusters protected by achiral ligands. *Nature Communications*, 3, 2012.

[176] N. A. Abdulrahman, Z. Fan, T. Tonooka, S. M. Kelly, N. Gadegaard, E. Hendry, A. O. Govorov, and M. Kadodwala. Induced Chirality through Electromagnetic Coupling between Chiral Molecular Layers and Plasmonic Nanostructures. *Nano Letters*, 12(2):977–983, 2012.

[177] A. Garcia-Etxarri and J. A. Dionne. Surface-enhanced circular dichroism spectroscopy mediated by nonchiral nanoantennas. *Physical Review B*, 87(23), 2013.

[178] F. Lu, Y. Tian, M. Liu, D. Su, H. Zhang, A. O. Govorov, and O. Gang. Discrete Nanocubes as Plasmonic Reporters of Molecular Chirality. *Nano Letters*, 13(7):3145–3151, 2013.

[179] B. M. Maoz, Y. Chaikin, A. B. Tesler, O. Bar Elli, Z. Fan, A. O. Govorov, and G. Markovich. Amplification of Chiroptical Activity of Chiral Biomolecules by Surface Plasmons. *Nano Letters*, 13(3):1203–1209, 2013.

[180] M. Tokeshi, M. Uchida, A. Hibara, T. Sawada, and T. Kitamori. Determination of subyoctomole amounts of nonfluorescent molecules using a thermal lens microscope: Subsingle molecule determination. *Analytical Chemistry*, 73(9):2112–2116, 2001.

[181] D. Boyer, P. Tamarat, A. Maali, B. Lounis, and M. Orrit. Photothermal imaging of nanometer-sized metal particles among scatterers. *Science*, 297(5584):1160–1163, 2002.

[182] A. Gaiduk, M. Yorulmaz, P. V. Ruijgrok, and M. Orrit. Room-Temperature Detection of a Single Molecule's Absorption by Photothermal Contrast. *Science*, 330(6002):353–356, 2010.

[183] A. B. Dahlin. *Plasmonic Biosensors: An Integrated View of Refractometric Sensors*. IOP Press, 2012.

[184] M. P. Jonsson, A. B. Dahlin, L. Feuz, S. Petronis, and F. Hook. Locally functionalized short-range ordered nanoplasmonic pores for bioanalytical sensing. *Analytical Chemistry*, 82(5):2087–2094, 2010. Jonsson, Magnus P. Dahlin, Andreas B. Feuz, Laurent Petronis, Sarunas Hook, Fredrik.

[185] L. Feuz, P. Jonsson, M. P. Jonsson, and F. Hook. Improving the limit of detection of nanoscale sensors by directed binding to high-sensitivity areas. *Acs Nano*, 4(4):2167–2177, 2010.

[186] L. Feuz, M. P. Jonsson, and F Höök. Material-selective surface chemistry for nanoplasmonic sensors: Optimizing sensitivity and controlling binding to local hot spots. *Nano Letters*, 12(2):873–879, 2012.

[187] A. Ulman. Formation and structure of self-assembled monolayers. *Chemical Reviews*, 96(4):1533–1554, 1996.

[188] A. Hucknall, S. Rangarajan, and A. Chilkoti. In Pursuit of Zero: Polymer Brushes that Resist the Adsorption of Proteins. *Advanced Materials*, 21(23):2441–2446, 2009.

[189] J Lahiri, L Isaacs, J Tien, and GM Whitesides. A strategy for the generation of surfaces presenting ligands for studies of binding based on an active ester as a common reactive intermediate: A surface plasmon resonance study. *Analytical Chemistry*, 71(4):777–790, 1999.

[190] S. Zhao and W. M. Reichert. Influence of biotin lipid surface-density and accessibility on avidin binding to the tip of an optical fiber sensor. *Langmuir*, 8(11):2785–2791, 1992.

[191] Joshua R. Wayment and Joel M. Harris. Biotin-Avidin Binding Kinetics Measured by Single-Molecule Imaging. *Analytical Chemistry*, 81(1):336–342, 2009.

[192] P. S. Katsamba, I. Navratilova, M. Calderon-Cacia, L. Fan, K. Thornton, M. D. Zhu, T. Vanden Bos, C. Forte, D. Friend, I. Laird-Offringa, G. Tavares, J. Whatley, E. G. Shi, A. Widom, K. C. Lindquist, S. Klakamp, A. Drake, D. Bohmann, M. Roell, L. Rose, J. Dorocke, B. Roth, B. Luginbuhl, and D. G. Myszka. Kinetic analysis of a high-affinity antibody/antigen interaction performed by multiple Biacore users. *Analytical Biochemistry*, 352(2):208–221, 2006.

[193] T. Bravman, V. Bronner, O. Nahshol, and G. Schreiber. The ProteOn XPR36 (TM) Array System-High Throughput Kinetic Binding Analysis of Biomolecular Interactions. *Cellular and Molecular Bioengineering*, 1(4):216–228, 2008.

[194] O. Nahshol, V. Bronner, A. Notcovich, L. Rubrecht, D. Laune, and T. Bravman. Parallel kinetic analysis and affinity determination of hundreds of monoclonal antibodies using the ProteOn XPR36. *Analytical Biochemistry*, 383(1):52–60, 2008.

[195] I. Le Trong, Z. Wang, D. E. Hyre, T. P. Lybrand, P. S. Stayton, and R. E. Stenkamp. Streptavidin and its biotin complex at atomic resolution. *Acta Crystallographica Section D-Biological Crystallography*, 67(9):813–821, 2011.

[196] P. C. Weber, D. H. Ohlendorf, J. J. Wendolski, and F. R. Salemme. Structural Origins of High-Affinity Biotin Binding to Streptavidin. *Science*, 243(4887):85–88, 1989.

[197] www.rcsb.org.

[198] PDB ID: 3RY1.

[199] PDB ID: 3RY2.

[200] P. S. Vukusic, G. P. Bryanbrown, and J. R. Sambles. Surface-plasmon resonance on gratings as a novel means for gas sensing. *Sensors and Actuators B-Chemical*, 8(2):155–160, 1992.

[201] D. C. Cullen, R. G. W. Brown, and C. R. Lowe. Detection of immuno-complex formation via surface-plasmon resonance on gold-coated diffraction gratings. *Biosensors*, 3(4):211–225, 1987.

[202] M. Piliarik, M. Vala, I. Tichy, and J. Homola. Compact and low-cost biosensor based on novel approach to spectroscopy of surface plasmons. *Biosensors & Bioelectronics*, 24(12):3430–3435, 2009.

[203] M. Piliarik and J. Homola. Surface plasmon resonance (spr) sensors: approaching their limits? *Optics Express*, 17(19):16505–16517, 2009.

[204] W. Hickel, B. Rothenhausler, and W. Knoll. Surface plasmon microscopic characterization of external surfaces. *Journal of Applied Physics*, 66(10):4832–4836, 1989.

[205] B. Rothenhausler and W. Knoll. Surface plasmon microscopy. *Nature*, 332(6165):615–617, 1988. 10.1038/332615a0.

[206] B. P. Nelson, T. E. Grimsrud, M. R. Liles, R. M. Goodman, and R. M. Corn. Surface plasmon resonance imaging measurements of dna and rna hybridization adsorption onto dna microarrays. *Analytical Chemistry*, 73(1):1–7, 2001.

[207] J. M. Brockman, B. P. Nelson, and R. M. Corn. Surface plasmon resonance imaging measurements of ultrathin organic films. *Annual Review of Physical Chemistry*, 51:41–63, 2000.

[208] O. Andersson, A. Larsson, T. Ekblad, and B. Liedberg. Gradient hydrogel matrix for microarray and biosensor applications: An imaging spr study. *Biomacromolecules*, 10(1):142–148, 2008.

[209] T. Rindzevicius, Y. Alaverdyan, A. Dahlin, F. Hook, D. S. Sutherland, and M. Kall. Plasmonic sensing characteristics of single nanometric holes. *Nano Letters*, 5(11):2335–2339, 2005.

[210] G. Raschke, S. Kowarik, T. Franzl, C. Sonnichsen, T. A. Klar, J. Feldmann, A. Nichtl, and K. Kurzinger. Biomolecular recognition based on single gold nanoparticle light scattering. *Nano Letters*, 3(7):935–938, 2003.

[211] K. M. Mayer, F. Hao, S. Lee, P. Nordlander, and J. H. Hafner. A single molecule immunoassay by localized surface plasmon resonance. *Nanotechnology*, 21(25), 2010.

[212] G. J. Nusz, S. M. Marinakos, S. Rangarajan, and A. Chilkoti. Dual-order snapshot spectral imaging of plasmonic nanoparticles. *Applied Optics*, 50(21):4198–4206, 2011.

[213] S. Patskovsky, R. Jacquemart, M. Meunier, G. De Crescenzo, and A. V. Kabashin. Phase-sensitive spatially-modulated surface plasmon resonance polarimetry for detection of biomolecular interactions. *Sensors and Actuators B-Chemical*, 133(2):628–631, 2008.

[214] W. J. Zhou, A. R. Halpern, T. H. Seefeld, and R. M. Corn. Near Infrared Surface Plasmon Resonance Phase Imaging and Nanoparticle-Enhanced Surface Plasmon Resonance Phase Imaging for Ultrasensitive Protein and DNA Biosensing with Oligonucleotide and Aptamer Microarrays. *Analytical Chemistry*, 84(1):440–445, 2012.

[215] www.flir.com.

[216] L. R. Hirsch, J. B. Jackson, A. Lee, N. J. Halas, and J. West. A whole blood immunoassay using gold nanoshells. *Analytical Chemistry*, 75(10):2377–2381, 2003.

[217] X. H. Huang, I. H. El-Sayed, W. Qian, and M. A. El-Sayed. Cancer cell imaging and photothermal therapy in the near-infrared region by using gold nanorods. *Journal of the American Chemical Society*, 128(6):2115–2120, 2006.

[218] G. Baffou, R. Quidant, and J. F. Garcia de Abajo. Nanoscale Control of Optical Heating in Complex Plasmonic Systems. *ACS Nano*, 4(2):709–716, 2010.

[219] M. Kuwata-Gonokami, N. Saito, Y. Ino, M. Kauranen, K. Jefimovs, T. Vallius, J. Turunen, and Y. Svirko. Giant optical activity in quasi-two-dimensional planar nanostructures. *Physical Review Letters*, 95(22), 2005.

[220] M. Hentschel, M. Schaeferling, T. Weiss, N. Liu, and H. Giessen. Three-Dimensional Chiral Plasmonic Oligomers. *Nano Letters*, 12(5):2542–2547, 2012.

[221] V. K. Valev, J. J. Baumberg, C. Sibilia, and T. Verbiest. Chirality and Chiroptical Effects in Plasmonic Nanostructures: Fundamentals, Recent Progress, and Outlook. *Advanced Materials*, 25(18):2517–2534, 2013.

[222] A. Papakostas, A. Potts, D. M. Bagnall, S. L. Prosvirnin, H. J. Coles, and N. I. Zheludev. Optical manifestations of planar chirality. *Physical Review Letters*, 90(10), 2003.

[223] R. Singh, E. Plum, W. Zhang, and N. I. Zheludev. Highly tunable optical activity in planar achiral terahertz metamaterials. *Optics Express*, 18(13):13425–13430, 2010.

[224] D. Wang, W. Zhu, M. D. Best, J. P. Camden, and K. B. Crozier. Wafer-scale metasurface for total power absorption, local field enhancement and single molecule Raman spectroscopy. *Scientific Reports*, 3, 2013.

[225] B. Liedberg, C. Nylander, and I. Lundstrom. Biosensig with surface-plasmon resonance - how it all started. *Biosensors & Bioelectronics*, 10(8):R1–R9, 1995.

[226] www.biacore.com.

[227] M. E. Stewart, C. R. Anderton, L. B. Thompson, J. Maria, S. K. Gray, J. A. Rogers, and R. G. Nuzzo. Nanostructured plasmonic sensors. *Chemical Reviews*, 108(2):494–521, 2008.

[228] S. I. Shopova, R. Rajmangal, S. Holler, and S. Arnold. Plasmonic enhancement of a whispering-gallery-mode biosensor for single nanoparticle detection. *Applied Physics Letters*, 98(24):243104–3, 2011.

[229] B. K. Min, E. Ostby, V. Sorger, E. Ulin-Avila, L. Yang, X. Zhang, and K. Vahala. High-q surface-plasmon-polariton whispering-gallery microcavity. *Nature*, 457(7228):455–U3, 2009.

[230] N. Liu, T. Weiss, M. Mesch, L. Langguth, U. Eigenthaler, M. Hirscher, C. Sonnichsen, and H. Giessen. Planar metamaterial analogue of electromagnetically induced transparency for plasmonic sensing. *Nano Letters*, 10(4):1103–1107, 2010.

[231] F. Hao, P. Nordlander, Y. Sonnefraud, P. Van Dorpe, and S. A. Maier. Tunability of subradiant dipolar and fano-type plasmon resonances in metallic ring/disk cavities: Implications for nanoscale optical sensing. *ACS Nano*, 3(3):643–652, 2009.

[232] A. V. Kabashin, P. Evans, S. Pastkovsky, W. Hendren, G. A. Wurtz, R. Atkinson, R. Pollard, V. A. Podolskiy, and A. V. Zayats. Plasmonic nanorod metamaterials for biosensing. *Nature Materials*, 8(11):867–871, 2009.

[233] N. Liu, M. Mesch, T. Weiss, M. Hentschel, and H. Giessen. Infrared perfect absorber and its application as plasmonic sensor. *Nano Letters*, 10(7):2342–2348, 2010.

[234] A. N. Grigorenko, P. I. Nikitin, and A. V. Kabashin. Phase jumps and interferometric surface plasmon resonance imaging. *Applied Physics Letters*, 75(25):3917–3919, 1999.

[235] Y. C. Li, Y. F. Chang, L. C. Su, and C. Chou. Differential-phase surface plasmon resonance biosensor. *Analytical Chemistry*, 80(14):5590–5595, 2008.

[236] A. B. Dahlin. Size Matters: Problems and Advantages Associated with Highly Miniaturized Sensors. *Sensors*, 12(3):3018–3036, 2012.

[237] D. M. Rissin, C. W. Kan, T. G. Campbell, S. C. Howes, D. R. Fournier, L. Song, T. Piech, P. P. Patel, L. Chang, A. J. Rivnak, E. P. Ferrell, J. D. Randall, G. K. Provuncher, D. R. Walt, and D. C. Duffy. Single-molecule enzyme-linked immunosorbent assay detects serum proteins at subfemtomolar concentrations. *Nature Biotechnology*, 28(6):595–U25, 2010.